UNIVERSITY OF SOUTHAMPTON

HIGH-BRIGHTNESS DIODE-PUMPED WAVEGUIDE LASERS

by

Jacob Isa Mackenzie

Submitted for the degree of

Doctor of Philosophy

Faculty of Engineering and Applied Science

Department of Electronics and Computing Science

April 2003

The most beautiful thing we can experience is the mysterious.
It is the source of all true art and science.

Albert Einstein

UNIVERSITY OF SOUTHAMPTON

ABSTRACT

FACULTY OF ENGINEERING AND APPLIED SCIENCE

ELECTRONICS AND COMPUTING SCIENCE

Doctor of Philosophy

HIGH-BRIGHTNESS DIODE-PUMPED WAVEGUIDE LASERS

By Jacob Isa Mackenzie

Reported in this thesis are advances toward high-brightness diode-pumped planar waveguide (PW) lasers. Efficient and compact planar waveguide lasers are made possible by their geometry, which is compatible with that of high-power diode lasers, has very good thermal management characteristics, and delivers high optical gains per unit pump power. Thus using the waveguide structure in conjunction with trivalent rare-earth ions, multi-Watt diffraction-limited operation of weak and quasi-three-level laser transitions can be obtained.

Large mode area (LMA) double-clad planar waveguides, fabricated via direct bonding sapphire and YAG, are the primary structures investigated herein. These high numerical aperture waveguides are ideally suited to high-power diode-pumping due to a combination of features related to their slab-like configuration. Furthermore the LMA double-clad planar waveguide is shown to robustly select the fundamental waveguide mode. This general result leads to guided-diffraction-limited output, applicable to a range of oscillating wavelengths.

Two in-plane pumping geometries are detailed; longitudinal or end-pumping and transverse or side-pumping. For end-pumping, the pump is conditioned in one axis to enable launching into the waveguide, and at the same time the free space axis is matched to the fundamental mode of a simple monolithic laser cavity. As such, efficient end-pumped operation of Nd:YAG, Yb:YAG, and Er:YAG LMA-PW lasers were realised. With Nd:YAG for 7.5W of absorbed pump power, 4.3W of CW 1.064μm output was observed. Changing the resonator mirrors to optimise the quasi-three level transition an output of 3.5W at 946nm was measured, corresponding to 6.5W of absorbed pump. In addition the much weaker and rarely studied 1.8μm transition, operated with as much as 0.4W. In a similar configuration, 0.45W of 2.7μm CW output was obtained from a highly doped Er:YAG LMA-PW with 4.6W of absorbed pump power. As the first Er:YAG waveguide laser to be reported, it illustrates the possibility to obtain high output power and good beam quality from weak laser transitions with these structures.

Furthermore by integrating a Cr^{4+} saturable absorber into a Yb:YAG LMA-PW, an end-pumped passively Q-switched laser was demonstrated with 2.3W average power at 1.03μm in a near-diffraction-limited beam. Pulses of ~2ns temporal width at repetition rates approaching 80kHz produced peak powers of ~20kW. Operation of a similar Nd:YAG LMA PW laser, on both the 1.064μm and 946nm transitions, was also demonstrated and its performance shown to be inferior to that of the Yb^{3+}-doped structure in this pumping configuration.

Using the side-pumping scheme higher-powers can be obtained, typically however, at the expense of the resonator complexity when trying to obtain high brightness performance. As such a monolithic Tm:YAG LMA-PW laser, pumped by two proximity-coupled diode bars, produced 15W at 2μm with an asymmetric low brightness beam, despite being diffraction-limited in the guided axis. In addition two separate Nd:YAG LMA-PW lasers were trialled with unstable and external resonator geometries. Watt level output powers with significantly enhanced brightness were observed. Further designs for power scaling these devices are discussed.

TABLE OF CONTENTS

ACKNOWLEDGEMENTS

After such a long undertaking like a PhD, there are many people to thank for their support, assistance, and encouragement. I hope to be able to include you all. What initially was an interest and an idea, “Why not complete my studies overseas?”, became a reality through the efforts of my supervisor Dr Dave Shepherd and one very caring student coordinator, Mrs Eveline Smith. Thank you both for your backing and the Optoelectronics Research Centre (ORC) for providing me with this opportunity.

Once into my studies, Dave’s continued pedagogical role left me in no doubt that I was in very capable hands. I am honoured to have you as a mentor. For some of my earlier work I was also guided by Prof. Anne Tropper, to whom I am grateful for our discussions on the basics of laser physics in waveguide structures. It was around the beginning of my second year that I had the opportunity to visit our collaborators, Onyx Optics, in California USA. There I had the pleasure to meet and work with the Meissner family, Dr Raymond Beach, and Mr Scott Mitchell. I would like to pay a special tribute to Ray, for his plethora of publications and the several discussions that founded a good portion of the material to follow. My best wishes and gratitude to you all, your input, help, and waveguides were invaluable in helping me achieve this milestone.

Closer to hand, my colleagues within the Crystal Waveguide Laser group were also instrumental in many aspects regarding my studies. Many thanks to Dr Cheng Li, Dr Taj Bhutta, Dr Catherine Bonner, and of course soon to be Dr Simon Hettrick. It has been a memorable and enjoyable experience to work with you all. This brings me also to those other important people, without whom my experiments would not have reached fruition. Thank you Simon Butler, Chris Nash, and Tim McIntyre; your skills, ideas, and the components you made, fixed, or adjusted, in a “hurry”, helped me more than you realise.

Diverging from the technical path slightly, I wish to express my gratefulness to those loved ones and close friends who were always there for me. Especially to my friends and family, who I left behind in Adelaide, Sydney, Newcastle, and Canberra to pursue student-hood one last time; I missed you all. To my new friends and housemates gathered since arriving in the UK, you have made these past years truly great. A special thought goes to Erica, Caterina, Lola, Vittoria, Carlos, Isabel, Arshad, Constantino, Gilberto, Cristiana, Laura, Jose-Maria, and the rest of the Italian collection; the spirit of our “family” unit

added that special touch to living abroad. Indeed, moving to the other side of the planet did have its downsides; it was at those times that my connection with my mother helped enormously, without her I would not be the person I am today. Her intuition, integrity, and vision give me strength and courage, for which I am eternally grateful.

Finally, I must bow and acknowledge my examiners, Dr Andrew Scott and Prof. David Richardson, without whom I would most probably never have had the opportunity to talk for three hours about my last three years of study! In fact I appreciated the viva experience for this very reason and trust that I was able to impress some of my enthusiasm for the planar waveguide laser on you as well.

Thank you one and all.

J.I. Mackenzie

June 2003.

Chapter 1

INTRODUCTION

1.1 Topic overview

Guided wave lasers were among the first optical lasers developed, their operation demonstrated as early as 1961 [1]. In the pursuing years the waveguide laser has achieved increasing importance, diode and fibre lasers being the most prominent examples. More recently planar waveguides structures comprising dielectric crystal layers have been demonstrated as potential candidates for high-power solid-state laser devices [2-6] due to a combination of features related to their slab-like geometry. This thesis describes significant developments leading toward efficient, high-brightness, high-power, diode-pumped planar waveguide lasers (PWL).

Globally there is significant interest in high-average-power bright laser sources that are compact, robust, and have minimal thermal and electrical requirements. Various wavelengths are also desired specific to the particular application, for example: medical systems require ultra-violet (UV), visible, and near to mid infra-red (IR) sources that match known absorption characteristics for various parts of the human body; communication systems use near IR wavelengths corresponding to transmission windows in optical fibres, or as pump sources for optical amplifiers; remote sensing or ranging applications also typically use near to mid IR sources, bounded by scattering losses at shorter wavelengths and water vapour absorption toward longer wavelengths; materials processing simply require high power and brightness at wavelengths that interact with the material of interest; whilst for military and space applications, compactness, durability, and robustness are all necessary. PWL have the potential to meet many of these requirements.

The spatial brightness of a laser source is defined by its beam quality and output power and governs the spot size to which its output can be focussed. One measure of beam

quality is given by the M^2 factor, equivalent to the degree to which the divergence exceeds natural diffraction. Similarly, for characterising beam quality the standard[i] is to use the beam-parameter product, Q, which states that the product of the beam waist radius and its divergence is constant [7],

$$Q_i = W_{0_i}\Theta_{0_i} = \frac{M_i^2\lambda}{\pi} = const \qquad \textbf{(1.1).}$$

W_{0_i} is obtained, in each Cartesian axis (i = x,y, for a beam propagating along the z-axis), from the second-order moment (σ_i) of the intensity distribution[ii], and Θ_0 is the half-angle far-field divergence corresponding to the asymptote of $W_i(z)$[iii] [8], and λ is the optical wavelength in the propagation medium.

For a beam propagating along the z-axis, its brightness is given by the expression,

$$B = \frac{P}{\pi^2 Q_x^2 Q_y^2} = \frac{P}{\left(M_x^2 M_y^2 \lambda\right)^2} \qquad \textbf{(1.2).}$$

This parameter has significant importance for many applications that require high intensity and is applicable to this thesis in two respects; firstly the brightness of the pump source defines the efficiency with which its radiation may be coupled into a waveguide, and secondly in terms of the brightness obtainable from a planar waveguide laser. It should be noted that the denominator of equation (1.2) is minimised for a diffraction-limited source (i.e. M^2=1); therefore, to scale brightness it is necessary to increase the output power, P, whilst maintaining a diffraction-limited beam quality.

---

[i] ISO 11146:1999, International Standard - Lasers and laser-related equipment - Test methods for laser beam parameters - Beam widths, divergence angle and beam propagation factor

[ii] Second-order moment: $\sigma_i = \sqrt{\frac{1}{P_0}\int_0^\infty i^2 I_0(i)di}$, $I_0(i)$ the intensity distribution along the i^{th} axis, with the origin representing the centre of gravity of the profile, and P_0 the total power of $I_0(i)$. The beam waist is then obtained using, $W_{0_i} = 2\sigma_i$.

[iii] Propagation of a paraxial beam is described by: $W_i(z) = W_{0_i}\sqrt{1+\left(\frac{M_i^2\lambda\, z}{\pi\, W_{0_i}^2}\right)^2}$.

1.2 Planar waveguide lasers

A planar waveguide consists of a layer of material capped by regions of lower refractive index, n_{clad} and n_{subs}, Figure 1-1. Optical radiation trapped by total internal reflection (TIR) within the higher index layer, n_{core}, is constricted in one axis as it propagates along the plane of the composite structure. The guidance and laser properties of these devices are discussed in more detail in the following chapter; however it is constructive to give a review of the progress and current state of affairs in the area of planar waveguide lasers.

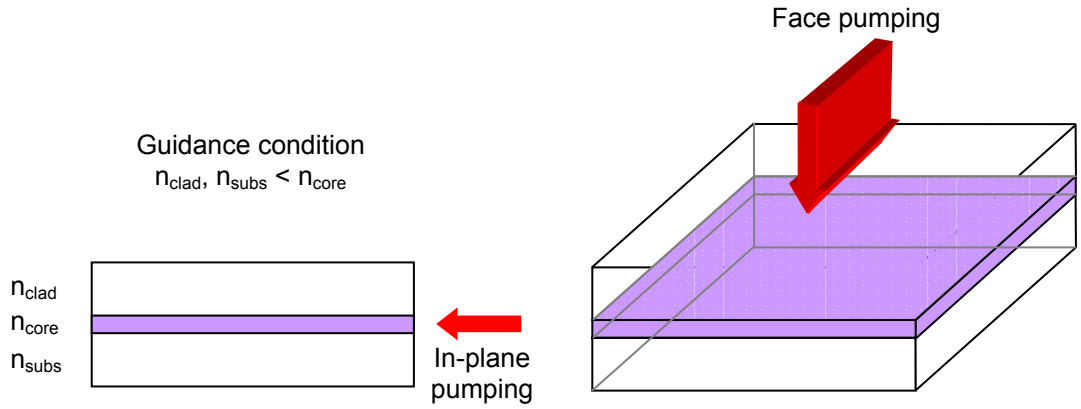

Figure 1-1: Planar waveguide schematic and optical excitation schemes.

1.2.1 Historical review

Waveguide structures were first employed in lasers to reduce laser threshold and thus avoid the need for high pump powers. In addition confining the radiation to small volumes circumvented the difficulties in fabricating large optical-quality active materials [1]. Subsequently there were many fibre lasers reported during the 1960's [9], along with a dye based dielectric planar waveguide laser in 1971 [10]. It was 1962 when the first diode lasers were demonstrated [11], their subsequent use as an optical pump source paved the way for efficient compact laser sources of the future and have had far reaching consequences. Assisted by the already burgeoning field of electronics, the quality of semiconductor materials and devices promptly outstripped that of dielectrics. As such active-semiconductor waveguide structures were well characterised and developed during the pursuing years. Even today however, state of the art diode lasers are limited in their output powers to <10W per emitter [12], typically due to thermal effects and catastrophic optical damage at the emitting facet [13].

During the decades following the inception of the laser, interest increased in active gaseous media that could be excited by well understood techniques such as electric or RF discharges. Even using a gaseous active media waveguides found their niche, with the first gas waveguide laser demonstration at the beginning of the 1970's [14]. In the following years there was continued growth in this field, especially in the high-power area, with a 1-kW planar-waveguide CO_2 laser demonstrated in 1991 [15]. Previous to this however, miniaturisation and planar compatibility were key phrases of the 1970's and 1980's, corresponding to the growing interest in optical integrated circuits (OIC). Planar devices in conjunction with integrated optics were believed to be crucial in the development of miniature communication systems [16]. Unfortunately, an optical equivalent to what silicon is for electronics has not yet been realised, consequently OIC on the same scale are still to eventuate. One benefit of the strong interest in OIC was that there have been many techniques developed for fabricating optical waveguides in dielectric materials, several of which are now employed to develop miniature and robust planar devices, including waveguide lasers.

Waveguide fabrication falls under two broad headings, modification of the refractive index profile, or co-joining materials with dissimilar refractive index. The first can be obtained through processes such as ion-exchange [17], ion-diffusion [18], ion-implantation [19], or optical writing methods [20, 21]. Typically these techniques, with exception of the last, form relatively thin waveguides with low numerical apertures (NA[iv]) and therefore are not compatible for guiding highly divergent or multimode laser diode radiation. Alternatively, the second fabrication methodology allows relatively thick guides of high index contrast and therefore high NA waveguide structures. Techniques utilised to fabricate composite structures of dissimilar materials include; sputtering [22] or deposition [23], growth through epitaxial processes [24], or simply adhesion [25].

Considering the vast number of articles and fabrication possibilities for dielectric planar-waveguide lasers, there have been a limited number of high-power (>1W) devices demonstrated. From the outset, after initial demonstrations of high-power-diode pumping of planar waveguides in 1992 by researchers at the University of Southampton [26], there

[iv] $NA = (n_{core}^2 - n_{clad,subs}^2)^{1/2}$, where n_{core} is the core refractive index and $n_{clad,subs}$ is the larger of the cladding and substrate refractive indices.

were two generic pumping schemes adopted, see Figure 1-1. In 1995 Heriot-Watt University researchers envisaged a face pumping scheme for thin slabs [27], which was soon applied to very thick multi-mode waveguides, where a large active core was required to achieve reasonable absorption efficiency. Instead, in-plane pumping (side or end) was adopted by researchers at the University of Southampton, LETI[v] [28], and later the Max-Born-Institut für Nichtlineare Optik und Kurzzeitspektroskopie[vi] [29].

At the conference of Advanced Solid State Lasers in 1997, D.P. Millas of Heriot-Watt University presented results detailing a 9W average-power, quasi-continuous-wave (QCW) diode-face-pumped thick YAG planar waveguide [30]. The waveguide consisted of a 200-μm-thick Nd^{3+}-doped core, clad with 400−μm-thick un-doped YAG and was fabricated using the thermal-bonding technique [25]. The following year Bonner *et al.* [2] were to report a CW multi-Watt (6.2W) PWL grown via liquid phase epitaxy (LPE), the 80 μm thick multi-mode Nd:YAG waveguide was end-pumped with a 20W diode laser bar. In 1999 Shepherd *et al.* [31] obtained a second CW multi-Watt (3.7W) result, using a thermally-bonded planar waveguide and the same end-pumping geometry as for the previous LPE PWL, although with a much smaller 8−μm-thick Nd:YAG core, clad with sapphire. Griebner *et al.* following on from previous success in obtaining near-diffraction-limited output from a multimode fibre laser using an extended cavity [32], were able to improve the planar-waveguide laser brightness demonstrating a 1.2W CW output power with beam quality (M^2 values) of 1.5x4 [3]. Also a thermally-bonded planar composite, it comprised a 100-μm-thick 10 at.% Yb:YAG active core capped by 300μm un-doped YAG cladding layers. This result was immediately followed by a 1W direct-bonded Yb:YAG channel-waveguide structure, with a 100μm by 100μm cross section and un-doped YAG cladding, and had nearly diffraction-limited beam quality in both axes [33].

In keeping with the concept of compact, robust and simple high-power sources Bonner *et al.* reported the first monolithic double-clad planar waveguide lasers [4]; the result of a

---

[v] LETI, CEA, Technologies Avancée, Grenoble, France.

[vi] Max-Born-Institut für Nichtlineare Optik und Kurzzeitspektroskopie, Berlin, Germany.

collaboration between the University of Southampton and Onyx Optics[vii]. Diffraction-limited beam quality in the guided axis was obtained for Ytterbium and Neodymium doped YAG composite structures, with output powers of ~2W and ~4W respectively. Furthermore, this paper described the technique of proximity coupling a diode bar to the waveguide, leading to efficient and direct pumping of the active region without the necessity of intermediary optics. Extending this result, Beach *et al.* [5] obtained >12W from a side-pumped proximity-coupled double-clad Yb:YAG PWL, again although diffraction-limited in the guided axis, the unguided axis beam quality was still highly multi-mode. Reported in the same paper was the first monolithic strip unstable resonator for improving the beam quality in the plane of a double-clad Nd:YAG composite structure. In addition they also detailed the first demonstration of a passively-Q-switched (PQS) high-power waveguide laser. An average output power of ~8W was obtained with pulses of ~3ns temporal width and a repetition rate of ~80kHz.

This historical review has now reached midway through the period of investigation related to the work described herein. Further developments outside of those described herein were the continued improvements of the face-pumped geometry at Heriott-Watt University, where the output power has been scaled to 150W in multi-mode operation and >100W in a high-brightness configuration using an external negative-branch unstable resonator [34]. Similar thick waveguide structures have also been used in a self-imaging (Talbot imaging) configuration for lasers and amplifiers [35-37].

1.3 High-power solid-state laser systems

Currently there is significant development activity in the field of high-power solid-state lasers sources. Over the past decade typical output powers from single oscillators, with near or fully diffraction-limited beam quality, have escalated from ~10W to several hundreds of Watts [38-48]. Continuous wave (CW) output powers greater than 1kW have also been obtained using solid-state lasers, although with less than diffraction-limited beam quality [49-52].

There are many inter-related parameters which have to be considered when designing high-brightness, high-power solid-state laser systems [53]. The major difficulty lies with

[vii] Onyx Optics, Dublin, CA 94568, USA

managing the residual excitation power not converted into useful laser output, normally manifesting as a thermal load in the active material. Although planar waveguide lasers have not yet exhibited the same output powers as described in the previous paragraph, this relatively new field of research has a good potential for doing so. Some of the key parameters for developing high-average power lasers are introduced subsequently, highlighting the features that planar-waveguide structures exploit.

1.3.1 Active media

Choosing an active material is primarily driven by the application requirements, such as laser wavelength, output power, continuous or pulsed operation, etc. Consequently, in regard to an active medium selection there are two choices to be made: firstly which active ion(s) to use, this sets the general spectroscopic characteristics; secondly a compatible host material that defines the fine spectroscopic details along with the optical and thermo-mechanical properties. These later parameters are important to the overall system performance, such as efficiency, beam-quality, and output power or energy capabilities.

Tri-valent rare-earth (RE^{3+}) ions are the most commonly used activators, due to their electronic configuration of a partially occupied 4*f* electron subshell, which is in some measure shielded from crystal fields associated with neighbouring ions by the completely filled 5s and 5*p* electron shells [53]. Furthermore, these activator ions have been successfully substituted into many crystalline hosts, Nd^{3+} being the most prominent example [54]. Transition metal ions are also well established activators, and usually have very broad spectroscopic features favouring tuneable laser wavelengths or short pulse generation, such as the Ti^{3+}:sapphire laser. Furthermore, some actinide (Ac^{3+}) ions have been suggested as having suitable stimulated emission characteristics for laser action, although few of these radio-active elements have yet to demonstrate efficient operation [53, 55].

Many high-average-power laser systems take advantage of the high thermal conductance characteristics of crystalline materials in order to avoid temperature dependent effects degrading performance. Yttrium Aluminium Garnet (YAG), $Y_3Al_5O_{12}$, has proven itself an invaluable host material for such applications. This is primarily due to its good thermal, optical, chemical, and mechanical properties and suitability for rare-earth doping [54].

Investigated herein are planar-waveguide structures comprised of YAG and sapphire (Al_2O_3), capitalising upon both the excellent laser performance of rare-earth-doped YAG and the approximately three times higher thermal conductivity of sapphire.

1.3.2 Pump Source

Advancing semiconductor technologies have helped in the drive toward compact, high-average-power, solid-state lasers. Accordingly, simple and efficient pump sources such as the high-power laser diode are of great importance for today's and future laser systems. High-power diode-lasers, although typically multimode and with highly asymmetric outputs, are gradually overtaking the flashlamp as the pump source of choice for solid-state active materials, for reasons primarily based on lifetime, reliability, improved efficiency, and waste heat management [13]. Typically the low brightness output of laser diodes limit their usefulness for direct use in the applications listed earlier, despite the developments in conditioning the spatial-output of high-power diode devices that have improved the achievable brightness by 2~3 times [7]. This has allowed diode sources to now be used directly for several materials processing applications. However, there are still many other applications that require even brighter laser sources, which at this stage can only be accessed via other active materials, and for which diode lasers may be used as the pump source.

Two laser diode geometries were employed for the experiments discussed in the following chapters. The first are high-brightness multi-mode single-broad-stripe emitters and the second are linear arrays of single emitters in the form of low-brightness high-power diode-laser bars. Both have a geometry that is compatible with that of the planar waveguide. The latter is more suitable for power scaling in a side-pumped arrangement, whereas the first is shown to be a very effective pump source for highly efficient end-pumped multi-Watt diffraction-limited lasers.

1.3.3 Thermal management

For high-average-power solid-state laser systems, the thermal dynamics within the host medium are of paramount importance. Significant thermal loading of the host material derived from the waste heat generated in the pumped volume leads to graded refractive index profiles, distortion of the crystal surfaces, and stress effects detrimental to laser performance or even fracture [56]. The latter occurs when the temperature gradients between the heat source and heat sink, with the surfaces of the host medium acting as the

cooling interface, create stresses that exceed the tensile strength of the material. Currently there exist four distinct trends in solid-state host medium geometries associated with managing high thermal loads. They are the rod [57-59], fibre [60, 61], slab [62-65], and 'thin-disc' [66, 67], each of which have their own advantages and disadvantages.

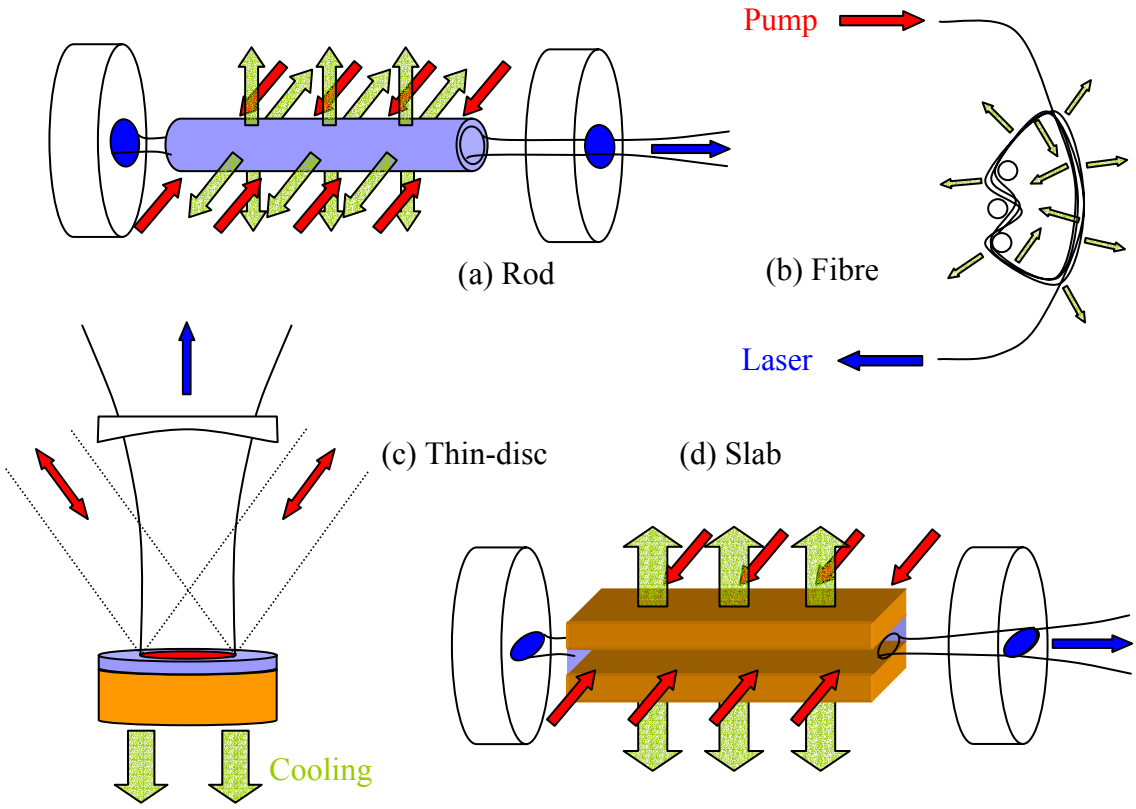

Figure 1-2: Schematic of the four host geometries associated with thermal management in high-power laser systems (a) rod, (b) fibre, (c) thin-disc, and (d) slab.

The laser rod has an historical importance and relatively simple fabrication technology, therefore efforts continue in developing high-power rod laser systems despite its relatively poor thermal characteristics. Some techniques used to overcome the pump power limitations imposed by stress fracture have included; uniform pumping geometries [57, 68], low doping concentrations or "wing-pumping" [58] and end-pumping with un-doped end-caps [58, 69-71]. Even with these pumping techniques, the maximum thermal loading of an active rod is limited by its geometry and the material properties of the host. Moreover, effects such as thermally induced birefringence have to be compensated for by additional intra-cavity elements, adding to the complexity of the laser cavity [51, 59].

In contrast the fibre laser, equivalent to a very long thin rod, relies upon the distribution of the heat load along its length, thus increasing the surface area through which the heat may be extracted [60, 72]. Currently experiencing a renaissance in research and development interest, fibre-laser brightness has increased fivefold over the past few years. In fact these devices are currently at the forefront of high-brightness, solid-state, high-average-power laser sources [48]. Not only can the thermal load be spread over the length of the fibre, the index guiding provided by its design dominates induced lensing effects, allowing diffraction-limited operation to be maintained even for very high pump powers [73]. Practical limitations reached to date include, efficient coupling of the low-brightness high-power laser diodes into the fibre, and nonlinear effects such as stimulated Raman scattering (SRS) and stimulated Brillouin scattering (SBS) brought about by the very-high intensity interaction-length product [48]. Another interesting configuration of the fibre-laser is that presented by Ueda *et al.* [74]: a side-pumped design, the fibre has a rectangular profile and is wrapped into a disk shape, similar to a planar waveguide with a coiled active gain region. This compact design generates >1kW of output power with an M^2 factor of 15 and electrical to optical efficiency of ~15-18%.

Thin-disc lasers [66], effectively the opposite extreme of the rod geometry with respect to the fibre, takes advantage of one-dimensional temperature gradients in the longitudinal, "thin", axis. This is in stark contrast to the rod and fibre where heat is removed radially. The thin-disc laser utilises a very thin active region, ~0.2mm thick, in close proximity to a heat sink, whereby the largest cooling surface is the end face perpendicular to the lasing axis. One drawback with this design is the pumping scheme complexity, requiring multiple passes through the same gain region to achieve sufficient absorption. Nevertheless, these laser systems have generated impressive output powers and optical efficiency [52].

The slab geometry, also known to offer good thermal management properties [62, 75], has a simplified power scaling advantage over its cylindrical counterpart due to the possibility of side or face pumping and yet still maintaining uniform one-dimensional temperature gradients within the host medium [62, 65]. This assumes a high aspect ratio slab that is cooled through the faces perpendicular to the thin dimension and well away from the end faces. Furthermore, when considering the important case of quasi-three-level laser materials, Rutherford *et al*. [65] report that the side-pumped slab has an advantage over

the thin-disc for slab-aspect ratios greater than the number of pump passes, N, through the thin disc active region. This corresponds to a figure of merit relating the pump power at which fracture would occur divided by the pump power required to excite the material to transparency. Currently the maximum number of pump passes, N, reported for the thin-disc laser stands at 16 [52].

Planar waveguides can be seen as the ultimate example of the high-aspect-ratio slab geometry, with the laser medium thickness of the order of the optical wavelength. If one considers the active core region of the planar waveguide as the "slab" described by Rutherford *et al.* [65], the aspect ratio is typically >100. The implication is that the planar waveguide does indeed have potential for high-power applications at least in the case of quasi-three-level laser systems, e.g. Yb^{3+}. Additionally, the side-pumped slab geometry offers the opportunity to utilise three independent axes for excitation, waste heat extraction, and signal generation, simplifying some of the engineering problems associated with high-power systems.

1.3.4 Cavity design

Efficient and bright laser sources require that the lowest order oscillating mode overlaps well with the excited volume of the active material. In the case of low-brightness laser-diodes, efficiently transferring their radiation into a small volume is limited by their beam quality, therefore it is often necessary to use a simple pump-coupling scheme at the expense of increasing resonator complexity. Diffraction-limited beams that have a reasonable overlap with the relatively large pump volume can be obtained in a variety of ways, for example, utilising telescopic resonators [76], multi-pass slabs [77, 78], or unstable resonators [79].

Efficient laser operation has been demonstrated using planar gain regions [26, 64, 77, 78, 80], avoiding the need for beam-shaping [81] or brightness-reducing fibre coupling [82] typically required to condition the diode-pump radiation to match circularly symmetric cavity modes. Moreover, a waveguide structure can improve spatial mode control in the guided axis and reduce susceptibility to induced thermal effects, as will be discussed in later chapters.

1.4 Approach for work presented herein

Following on from earlier work undertaken at the University of Southampton, methods to enhance diode-pumped planar waveguide laser brightness are investigated for in-plane pumping configurations. Therefore this work has a general theme of spatial-mode-control in the guided and un-guided axes of these devices.

Furthermore, planar waveguide lasers are studied beyond the simple pursuit of high output powers where the application of the waveguide structure is advantageous for developing compact, efficient, and diverse devices. Combining the natural compatibility of the diode laser and active planar waveguide, it is possible to produce thin regions of very high-gain. Thus laser threshold can be achieved with low pump powers, even when using materials with weak stimulated emission properties or re-absorption losses at the laser wavelength. This feature and the good thermal management characteristics of the direct-bonded planar waveguides make it possible to develop compact and efficient laser sources not easily achievable in bulk laser configurations.

1.4.1.1 Spatial-mode control – the guided axis

High-power double-clad waveguides in both fibre [45, 48, 72, 73] and planar [4, 5] configurations have shown excellent spatial-mode control. The term “double-clad” was originally coined in relation to fibres that had an inner waveguide supporting only the fundamental-mode at the laser wavelength, and an outer guide capturing the pump radiation, Figure 1-3(a). Alternatively this was also called cladding-pumping. Classically then, a double-clad waveguide implied an isolated single-mode active core within a larger passive high-NA multi-mode waveguide; typically the inner guide is much smaller than the outer, hence the overlap of the pump field distribution with the active region scales the absorption length proportionally [83].

An extended absorption length is well suited to the double-clad fibre configuration, due to its low propagation losses and the relative ease to fabricate long lengths; notably, it also leads to a spreading of the thermal load and increased surface area through which to extract the heat. In the planar case however, practical device lengths are limited to the order of centimetres rather than tens of meters. Therefore it is necessary to maintain a small area-difference between the core and outer cladding, which is apparently in contradiction with maintaining a single-more core and increasing the outer cladding

separation. In fact this is indeed true and the design of the waveguides, Figure 1-3(b), reported by [4] and [5] do not have single-mode cores, rather they are comparable to large-mode-area (LMA) fibres, [84, 85]. Single-mode operation is maintained by gain mode-selection rather than index guiding, as with the classical double-clad fibre, this is discussed in detail in the following chapter. However, it is important to note that the fundamental mode of the LMA structure is not well confined to the core and therefore interacts with the outer cladding layer, thus leading to the index profile of the entire structure defining the propagating mode characteristics.

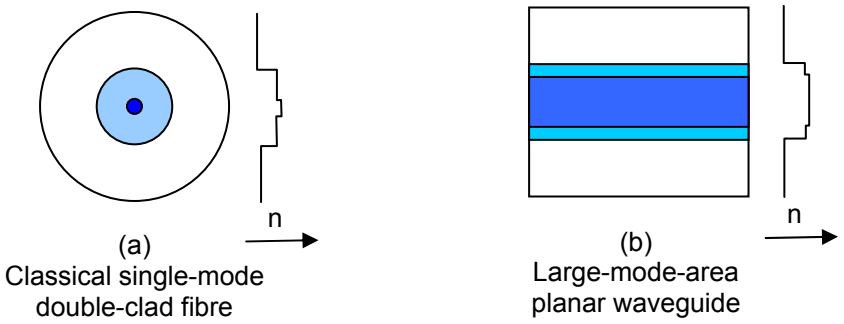

Figure 1-3: Schematic of double-clad waveguide structures and refractive index (n) profile: (a) "Classical" single-mode core double-clad fibre [72] and (b) double-clad planar waveguide[4].

1.4.1.2 Spatial-mode control – the un-guided axis

Notwithstanding the advantages of the planar waveguide, the spatial mode quality in the plane still needs to be addressed to achieve high brightness laser sources. Spatial control of the laser field within a laser cavity may be achieved in a variety of ways, the most obvious being the resonator configuration. However, for monolithic near-planar stable resonators of around ~1cm in length, the fundamental mode radius is of the order of ~100μm[viii] [86]. This implies significant restrictions on the pump characteristics and its conditioning, which at present are not easily met with high-average-power (>10W) diodes.

[viii] The beam waist in a stable laser cavity, neglecting lensing effects is given by: $\omega_0 = \left(\frac{\lambda_m l}{\pi}\right)^{\frac{1}{2}} \frac{[g_1 g_2 (1 - g_1 g_2)]^{\frac{1}{4}}}{(g_1 g_2 - 2 g_1 g_2)^{\frac{1}{2}}}$,

where λ_m is the laser wavelength in the active medium, l is the length of the medium, $g_i = 1 - l/R_i$, where R_i is the radius of curvature of the i^{th} mirror. Hence for the example considered above in the text the leading term is of the order of 100μm and the second of the order of unity.

As such the end-pumped planar waveguide lasers investigated herein utilize relatively high-brightness pump sources (e.g. broad-stripe diodes) that can be coupled into the waveguide, whilst simultaneously conditioned to match the fundamental in-plane cavity mode.

One technique used to expand the fundamental cavity mode, easing the requirements on the pump beam quality, is the telescopic resonator [76]. A novel variation of this technique, using an extended cavity arrangement with two cylindrical lenses and a plane mirror is described in chapter 5. Furthermore, a quasi-monolithic stable multi-pass resonator also employing a beam expanding telescope in one axis is proposed and discussed in chapter 6.

Unstable resonators are another alternative that offer an efficient means to extract the available gain in short cavities [87]. Typically to achieve good beam quality from such resonators, high cavity-output-coupling is necessary, thus requiring high gain active elements. Fortunately this is possible with planar waveguide structures by employing strip unstable resonators [5, 6]. Such a resonator is described in chapter 5 and its performance discussed.

In principle it is also possible to modify the spatial characteristics of electro-magnetic fields through their spectral [88, 89] or phase components [37, 90-92]. However, these techniques have not been investigated herein.

Finally, one other method for mode control is to introduce a waveguide in the plane, thus essentially making a channel waveguide [33]. However to achieve diffraction-limited performance from a monolithic device requires that it supports a single mode or be a LMA structure, therefore for the associated small waveguide dimensions it is not obviously power-scalable. One approach demonstrated with good results, was a Ti:sapphire pumped ion exchanged Nd^{3+}-doped glass waveguide with a single-mode channel expanded to a broad channel via an adiabatic taper [93] and more recently with Er^{3+} [94]. The broad multi-mode channel can be pumped by a non-diffraction-limited source and in principle can have a reasonable overlap with the fundamental laser mode defined by adiabatically expanding the single-mode channel. Power scaling to the Watt level with a high-brightness diode-pump source is foreseeable and discussed in the future works section.

1.5 Synopsis

Following this introduction the rest of the thesis is presented as follows. Chapter 2 details the theory used in describing the performance of the planar waveguide lasers investigated. The chapter is divided three sections, the first general laser performance theory, followed by thermal modelling, and last waveguide theory in which the previous sections are applied to the primary structure investigated, i.e. the large-mode-area double-clad planar waveguide. Included, is a rate equation analysis, with spatial mode selection, a simple plane-wave model for side-pumped LMA PW lasers that accounts for active media exhibiting re-absorption loss and energy-transfer loss mechanisms, and a treatment of guided spatial modes accounting for refractive index profiles, which includes the difference associated with rare-earth doping. Chapters 3 and 4 contain experimental results corresponding to end-pumping schemes, with the earlier related to the operation of CW Neodymium and Erbium doped LMA PW lasers; the latter, passively Q-switched Ytterbium and Neodymium-doped structures. Chapter 5 describes experiments performed using a side-pumped geometry with Thulium and Neodymium-doped LMA PW structures. Several resonator configurations were trialled and their performance discussed. Conclusions and discussion of future work are presented in the final chapter.

1.6 References

[1] E. Snitzer, *Physics Review Letters*, vol. 7, pp. 175 -177, 1961.

[2] C. L. Bonner, C. T. A. Brown, D. P. Shepherd, W. A. Clarkson, A. C. Tropper, D. C. Hanna, and B. Ferrand, "Diode-bar end-pumped high-power Nd:$Y_3Al_5O_{12}$ planar waveguide laser," *Optics Letters*, vol. 23, pp. 942-944, 1998.

[3] U. Griebner, R. Grunwald, and H. Schonnagel, "Thermally bonded Yb : YAG planar waveguide laser," *Optics Communications*, vol. 164, pp. 185-190, 1999.

[4] C. L. Bonner, T. Bhutta, D. P. Shepherd, and A. C. Tropper, "Double-clad structures and proximity coupling for diode-bar- pumped planar waveguide lasers," *IEEE Journal of Quantum Electronics*, vol. 36, pp. 236-242, 2000.

[5] R. J. Beach, S. C. Mitchell, H. E. Meissner, O. R. Meissner, W. F. Krupke, J. M. McMahon, W. J. Bennett, and D. P. Shepherd, "Continuous-wave and passively Q-switched cladding-pumped planar waveguide lasers," *Optics Letters*, vol. 26, pp. 881-883, 2001.

[6] J. R. Lee, H. J. Baker, G. J. Friel, G. J. Hilton, and D. R. Hall, "High-average-power Nd : YAG planar waveguide laser that is face pumped by 10 laser diode bars," *Optics Letters*, vol. 27, pp. 524-526, 2002.

[7] U. Brauch, P. Loosen, and H. Opower, "High-power diode lasers for direct applications," in *High-Power Diode Lasers: Fundamentals, Technology, Applications*, vol. 78, *Topics in Applied Physics*, 2000, pp. 303-367.

[8] M. W. Sasnett, "Propagation of Multimode Laser Beams-The M^2 factor," in *The Physics and Technology of Laser Resonators*, D. R. Hall and P. E. Jackson, Eds. Bristol: Hilger: IOP Publishing, 1989, pp. 132-142.

[9] N. S. Kapany, *Fiber Optics: Principles and applications*. New York: Academic Press, 1967.

[10] G. Zeidler, "Optical waveguide technique with organic dye lasers," *Journal of Applied Physics*, vol. 42, pp. 884-5, 1971.

[11] R. D. Dupuis, "An Introduction to the Development of the Semiconductor-Laser," *IEEE Journal of Quantum Electronics*, vol. 23, pp. 651-657, 1987.

[12] J. Sebastian, G. Beister, F. Bugge, F. Buhrandt, G. Erbert, H. G. Hansel, R. Hulsewede, A. Knauer, W. Pittroff, R. Staske, M. Schroder, H. Wenzel, M. Weyers, and G. Trankle, "High-power 810-nm GaAsP-AlGaAs diode lasers with narrow beam divergence," *IEEE Journal of Selected Topics in Quantum Electronics*, vol. 7, pp. 334-339, 2001.

[13] G. Erbert, A. Barwolff, J. Sebastian, and J. Tomm, "High-power broad-area diode lasers and laser bars," in *High-Power Diode Lasers: Fundamentals, Technology, Applications*, vol. 78, *Topics in Applied Physics*, 2000, pp. 173-223.

[14] P. W. Smith, "A waveguide gas laser," *Applied Physics Letters*, vol. 18, pp. 152-154, 1971.

[15] A. D. Colley, H. J. Baker, and D. R. Hall, "Planar Wave-Guide, 1-kW CW, Carbon-Dioxide Laser-Excited by a Single Transverse RF Discharge," *Applied Physics Letters*, vol. 61, pp. 136-138, 1992.

[16] J. P. Wittke, "Thin-film lasers," *RCA Review*, vol. 33, pp. 674-94, 1972.

[17] R. V. Ramaswamy and R. Srivastava, "Ion-Exchanged Glass Wave-Guides - a Review," *Journal of Lightwave Technology*, vol. 6, pp. 984-1002, 1988.

[18] R. V. Schmidt and I. P. Kaminow, "Metal-diffused optical waveguides," *Applied Physics Letters*, vol. 25, pp. 458-460, 1974.

[19] P. J. Chandler, L. Zhang, and P. D. Townsend, "Ion-Implanted Wave-Guides in Laser Host Materials," *Nuclear Instruments & Methods in Physics Research*

Section B- Beam Interactions with Materials and Atoms, vol. 59, pp. 1223-1227, 1991.

[20] K. Miura, J. R. Qiu, H. Inouye, T. Mitsuyu, and K. Hirao, "Photowritten optical waveguides in various glasses with ultrashort pulse laser," *Applied Physics Letters*, vol. 71, pp. 3329-3331, 1997.

[21] M. Svalgaard, C. V. Poulsen, A. Bjarklev, and O. Poulsen, "Direct UV Writing of Buried Singlemode Channel Wave-Guides in Ge-Doped Silica Films," *Electronics Letters*, vol. 30, pp. 1401-1403, 1994.

[22] K. Kubodera, J. Nakano, K. Otsuka, and S. Miyazawa, "A slab waveguide laser formed of glass-clad $LiNdP_4O_{12}$," *Journal of Applied Physics*, vol. 49, pp. 65-68, 1978.

[23] M. Kawachi, "Silica Wave-Guides on Silicon and Their Application to Integrated-Optic Components," *Optical and Quantum Electronics*, vol. 22, pp. 391-416, 1990.

[24] I. Chartier, B. Ferrand, D. Pelenc, S. J. Field, D. C. Hanna, A. C. Large, D. P. Shepherd, and A. C. Tropper, "Growth and Low-Threshold Laser Oscillation of an Epitaxially Grown Nd YAG Wave-Guide," *Optics Letters*, vol. 17, pp. 810-812, 1992.

[25] C. T. A. Brown, C. L. Bonner, T. J. Warburton, D. P. Shepherd, A. C. Tropper, D. C. Hanna, and H. E. Meissner, "Thermally bonded planar waveguide lasers," *Applied Physics Letters*, vol. 71, pp. 1139-1141, 1997.

[26] D. C. Hanna, A. C. Large, D. P. Shepherd, A. C. Tropper, I. Chartier, B. Ferrand, and D. Pelenc, "A Side-Pumped Nd-YAG Epitaxial Wave-Guide Laser," *Optics Communications*, vol. 91, pp. 229-235, 1992.

[27] A. Faulstich, H. J. Baker, and D. R. Hall, "Diode Pumped, thin slab solid state lasers," presented at Advanced Solid State Lasers, 1995.

[28] D. Pelenc, B. Chambaz, I. Chartier, B. Ferrand, C. Wyon, D. P. Shepherd, D. C. Hanna, A. C. Large, and A. C. Tropper, "High Slope Efficiency and Low-Threshold in a Diode-Pumped Epitaxially Grown Yb-YAG Wave-Guide Laser," *Optics Communications*, vol. 115, pp. 491-497, 1995.

[29] U. Griebner, H. Schonnagel, R. Grunwald, and S. Woggon, "Transversely guided pumped Yb:YAG laser," presented at Lasers and Electro-Optics 1997, 1997.

[30] D. P. Millas, A. Faulstich, H. J. Baker, and D. R. Hall, "A planar waveguide Nd:YAG laser, face pumped by laser diode bars," *Proceedings of the XI International Symposium on Gas Flow and Chemical Lasers and High Power Lasers '96*, vol. 3092, pp. 25-28, 1997.

[31] D. P. Shepherd, C. L. Bonner, C. T. A. Brown, W. A. Clarkson, A. C. Tropper, D. C. Hanna, and H. E. Meissner, "High-numerical-aperture, contact-bonded, planar waveguides for diode-bar-pumped lasers," *Optics Communications*, vol. 160, pp. 47-50, 1999.

[32] U. Griebner, R. Koch, H. Schonnagel, and R. Grunwald, "Efficient laser operation with nearly diffraction-limited output from a diode-pumped heavily Nd-doped multimode fiber," *Optics Letters*, vol. 21, pp. 266-268, 1996.

[33] U. Griebner and H. Schonnagel, "Laser operation with nearly diffraction-limited output from a Yb : YAG multimode channel waveguide," *Optics Letters*, vol. 24, pp. 750-752, 1999.

[34] H. J. Baker, J. R. Lee, and D. R. Hall, "Planar Waveguide Solid-State Lasers," presented at Conference on Lasers and Electro-Optics, 2002.

[35] J. Banerji, A. R. Davies, and R. M. Jenkins, "Laser resonators with self-imaging waveguides," *Journal of the Optical Society of America B-Optical Physics*, vol. 14, pp. 2378-2380, 1997.

[36] W. Pelouch, D. Smith, J. Koroshetz, I. McKinnie, J. Unternahrer, and S. Henderson, "High Power Self-Imaging Waveguide Lasers and Amplifiers," presented at OSA Trends in Optics and Photonics Vol. 68, Washington D.C., 2002.
[37] H. J. Baker, J. R. Lee, and D. R. Hall, "Self-imaging and high-beam-quality operation in multi-mode planar waveguide optical amplifiers," *Optics Express*, vol. 10, pp. 297-302, 2002.
[38] S. C. Tidwell, J. F. Seamans, C. E. Hamilton, C. H. Muller, and D. D. Lowenthal, "Efficient, 15-W Output Power, Diode-End-Pumped Nd-YAG Laser," *Optics Letters*, vol. 16, pp. 584-586, 1991.
[39] G. Cerullo, S. Desilvestri, and V. Magni, "High-Efficiency, 40-W CW Nd:YLF Laser with Large TEM_{00} Mode," *Optics Communications*, vol. 93, pp. 77-81, 1992.
[40] S. C. Tidwell, J. F. Seamans, and M. S. Bowers, "Highly Efficient 60-W TEM_{00} CW Diode-End-Pumped Nd-YAG Laser," *Optics Letters*, vol. 18, pp. 116-118, 1993.
[41] D. Golla, S. Knoke, W. Schone, G. Ernst, M. Bode, A. Tunnermann, and H. Welling, "300-W CW Diode-Laser Side-Pumped Nd-YAG Rod Laser," *Optics Letters*, vol. 20, pp. 1148-1150, 1995.
[42] D. Golla, M. Rode, S. Knoke, W. Schone, and A. Tunnermann, "62-W CW TEM_{00} Nd:YAG laser side-pumped by fiber-coupled diode lasers," *Optics Letters*, vol. 21, pp. 210-212, 1996.
[43] S. Konno, S. Fujikawa, and K. Yasui, "80 W CW TEM_{00} 1064 nm beam generation by use of a laser-diode- side-pumped Nd:YAG rod laser," *Applied Physics Letters*, vol. 70, pp. 2650-2651, 1997.
[44] K. Contag, M. Karszewski, C. Stewen, A. Giesen, and H. Hugel, "Theoretical modelling and experimental investigation of the diode-pumped thin-disk Yb : YAG laser (vol 29, pg 697, 1999)," *Quantum Electronics*, vol. 29, pp. 1025-1025, 1999.
[45] V. Dominic, S. MacCormack, R. Waarts, S. Sanders, S. Bicknese, R. Dohle, E. Wolak, P. S. Yeh, and E. Zucker, "110W fibre laser," *Electronics Letters*, vol. 35, pp. 1158-1160, 1999.
[46] Y. Hirano, Y. Koyata, S. Yamamoto, K. Kasahara, and T. Tajime, "208-W TEM_{00} operation of a diode-pumped Nd : YAG rod laser," *Optics Letters*, vol. 24, pp. 679-681, 1999.
[47] G. D. Goodno, S. Palese, J. Harkenrider, and H. Injeyan, "Yb : YAG power oscillator with high brightness and linear polarization," *Optics Letters*, vol. 26, pp. 1672-1674, 2001.
[48] J. Limpert, A. Liem, H. Zellmer, and A. Tunnermann, "Continuous-wave ultra high-brightness fiber laser systems," presented at Advanced Solid State Photonics, San Antonio, Texas, USA, 2003.
[49] R. J. StPierre, D. W. Mordaunt, H. Injeyan, J. G. Berg, R. C. Hilyard, M. E. Weber, M. G. Wickham, G. M. Harpole, and R. Senn, "Diode array pumped kilowatt laser," *IEEE Journal of Selected Topics in Quantum Electronics*, vol. 3, pp. 53-58, 1997.
[50] D. S. Sumida, A. A. Betin, H. Bruesselbach, R. Byren, S. Matthews, R. Reeder, and M. S. Mangir, "Diode-pumped Yb : YAG catches up with Nd : YAG," *Laser Focus World*, vol. 35, pg. 63, 1999.
[51] E. C. Honea, R. J. Beach, S. C. Mitchell, J. A. Skidmore, M. A. Emanuel, S. B. Sutton, S. A. Payne, P. V. Avizonis, R. S. Monroe, and D. G. Harris, "High-power dual-rod Yb : YAG laser," *Optics Letters*, vol. 25, pp. 805-807, 2000.

[52] C. Stewen, K. Contag, M. Larionov, A. Giesen, and H. Hugel, "A 1-kW CW thin disc laser," *IEEE Journal of Selected Topics in Quantum Electronics*, vol. 6, pp. 650-657, 2000.
[53] W. Koechner, *Solid State Laser Engineering - Chapter 2*, vol. 1, 4th ed. Berlin Heidelberg: Springer Verlag, 1999.
[54] A. A. Kaminskii, *Laser Crystals - Chapter 1*, vol. 14, Berlin Heidelberg: Springer Verlag, 1990.
[55] A. A. Kaminskii, *Laser Crystals - Chapter 4*, vol. 14, Berlin Heidelberg: Springer Verlag, 1990.
[56] W. Koechner, *Solid State Laser Engineering - Chapter 7*, vol. 1, 4th ed. Berlin Heidelberg: Springer Verlag, 1999.
[57] S. Fujikawa, T. Kojima, and K. Yasui, "High-power and high-efficiency operation of a CW-Diode-Side-Pumped Nd:YAG rod laser," *IEEE Journal of Selected Topics in Quantum Electronics*, vol. 3, pp. 40-44, 1997.
[58] E. C. Honea, R. J. Beach, S. B. Sutton, J. A. Speth, S. C. Mitchell, J. A. Skidmore, M. A. Emanuel, and S. A. Payne, "115-W Tm:YAG diode-pumped solid-state laser," *IEEE Journal of Quantum Electronics*, vol. 33, pp. 1592-1600, 1997.
[59] W. A. Clarkson, "Thermal effects and their mitigation in end-pumped solid-state lasers," *Journal of Physics D-Applied Physics*, vol. 34, pp. 2381-2395, 2001.
[60] D. C. Hanna, M. J. McCarthy, and P. J. Suni, "Thermal considerations in longitudinally pumped fibre and miniature lasers," *SPIE: Fiber Laser Sources and Amplifiers*, vol. 1171, pp. 160, 1989.
[61] M. K. Davis, M. J. F. Digonnet, and R. H. Pantell, "Thermal effects in doped fibers," *Journal of Lightwave Technology*, vol. 16, pp. 1013-1023, 1998.
[62] J. M. Eggleston, T. J. Kane, K. Kuhn, J. Unternahrer, and R. L. Byer, "The Slab Geometry Laser - Part 1. Theory," *IEEE Journal of Quantum Electronics*, vol. 20, pp. 289-301, 1984.
[63] K. M. Du, N. L. Wu, J. D. Xu, J. Giesekus, P. Loosen, and R. Poprawe, "Partially end-pumped Nd : YAG slab laser with a hybrid resonator," *Optics Letters*, vol. 23, pp. 370-372, 1998.
[64] J. L. Blows, J. M. Dawes, and J. A. Piper, "A simple, thermally-stabilised, diode end-pumped, planar Nd : YAG laser," *Optics Communications*, vol. 162, pp. 247-250, 1999.
[65] T. S. Rutherford, W. M. Tulloch, E. K. Gustafson, and R. L. Byer, "Edge-pumped quasi-three-level slab lasers: Design and power scaling," *IEEE Journal of Quantum Electronics*, vol. 36, pp. 205-219, 2000.
[66] A. Giesen, H. Hugel, A. Voss, K. Wittig, U. Brauch, and H. Opower, "Scalable Concept for Diode-Pumped High-Power Solid-State Lasers," *Applied Physics B-Lasers and Optics*, vol. 58, pp. 365-372, 1994.
[67] K. Contag, M. Karszewski, C. Stewen, A. Giesen, and H. Hugel, "Theoretical modelling and experimental investigations of the diode-pumped thin-disk Yb:YAG laser," *Quantum Electronics*, vol. 29, pp. 697-703, 1999.
[68] R. Weber, B. Neuenschwander, and H. P. Weber, "Thermal effects in solid-state laser materials," *Optical Materials*, vol. 11, pp. 245-254, 1999.
[69] M. Tsunekane, N. Taguchi, T. Kasamatsu, and H. Inaba, "Analytical and experimental studies on the characteristics of composite solid-state laser rods in diode-end-pumped geometry," *IEEE Journal of Selected Topics in Quantum Electronics*, vol. 3, pp. 9-18, 1997.

[70] M. Tsunekane, N. Taguchi, and H. Inaba, "Reduction of thermal effects in a diode-end-pumped, composite Nd : YAG rod with a sapphire end," *Applied Optics*, vol. 37, pp. 3290-3294, 1998.

[71] R. Weber, B. Neuenschwander, M. Mac Donald, M. B. Roos, and H. P. Weber, "Cooling schemes for longitudinally diode laser-pumped Nd : YAG rods," *IEEE Journal of Quantum Electronics*, vol. 34, pp. 1046-1053, 1998.

[72] L. Zenteno, "High-Power Double-Clad Fiber Lasers," *Journal of Lightwave Technology*, vol. 11, pp. 1435-1446, 1993.

[73] N. S. Platonov, D. V. Gapontsev, V. P. Gaponstev, and V. Shumilin, "135W CW Fiber Laser with Perfect Single Mode Output," presented at Conference on Lasers and Electro-Optics, Long Beach, CA, USA, 2002.

[74] K. Ueda, H. Sekigguchi, and H. Kan, "kW fiber lasers for industrial applications," presented at OSA Trends in Optics and Photonics Vol. 68, Washington D.C., 2002.

[75] W. Koechner, *Solid State Laser Engineering - Chapter 1*, vol. 1, 4th ed. Berlin Heidelberg: Springer Verlag, 1999.

[76] D. C. Hanna, C. G. Sawyers, and M. A. Yuratich, "Telescopic Resonators for Large-Volume TEM_{00}-Mode Operation," *Optical and Quantum Electronics*, vol. 13, pp. 493-507, 1981.

[77] J. Richards and A. McInnes, "Versatile, efficient, diode-pumped miniature slab laser," *Optics Letters*, vol. 20, pp. 371-373, 1995.

[78] J. Harrison, P. F. Moulton, and G. A. Scott, "13-W, M^2<1.2 Nd:YLF Laser Pumped by a Pair of 20-W Diode-Laser Bars," *CLEO '95, Postdeadline Paper*, 1995.

[79] A. E. Siegmann, "Unstable Optical Resonators," *Applied Optics*, vol. 13, pp. 353-367, 1974.

[80] K. J. Snell, D. Lee, K. F. Wall, and P. F. Moulton, "Diode-Pumped, High-Power CW and Mode-Locked Nd:YLF Lasers," *OSA Trends in Optics and Photonics: Advanced Solid State Lasers*, vol. 34, pp. 55-58, 2000.

[81] W. A. Clarkson and D. C. Hanna, "Two-mirror beam-shaping technique for high-power diode bars," *Optics Letters*, vol. 21, pp. 375-377, 1996.

[82] B. Ehlers, K. Du, M. Baumann, H.-G. Treusch, P. Loosen, and R. Proprawe, "Beam shaping and fiber coupling of high-power diode laser arrays," *Proceedings of SPIE: Lasers in Material Processing*, vol. 3097, pp. 639-644, 1997.

[83] S. Bedo, W. Luthy, and H. P. Weber, "The Effective Absorption-Coefficient in Double-Clad Fibers," *Optics Communications*, vol. 99, pp. 331-335, 1993.

[84] H. L. Offerhaus, N. G. Broderick, D. J. Richardson, R. Sammut, J. Caplen, and L. Dong, "High-energy single-transverse-mode Q-switched fiber laser based on a multimode large-mode-area erbium-doped fiber," *Optics Letters*, vol. 23, pp. 1683-1685, 1998.

[85] D. Taverner, D. J. Richardson, L. Dong, J. E. Caplen, K. Williams, and R. V. Penty, "158-mu J pulses from a single-transverse-mode, large-mode-area erbium-doped fiber amplifier," *Optics Letters*, vol. 22, pp. 378-380, 1997.

[86] H. Weichel and L. S. Pedrotti, "A summary of useful laser equations - An LIA report," Electro-Optical Systems Design - The Engineering Magazine of Electro-Optical and Laser Technology, LIA Report.

[87] A. E. Siegmann, *Lasers - Chapter 22*, 1st ed. New York: University Science Books, 1986.

[88] V. Daneu, A. Sanchez, T. Y. Fan, H. K. Choi, G. W. Turner, and C. C. Cook, "Spectral beam combining of a broad-stripe diode laser array in an external cavity," *Optics Letters*, vol. 25, pp. 405-407, 2000.

[89] E. J. Bochove, "Theory of spectral beam combining of fiber lasers," *IEEE Journal of Quantum Electronics*, vol. 38, pp. 432-445, 2002.
[90] J. R. Leger, "Lateral-Mode Control of an AlGaAs Laser Array in a Talbot Cavity," *Applied Physics Letters*, vol. 55, pp. 334-336, 1989.
[91] M. Wrage, P. Glas, D. Fischer, M. Leitner, D. V. Vysotsky, and A. P. Napartovich, "Phase locking in a multicore fiber laser by means of a Talbot resonator," *Optics Letters*, vol. 25, pp. 1436-1438, 2000.
[92] M. Wrage, P. Glas, and M. Leitner, "Combined phase locking and beam shaping of a multicore fiber laser by structured mirrors," *Optics Letters*, vol. 26, pp. 980-982, 2001.
[93] S. J. Hettrick, J. I. Mackenzie, R. D. Harris, J. S. Wilkinson, D. P. Shepherd, and A. C. Tropper, "Ion-exchanged tapered-waveguide laser in neodymium-doped BK7 glass," *Optics Letters*, vol. 25, pp. 1433-1435, 2000.
[94] P. Madasamy, S. Honkanen, D. F. Geraghty, and N. Peyghambarian, "Single-mode tapered waveguide laser in Er-doped glass with multimode-diode pumping," *Applied Physics Letters*, vol. 82, pp. 1332-1334, 2003.

Chapter 2

MODELLING THEORY

2.1 Introduction

Presented in this chapter are some of the theoretical aspects underlying the experimental data and future directions detailed in this thesis. Firstly, two separate methods for predicting laser performance are introduced; these analyses are later applied to the large-mode-area double-clad planar waveguide laser. To start, following on from that reported by Risk [1], the results of a spatially-dependent rate-equation model are described. An expression for the population inversion density is derived that accounts for a non-uniform doping distribution, reabsorption loss at the laser wavelength, and gain saturation by the oscillating field. The second modelling approach, based upon a simpler plane wave analysis originally proposed by Beach [2] for end-pumped quasi-three-level lasers, was developed for side-pumped active media. This latter technique is a good approximation for the plane-wave nature of guided radiation and does not require detailed knowledge of the pump or laser field distributions. The model also allows for ground state depletion, gain saturation, and an effective determination of the output channels into which the absorbed pump power is distributed. Furthermore, this extension to Beach's approach includes upconversion and cross-relaxation, examples of excited-state energy transfer processes.

The thermal characteristics of an excited gain medium in conjunction with high power solid-state lasers is of particular importance, thus methods to predict the effects of heat flow in the planar waveguide laser are introduced. Applicable to the end-pumped double-clad waveguide structure, is a model originally developed by Joyce and Dixon [3] for semiconductor hetero-structure lasers. This analysis is used to calculate the temperature rise and in-plane profile, at the centre of the waveguide core and along the length of the crystal structure. Alternatively for the side-pumped geometry the thermal load in the planar waveguide can be relatively uniform, resulting in a situation resembling that of an infinite slab heat source [4]. Therefore, the thermal gradients can be assumed one-dimensional (1D) and perpendicular to the plane. This model is used to calculate the 1D

temperature distribution, average temperature rise, and a figure of merit relating the induced stress component under high-power operation and maximum tensile strength of the composite structure.

Finally, the theoretical guided mode profiles of the double-clad planar waveguide are described. The composite structures investigate herein were fabricated using layers of sapphire as the outer cladding, YAG for the inner cladding, and a rare-earth doped-YAG core. A refractive index difference between the rare-earth-doped core and inner cladding layers is responsible for producing a weak inner guide, the effect of which is discussed with regard to these composite waveguides and the rare-earth ions. An important factor governing the design of the LMA planar waveguide is the effective absorption length for the pump radiation. A simple rule that the absorption length scales according to the ratio of the doped core thickness to the separation of the outer cladding layers is demonstrated to be a reasonable approximation. Finally combining the general rate equation analysis introduced above and the spatial characteristics of the pump and laser fields for a double-clad waveguide, the phenomenon of gain-mode selection is obtained. When applied to the LMA PW laser, doping ratio[ix] limits imposed by the real refractive index profiles are observed.

2.2 Laser performance modelling

2.2.1 Spatial rate-equation analysis

In this section a steady-state spatial rate equation analysis is applied to a non-uniformly doped active material, of which the LMA PW is one example, to determine the relative gain for the individual cavity or waveguide modes and subsequent laser performance. With careful design of the doping profile, it is shown that the fundamental mode can be robustly maintained even at extremely high intra-cavity laser intensity levels. This characteristic is discussed in greater detail toward the end of the chapter when applied to the LMA PW laser, including the effects of an index step about the core layer.

Many authors have modelled laser system performance through the use of spatially dependent rate equations for uniformly doped active materials [1, 5-7]. The effect of a

[ix] Ratio of the thickness of the doped to un-doped layers.

non-uniform doping distribution has also been studied in the context of a fibre amplifier [8] and fibre laser [9]. Here a general analysis for a non-uniformly doped active medium is described, which is applicable to continuous-wave laser oscillators.

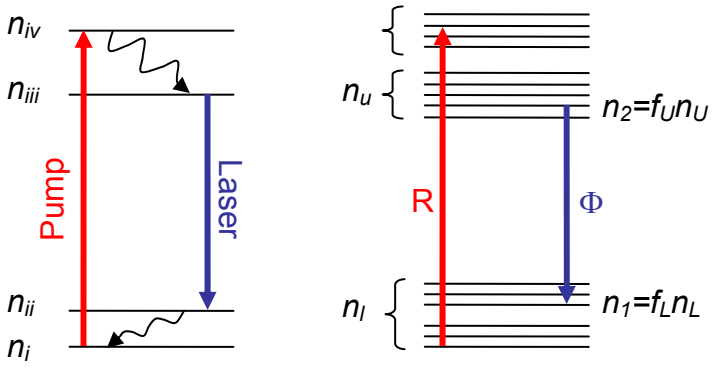

Figure 2.1: General energy scheme for quasi-three or four level laser system.

A general energy level scheme for an activated crystalline host is shown in Figure 2.1, which allows for the possibility of a non-zero population in the lower laser level energy manifold, n_l, i.e. a quasi-three-level transition. Following the analysis and assumptions of Risk [1], the steady-state rate of change of the population inversion density $\Delta N(x,y,z)=N_2(x,y,z)-N_1(x,y,z)$ above threshold, is given by,

$$\frac{d\Delta N(x,y,z)}{dt} = fRr(x,y,z)d(x,y,z) - \frac{\Delta N(x,y,z)-\Delta N^0(x,y,z)}{\tau} - \frac{fc\sigma\,\Delta N(x,y,z)\Phi\phi(x,y,z)}{n} = 0 \qquad \textbf{(2.1).}$$

where a normalised spatial doping profile $d(x,y,z)$, is introduced to distinguish it from the normalised pump distribution $r(x,y,z)$. The population inversion density is created by a pumping rate $R = \eta_{abs} P_p / h\nu_p$ for an incident pump power P_p with absorption efficiency η_{abs} and pump photon energy $h\nu_p$, f is the sum of the occupation factors for the upper (f_U) and lower (f_L) laser Stark levels [1], ΔN^0 is the un-pumped population inversion density, σ is the spectroscopic emission cross section, which is referenced to the Stark levels coupled by the laser photons, τ the lifetime of the upper laser-level manifold, c is the speed of light, n is the refractive index of the active medium at the laser wavelength, Φ is the total number of intra-cavity laser photons, given by $\Phi=2l_{cav}P_l/ch\nu_l$, with the one-way intra-

cavity laser power P_l, l_{cav} the optical cavity length, $h\nu_l$ the lasing photon energy, and finally $\phi(x,y,z)$ is the normalised laser photon distribution.

Equation (2.1) can be rearranged to obtain,

$$\Delta N(x,y,z) = \frac{f\tau Rr(x,y,z) - n_1^0 d(x,y,z)}{1 + S\phi(x,y,z)}$$

(2.2).

Thus the population inversion density is created by the pumping rate less any residual population in the terminal laser Stark level n_1^0, and is further modified by the saturating laser power through the parameter, S. That is $S = fc\sigma\tau\Phi/n$ gives a measure of the degree of saturation caused by the intra-cavity laser power.

The doping distribution, the pump and lasing photon distributions are normalised with respect to the cavity volume, such that

$$\iiint_{cavity} r(x,y,z)dV = \iiint_{cavity} \phi(x,y,z)dV = \iiint_{cavity} d(x,y,z)dV = 1$$

(2.3).

Taking into account these spatial distributions and noting that outside of the active crystal the population inversion density is zero, the normal steady-state laser condition that the gain is equal to the loss is written as,

$$\frac{2\sigma\, l_{cav}}{n} \iiint_{crystal} \Delta N(x,y,z)\phi(x,y,z)dV = L - \ln(R_l^{oc})$$

(2.4)

where L is the round-trip loss exponent and R_l^{oc} is the output coupler reflectivity at the laser wavelength. By substituting equation (2.3) into equation (2.4) it is found that,

$$\frac{2\sigma\, l_{cav}}{n(L - \ln(R_l^{oc}))} \iiint_{crystal} \frac{(f\tau Rr(x,y,z) - n_1^0 d(x,y,z))\phi(x,y,z)}{1 + S\phi(x,y,z)} dV = 1$$

(2.5)

Equation (2.5) can be re-arranged to express the pump excitation rate R in terms of the losses and the laser power, such that,

$$R = \frac{n\left(L - \ln(R_l^{oc})\right) + 2l_{cav}\sigma\, n_1^o I_d}{2l_{cav}\sigma\tau I_r}$$

where: $$I_d = \iiint_{crystal} \frac{d(x,y,z)\phi(x,y,z)}{1 + S\phi(x,y,z)} dV \text{ and } I_r = \iiint_{crystal} \frac{r(x,y,z)\phi(x,y,z)}{1 + S\phi(x,y,z)} dV$$

(2.6).

Substituting equation (2.6) back into equation (2.2) leads to a description of the change in the inversion profile for various levels of oscillating field saturation,

$$\Delta N(x,y,z) = \frac{n(L - \ln(R_l^{oc}))r(x,y,z)}{2l_{cav}\sigma\,(1 + S\phi(x,y,z))I_r} + n_1^o\left[\frac{r(x,y,z)I_d - d(x,y,z)I_r}{(1 + S\phi(x,y,z))I_r}\right]$$

(2.7).

Now the gain for any particular cavity or waveguide mode, G_p, with a spatial profile $\phi_p(x,y,z)$ saturated by a lasing mode of profile $\phi(x,y,z)$ is given by,

$$G_p = \frac{2l_{cav}\sigma}{n} \iiint_{crystal} \Delta N(x,y,z)\phi_p(x,y,z) dV$$

(2.8)

with $\Delta N(x,y,z)$ coming from equation (2.7). Therefore, in the general case the saturated inversion depends upon the size of the un-pumped population in the lower laser level. Hence, spatial-mode selectivity will also, depend on whether the lasing transition is 3 or 4-level in nature, as will be discussed in section 2.4.5.

With knowledge of the relevant spatial distributions, it is possible to solve equation (2.5) using equation (2.7) to find the lasing power as a function of pump power. Similarly, it can be used to find the optimum output coupling for a particular cavity configuration.

2.2.2 Plane-wave analysis

To model a laser system whose spatial distributions for either the laser or pump radiation are unknown, equation (2.5) is not suitable. Consequently a method such as a Rigrod analysis [10] or a simpler energy transfer model is required to predict its performance; as such a plane wave model applicable to side-pumped, highly multi-mode LMA PW lasers was required. Such a method was derived by modifying a model presented by Beach [2] for end-pumped quasi-three-level laser oscillators, which accounts for ground-state depletion and gain saturation. Other energy transfer mechanisms such as cross-relaxation,

and upconversion were also incorporated, as will be demonstrated. In addition the modelling allows simple identification of the de-excitation routes taken by the excited active medium, such as thermal loading of the crystal or fluorescence. This is particularly important in the case of high-power lasers where thermal or even upconversion effects can severely degrade their performance.

The premise for the plane-wave analysis is that the excited ion population is imagined to be in a single upper laser manifold whilst the remaining population is in the lower or ground state. Therefore changes in the population levels are defined by excitation and de-excitation rates from the lower and upper levels respectively, as illustrated in Figure 2.2, and imposing the law of energy conservation in a steady-state regime implies that the energy transfer channels must be equivalent. The result leads to the determination of the input and output energy paths for the laser system, one of which is laser output power.

Firstly, assuming that all of the active ions (n_0) are either in the upper (U) or lower (L) energy states, gives $n_0 = n_L + n_U$. Note the levels $n_{i,ii}$ in Figure 2.2 may in fact be Stark levels within a single energy manifold, similarly for $n_{iii,iv}$, which for example, corresponds to the ^{2}F electronic state of the trivalent rare earth ion, Yb^{3+}.

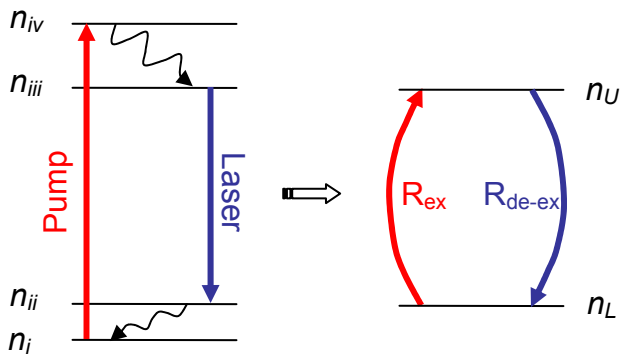

Figure 2.2: General energy scheme for a laser system and the equivalent two-level model accounting for an excitation and de-excitation rate between the upper and lower levels coupling the laser radiation.

2.2.2.1 Rate of excitation

In the side-pumped configuration, the fraction of incident pump power delivered to the active medium that is absorbed in a single pass across the width of the crystal, w, can be defined as,

$$F_A = 1 - e^{\left(-\sigma_p \eta_{po} \int_0^w f_L^p n_L - f_U^p n_U dx\right)}$$

(2.9)

where σ_p is the spectroscopic absorption cross section at the pump wavelength, η_{po} represents the overlap of the pump radiation and the doped volume of the active medium (discussed further in relation to the LMA waveguide later in this chapter, section 2.4.4), $f_L{}^{p}{}_{(U)}$ corresponds to the Stark level Boltzmann occupation factors for the lower (upper) energy manifold, the x-axis corresponds to integration across the width of the crystal, and $n_{L,(U)}$ is the population density of the lower (upper) laser manifold, assuming all the population lies within the two levels involved, it is possible to write,

$$f_U^p n_U - f_L^p n_L = f^p n_U - f_L^p n_0$$

(2.10)

Here, n_0 is the active-ion dopant density and $f^p = f_L{}^p + f_U{}^p$ is a compact notation for the sum of Stark level occupation factors in the lower and upper manifolds coupled by the pump radiation. It is useful now to define the integrated upper level population density, N_U, with respect to the active material length, l, which it will be shown can be easily obtained from the gain equal loss relationship at threshold, thus

$$N_U = \int_0^l n_U \, dz$$

(2.11).

Noting the relatively uniform pump distribution associated with side-pumping, the integrated inversion density with respect to the gain volume width, w, and referenced to the manifold Stark levels coupled by the pump radiation, can be written as

$$N_U^p = f^p N_U \frac{w}{l} - f_L^p n_0 w$$

(2.12),

therefore the fractional absorption becomes,

$$F_A = 1 - e^{\eta_{po} \sigma_p N_U^p}$$

(2.13)

Leaving the rate at which the active ions are promoted into the upper laser level, for a single pass pumping configuration, to be given by,

$$R_{ex} = \eta_{QY}\eta_{del}\frac{P_p}{h\nu_p}F_A$$

(2.14)

where η_{QY} is the quantum yield efficiency for the laser system, representing the number of electrons in the upper laser level per pump photon delivered to the active material, the latter is governed by the delivery efficiency, η_{del}, i.e. the percentage of the pump radiation coupled into the active medium.

2.2.2.2 Rate of de-excitation

Using a similar argument as in the previous section, the fraction of laser power absorbed in a single pass along the length of the gain volume, l is,

$$F_B = -\left(1 - e^{\left(-\eta_{lo}\sigma_l \int_0^l \left(f_L^l n_L - f_U^l n_U\right) dz\right)}\right)$$

(2.15)

here σ_l is the spectroscopic stimulated emission cross section for the laser transition, η_{lo} is the overlap of the oscillating field with the active volume, $f_{L(U)}^{l}$ is the lower (upper) laser Stark level occupation factor, and the z-axis corresponds to integration along the length of the crystal. The negative sign in front of equation (2.15) indicates that the process is one of emission rather than absorption. As before, noting that all the population is in either of the two levels involved in the laser transition gives,

$$f_U^l n_U - f_L^l n_L = f^l n_U - f_L^l n_0$$

(2.16)

where $f^l = f_L{}^l + f_U{}^l$ is a compact notation for the sum of Stark-level occupation factors in the lower and upper manifolds coupled by the laser radiation.

The integrated inversion density with respect to the crystal length, and referenced to the manifold Stark levels coupled by the laser radiation, is defined to be

$$N_U^l = f^l N_U - f_L^l n_0 l$$

(2.17)

from which,

$$F_B = e^{\eta_{lo}\sigma_l N_U^l} - 1$$

(2.18).

By tracing the laser output power, P_{out}, reflected back from the output coupler mirror through the cavity, and assuming that the propagation losses can be lumped into a one-way cavity transmission, T_{sp}, located at the high reflector, the de-excitation rate is given by,

$$R_{de-ex} = \frac{P_{out}}{\eta_{Mode} h\nu_l}\left(\frac{R_l^{oc}}{1-R_l^{oc}}\right)F_B\left(1+T_{sp}^2 e^{\eta_{lo}\sigma_l N_U^l}\right)+\frac{N_U wt_{core}}{\tau_{eff}}$$

(2.19)

With η_{Mode} representing the fill factor of the laser beam with respect to cross sectional area of the excited volume, t_{core} is the thickness of the doped region, and τ_{eff} is the effective emission lifetime of the upper level dependent upon radiative and non-radiative decay in addition to other excited state energy transfer mechanisms, such as upconversion and cross relaxation.

Equating equations (2.14) and (2.19), it is possible to derive the laser output power, threshold and slope efficiency. Therefore the output power of the laser is related to the incident pump power, P_p, by

$$P_{out} = \eta_{slope}(P_p - P_{th})$$

(2.20)

where the slope efficiency, η_{slope}, with respect to the incident pump power, for a single pass of the pump, is

$$\eta_{slope} = \eta_{QY}\eta_{Mode}\eta_{del}\frac{\nu_l}{\nu_p}\left(\frac{1-R_l^{oc}}{R_l^{oc}}\right)\left(\frac{F_A}{F_B(1+T_{sp}^2 e^{\eta_{lo}\sigma_l N_U^l})}\right)$$

(2.21)

and the threshold incident power, P_{th}, is

$$P_{th} = \frac{h\nu_p}{\eta_{QY}\eta_{del}\tau_{eff}}\left(\frac{N_U wt_{core}}{F_A}\right)$$

(2.22).

2.2.2.3 Excited-state population density

In order to calculate equations (2.20) - (2.22) it is also necessary to find the integrated excited-state population density, N_U. Under steady-state conditions this is calculated using the gain equal to loss expression, that is

$$T_{sp}^2 R_l^{oc}\, e^{2\eta_{lo}\sigma_l N_U^l} = 1 \tag{2.23}$$

Re-arranging equation (2.23) and using equation (2.17) leads to the final expression

$$N_U = \frac{1}{f^l}\left(\frac{1}{2\eta_{lo}\sigma_l}\ln\left(\frac{1}{T_{sp}^2 R_l^{oc}}\right) + f_L^l n_o l\right) \tag{2.24}$$

2.3 Thermal modelling

2.3.1 Thermal modelling - end pumping

In high-power end-pumped solid-state lasers, thermal management is of considerable importance for beam quality, efficiency, and scalability [11]. A key parameter in this problem is the thermal resistance between the heat source and its surrounds. The temperature rise and distribution within the active material, depends upon the absorbed pump power contributing to heat, its distribution, the heat-sink geometry, and of course the thermal conductivity of the host. To verify whether the thermal characteristics of the LMA PW laser are an improvement over its bulk counterparts and to determine the expected temperature rises associated with end-pumping, a model was developed that accounted for the composite's properties.

For the composite structure illustrated in Figure 2.3, it should be noted that the thermal conductivity is not necessarily equal for the individual layers between the heat source and sink. When coupled with the fact that under pumped conditions the heat source is confined to a thin stripe in a waveguide core, the thermal resistance and in-plane temperature distribution may be calculated by applying a model originally developed for semiconductor hetero-structure lasers by Joyce and Dixon [3]. Assumptions for this model are; (1) the uniform heat source is an infinitesimally thin planar rectangular stripe within a layered structure, (2) there is a single conductive heat sink of constant temperature at the bottom surface, and (3) no heat escapes the side, end or top surfaces, representative of the

end-pumped structures investigated. Thus a two-dimensional (2D) heat flow is expected in the x-y plane, as illustrated by the dashed lines in Figure 2.3, and the thermal resistance of the overall structure determined; the results define an in-plane (x-z plane) temperature-difference profile between the heat sink and the centre of the active layer. Although Joyce and Dixon originally proposed this model for electrically pumped lasers with uniform current injection along the length of the hetero-structure, it is a simple matter to apply this analysis recursively to small increments along the length of the medium, accounting for longitudinal pumping and an exponentially decreasing heat source.

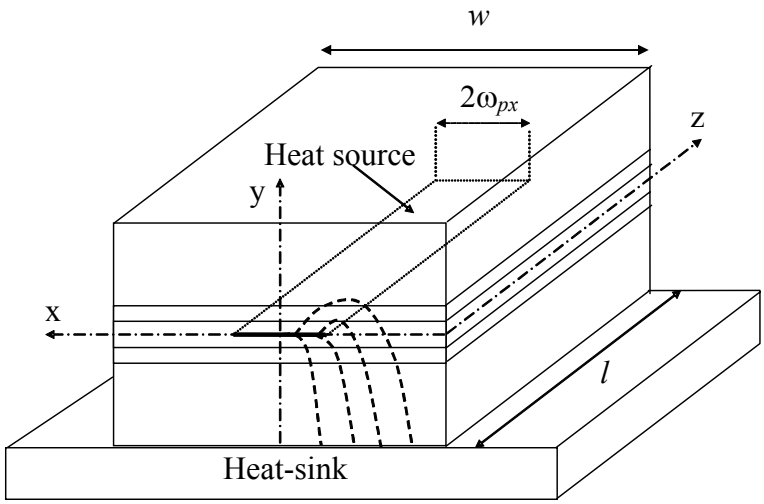

Figure 2.3: Schematic of a plane rectangular heat source at the centre of an active core in a double-clad LMA PW laser.

Joyce and Dixon develop their model starting with a separation-of-variables solution to Laplace's heat conduction equation as an appropriate form for the temperature distribution in the i^{th} layer of a hetero-structure [3], that is,

$$T_i(x,y) = \beta_{i,0}\left(1 - r_{i,0}y\right) + \sum_{m=1}^{\infty} \beta_{i,n}\left[\cosh(k_m y) - r_{i,m}\sinh(k_m y)\right]\cos(k_m x) \tag{2.25}$$

where the coefficients and constants are determined by a careful choice of the system coordinates (that is y in each layer increases from zero moving away from the heat source) and application of the boundary conditions listed in the above assumptions.

Consequently the in-plane temperature difference with respect to the heat sink, as a function of the thermal resistance *R(x)*, is determined at the heat source that is the centre of the active waveguide core, using

$$T_1(x,0) = R(x)P_h$$

(2.26)

where P_h is the heat deposited over the planar stripe area and the thermal resistance is given by,

$$R(x) = \sum_{m=1}^{M} \beta_{1,m} \cos(\kappa_m x), \qquad \kappa_m = \frac{2m\pi}{w}$$

(2.27).

Here $\beta_{1,m}$ is a coefficient derived from the fact that although the heat flux is an unknown function in x, the total heat flow from the planar heat source from both sides is constant and equal to $J = P_h/2\omega_{px}l$, the power per unit area for $|x| \le \omega_{px}$ and zero otherwise; ω_{px} is the half width of the rectangular heat source, and l its length. Using a Fourier series representation for the heat flux reveals,

$$\beta_{1,m} = \frac{2}{\omega_{px} l w \kappa_m^2} \frac{\sin(\kappa_m \omega_{px})}{(k_1 r_{1,m} + k_2 r_{2,m})}$$

(2.28).

Which involves, κ_m a separation constant for the Fourier series, w the full width of the composite structure, as indicated in Figure 2.3, k_1 and k_2 the thermal conductivities of the layers adjacent to the heat source that are respectively closer to and farther from the heat sink, as shown in Figure 2.4, and finally $r_{1,m}$ and $r_{2,m}$, are dimensionless series coefficients below and above the heat source respectively, determined using the listed boundary conditions, such that,

$$r_{i,m} = \frac{\tanh(\kappa_m t_i) + \left(\frac{k_{i+2}}{k_i}\right) r_{i,+2,m}}{1 + \left(\frac{k_{i+2}}{k_i}\right) \tanh(\kappa_m t_i)\, r_{i,+2,m}}, \qquad \begin{matrix} i = 1,3,\ldots,2b-1 \\ or \\ i = 2,4,\ldots,2a \end{matrix}$$

(2.29).

Where as shown in Figure 2.4, *i* denotes the layer number that is odd below or even above and increasing moving away from the heat source, thus there are *a* layers above (the uppermost layer numbered *2a*) and b layers below (the layer adjacent to the heat sink numbered *2b-1*); k_i is the thermal conductivity and t_i the thickness of the i^{th} layer. The definition of $r_{i,m}$ requires the boundary conditions at the outer surfaces of layers, $i = 2a$ and $2b\text{-}1$, be evaluated. Applying assumptions (3) and (2) to equation (2.25), i.e. at the uppermost surface no heat may escape, i.e. $\partial T_{2a}(y = t_{2a}) \big/ \partial y = 0$, and the surface adjacent to the highly conductive heat sink is held at a constant temperature $T_{2b-1}(y = t_{2b-1}) = 0$, (zero is used for simplicity, a linear offset from the actual heat sink temperature) gives,

$$r_{2a,m} = \tanh(\kappa_m t_{2a})$$
$$r_{2b-1,m} = \coth(\kappa_m t_{2b-1})$$

(2.30).

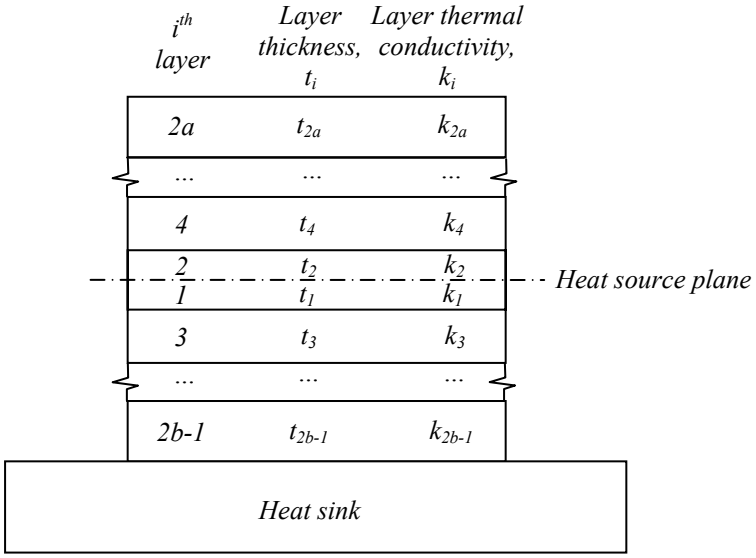

Figure 2.4: Cross section of the composite structure consisting of layers of dissimilar materials. The i^{th} layer is assigned a number as indicated, with a thickness, t_i, and a thermal conductivity, k_i.

Finally for $m = 0$ the $\beta_{1,0}$ coefficient is obtained directly from the Fourier series representation of the heat flux, where the leading term is independent of *x* and represents a 1D heat flow through the lower layers directly to the heat sink, given by,

$$\beta_{1,0} = \frac{P_h}{lw} \sum_i \frac{t_i}{k_i}, \qquad i = 1,3,\ldots,2b-1$$

(2.31).

To apply this model to the LMA PW laser, firstly the width of the heat source was assumed to be twice the average pump beam radius ω_{px} in the non-guided x-axis. Secondly, the absorbed power contributing to heat in the active medium over a small increment $\Delta z = z_2 - z_1$, was calculated using,

$$P_h(\Delta z) = \gamma P_p^0 \left(e^{-\alpha z_1} - e^{-\alpha z_2} + R_p^{oc} e^{-\alpha l} \left(e^{-\alpha (l - z_2)} - e^{-\alpha (l - z_1)} \right) \right) \tag{2.32}$$

where γ is the fraction of the absorbed pump contributing to heat, P_p^0 is the initial pump power launched into the waveguide, α is the absorption coefficient for the double-clad structure (see section 2.4.4), R_p^{oc} is the output mirror reflectance at the pump wavelength (hence allowing for back reflection of unabsorbed pump after one pass of the waveguide), and l is the length of the waveguide.

Applying this model in a recursive manner over the length of the waveguide, the induced temperature difference distribution in the plane as a function of x and z can be found. This is discussed further in Chapter 3.

2.3.2 Thermal modelling – side-pumping

An in-plane pumping scheme with the thermal load uniformly distributed throughout the entire waveguide core, approaches the case of a slab heat-source of infinite extent; corresponding to the high aspect ratio of the doped core to the waveguide width and length. Therefore the temperature gradient can be assumed to be 1D perpendicular to the plane, the solution for which has been discussed in detail by Eggleston *et al.* [4]. In their analysis the uniformly heated slab is in direct contact with the heat sink and cooling system, differing from the double-clad waveguide in that the core acts as the heat source, and the cladding layers, thermal resistance. Fortunately though, for the YAG/sapphire composite, planar structures can be fabricated with comparatively smaller overall thermal resistance than a single-crystal slab.

To determine the temperature distribution in the waveguide geometry, the heat conduction equation must be solved accounting for the boundary conditions, similar to that detailed in the previous section. Under steady-state pumping conditions (as discussed in this thesis) the time independent heat equation is given by [4],

$$\nabla^2 T(x,y,z) = \frac{-Q_T(x,y,z)}{k(x,y,z)}$$

(2.33).

The thermal load per unit volume, $Q_T(x,y,z)$ is assumed constant and equal to the uniformly deposited heat, P_h, over the volume of the active core, $t_{core}wl$. Furthermore, assuming that the heat flow is purely 1D perpendicular to the plane, implies equation (2.33) reduces to,

$$\frac{\partial^2 T(y)}{\partial y^2} = \frac{-P_h}{k(y)t_{core}wl}$$

(2.34).

Thus a general solution to equation (2.34) is shown in Figure 2.5, corresponding to the adjacent schematic diagram for the 5 layer composite structures investigated.

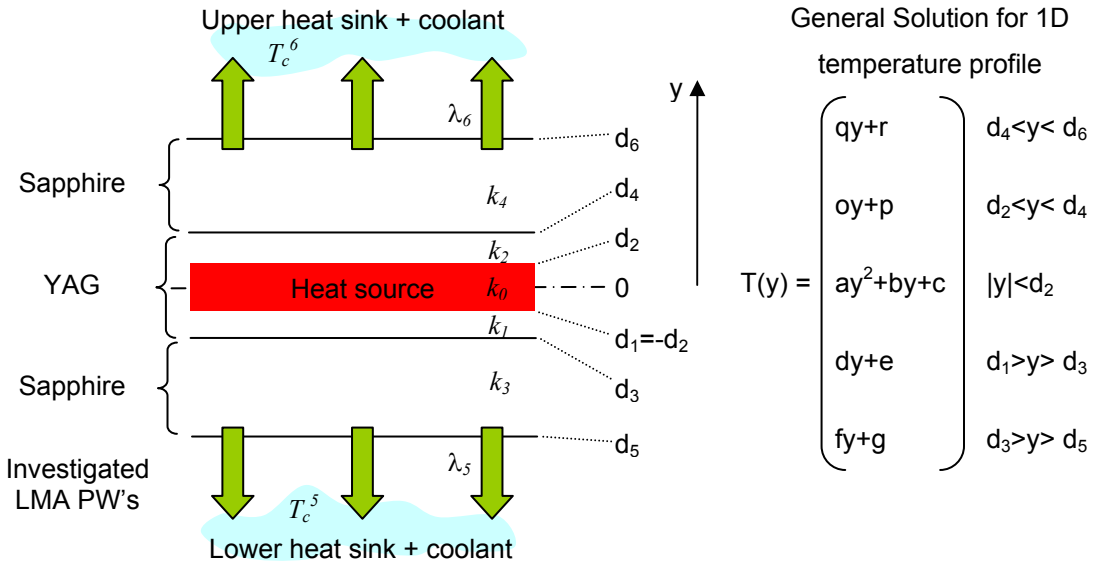

Figure 2.5: General structure and solution for modelling the 1D temperature profile in a double-clad waveguide

With reference to the schematic in Figure 2.5, the central layers are considered to be the same material (although in general this does not have to be the case) and only the inner core doped with an activator ion, becoming the source of heat when optically excited. It should be pointed out that each i^{th} layer is assumed isotropic in terms of its thermal conductivity, which is also assumed to be independent of temperature, therefore $k(y) = k_i$ for y contained by the i^{th} layer. In the composite structures investigated it is also

reasonable to expect that the boundary between each layer does not contribute additional thermal resistance, particularly as the fabrication technique requires the surfaces to be in intimate contact. The boundary conditions between the adjacent layers are therefore given by:

$$k_{i-2}\left.\frac{\partial T}{\partial y}\right|_{d_i} = k_i \left.\frac{\partial T}{\partial y}\right|_{d_i}, \quad for \quad i = 2,3,4$$
$$T_{i-2}\big|_{d_i} = T_i\big|_{d_i}$$

(2.35),

where the boundary surface position is indicated by d_i, i is the layer index, as indicated in Figure 2.5. Note for the case i=1 the first subscript index, i-2, is replaced by i-1. The upper statement in equation (2.35) states that the temperature gradient in adjacent layers is proportional through each layer's thermal conductivity, and the bottom is simply the continuity condition that the temperature either side of an infinitely thin boundary is equal.

The outer surfaces of the composite structure are assumed to be in contact with an actively cooled heat sink with the appropriate boundary condition then given by Newton's law of heat transfer [4],

$$k_{i-2}\left.\frac{\partial T}{\partial \hat{y}}\right|_{d_i} = \lambda_i\left(T_c^i - T_i\big|_{d_i}\right), \quad for \quad i = 5 \; or \; 6$$

(2.36)

here the coefficient of heat transfer, λ_i, is dependent upon the thermal interface between the waveguide and heat sink, including the latter's geometry [12], T_c^i is the coolant temperature, and finally $\hat{y}$ represents the outward unit-vector normal to the d_i boundary.

Therefore it simply becomes an algebraic problem to determine the coefficients of the general solution given in Figure 2.5, starting at the two boundaries adjacent the heat sinks and working toward the centre using equations (2.34)-(2.36).

To determine the stress induced by the thermal load in the composite slab, a temperature distribution with a zero mean temperature is required, given by:

$$T'(y) = T(y) - \frac{\int_{d_5}^{d_6} T(y)\,dy}{(d_6 - d_5)}$$

(2.37)

where *T(y)* is simply the solved form of the general equation given in Figure 2.5.

As detailed in [4], from the symmetry of the uniformly heated slab and application of the Airy Stress function, the induced stress component is found to be,

$$\sigma_s = \frac{E\alpha_T}{(1-\nu)} T'(y)$$

(2.38).

Here the first term comprises material properties, e.g. E is Young's modulus, α_T the thermal expansion coefficient, and ν, Poisson's ratio. Furthermore the maximum allowable surface stress before fracture occurs is given by:

$$\sigma_{\max} = \frac{R_s E\alpha_T}{(1-\nu)k_i} \quad , \quad for \quad i = 5 \; or \; 6$$

(2.39)

the term R_s is a thermal shock parameter [12], or thermal stress resistance parameter [4], essentially a figure of merit for the onset of stress fracture in a particular material. By taking the ratio of equations (2.39) and (2.38) another figure of merit relating the stress fracture limit to the induced stress is obtained, i.e,

$$F_\sigma = \frac{R_s}{k_i T'(d_i)} \quad , \quad for \quad i = 5 \; or \; 6$$

(2.40),

giving a simple expression for the margin of safety before stress fracture is expected in the composite structure.

2.4 Waveguide theory

2.4.1 Introduction to the slab waveguide

Guiding electromagnetic radiation is a well understood phenomenon, and for which there are many textbooks dedicated to its application in the optical regime, for example [13-16].

The simplest wave-guiding structure, the planar waveguide, being the primary focus of this study, achieves optical confinement through total internal reflection (TIR) at the interfaces between layers of higher refractive index bounded by lower index materials, as illustrated in Figure 2.6. Light, theoretically at least, may propagate through such structures without loss if the phase-fronts are reconstructed after undergoing two internal reflections from the upper and lower bounding interfaces. One method to account for the enforced phase relationship is to describe the propagating light with plane wave-fronts travelling at discrete angles upwards and downwards with respect to the layers, as indicated in Figure 2.6, noting that the dotted lines are for visualisation purposes only. The superposition of upward (red) and downward (blue) travelling wave-fronts produce standing waveforms perpendicular to the plane; these are called the guided modes of the waveguide and *represent a transverse electromagnetic field distribution that is unchanging as it propagates along the waveguide*. Each guided mode is defined by a unique angle with respect to the interface normal, θ_m, which is greater than the critical angle, θ_c, for that interface, i.e. the condition for TIR.

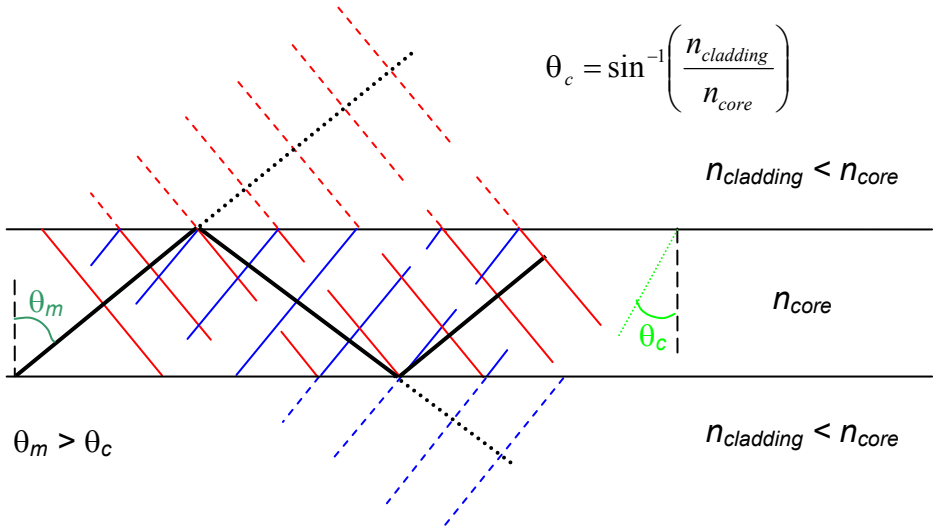

Figure 2.6: Upward and downward propagating plane waves in a waveguide.

2.4.2 Five layer double-clad waveguide

The concept of planar waveguides introduced above can be extended to account for more complex structures, and for which there are various numerical methods to calculate their modal properties [17]. An analytic solution for the guided modes of the double-clad

waveguide, illustrated in Figure 2.7, reported by Bonner *et. al.* [18] was obtained by choosing an appropriate form for the propagating electric field solutions in each layer of the structure. Solving the Helmholtz or "wave" equation and applying boundary conditions leads to an exact expression for the transverse electric field. A similar analysis, constructive for the following sections is developed in more detail here.

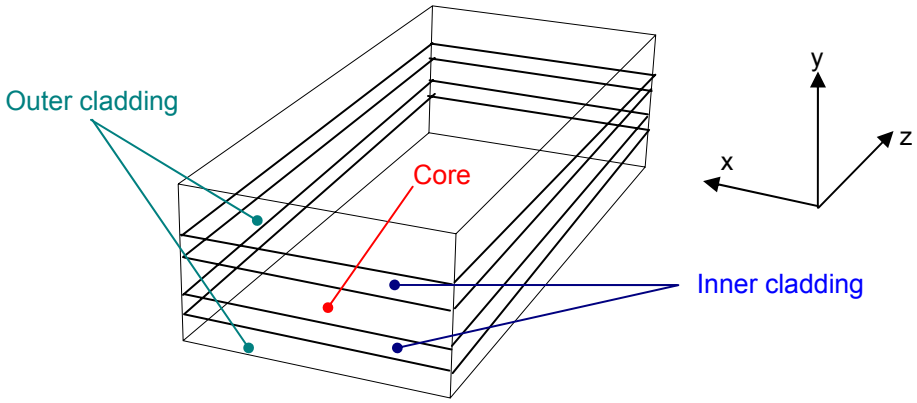

Figure 2.7: LMA double-clad planar waveguide

To start, first consider the waveguide configuration as defined in Figure 2.8, a five layer composite structure with a core layer surrounded by two lower refractive index materials. With $d_{1,2} = d_{3,4}$ and $n_{2,3} = n_{4,5}$ i.e. a symmetric structure, Figure 2.8 is representative of the LMA PW's investigated herein, however for generality the parameters describing each layer are kept independent. Mode solutions for the transverse electric (TE) field are derived, that is the field polarised in the plane, from which, by the duality of Maxwell's equations, the corresponding transverse magnetic (TM) field polarised perpendicular to the plane is found.

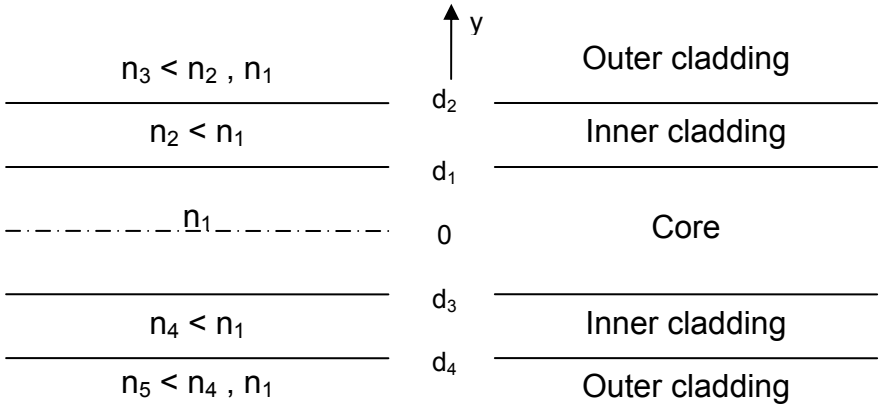

Figure 2.8: Parameters describing a double-clad planar waveguide. Note the core is divided in two, therefore $d_3 = -d_1$.

As discussed above, it can be assumed that in the core region the superposition of upward and downward propagating waves produce a transverse standing wave pattern described by an oscillatory solution. In contrast in the outer cladding layers, remembering that the guided modes are confined to the central layers, the electric field must decay as it propagates away from the interface, i.e. an evanescent field [17]. Finally, for the inner cladding layers, if the angle of propagation of the plane waves in the core is greater than the critical angle of the core-inner cladding interface, the same argument used for the outer cladding applies, i.e. exponential decay; otherwise an oscillatory solution is required. Therefore the general spatial form for the TE field amplitude may be written as,

$$E_x(y,z) = \begin{bmatrix} A_3 e^{-\alpha_3 y} & y \geq d_2 \\ A_2 e^{-\alpha_2 y} + A_2' e^{\alpha_2 y} & d_1 \leq y \leq d_2 \\ A_1 \cos\left(k_1 y + \psi^{TE}\right) & |y| \leq d_1 \\ A_4 e^{\alpha_4 y} + A_4' e^{-\alpha_4 y} & d_4 \leq y \leq d_3 \\ A_5 e^{\alpha_5 y} & y \leq d_4 \end{bmatrix} e^{-jk_z z} \quad \textbf{(2.41),}$$

where the A_i terms give the field amplitude in the ith layer, k_1 and α_i are the wavenumbers along the y-axis in the core and ith layer respectively, k_z is the wavenumber for the guided mode in the plane, and finally a phase term ψ^{TE} is introduced to account for a possible non-symmetric nature of the expected standing wave solutions. It should be highlighted that in the inner cladding layers, *i = 2 or 4*, the field solution is allowed to be either, oscillatory, for imaginary α_i, or evanescent, for real α_i.

Applying the Helmholtz equation, $\left(\nabla^2 + k_0^2 n_i^2\right)\underline{E} = 0$ to the electric field of equation (2.41) produces the dispersion relationships for the waveguide structure; thus the wavenumber in the ith layer is given by;

$$\alpha_i = k_0 \sqrt{(n_{eff}^2 - n_i^2)}$$
$$k_1 = k_0 \sqrt{(n_1^2 - n_{eff}^2)} \quad \textbf{(2.42)}$$

where $n_{eff} = k_z / k_0$, and k_0 is the free space wavenumber.

A direct consequence of the integral forms of Maxwell's equations is that across the interface of two dielectric media, the tangential electric and magnetic fields must be

continuous [13]. Therefore, to solve all the boundary conditions it is also necessary to determine the magnetic field in the plane. Using the time-harmonic Maxwell's curl equation, $\nabla \times \underline{E} = -j\omega\mu \underline{H}$, the general form for the tangential magnetic field is obtained,

$$H_z(y,z) = \frac{j}{\omega} \begin{bmatrix} \frac{-\alpha_3}{\mu_3} A_3 e^{-\alpha_3 y} & y \geq d_2 \\ \frac{-\alpha_2}{\mu_2}\left(A_2 e^{-\alpha_2 y} - A_2' e^{\alpha_2 y}\right) & d_1 \leq y \leq d_2 \\ \frac{-k_1}{\mu_1} A_1 \sin\left(k_1 y + \psi^{TE}\right) & |y| \leq d_1 \\ \frac{\alpha_4}{\mu_4}\left(A_4 e^{\alpha_4 y} - A_4' e^{-\alpha_4 y}\right) & d_4 \leq y \leq d_3 \\ \frac{\alpha_5}{\mu_5} A_5 e^{\alpha_5 y} & y \leq d_4 \end{bmatrix} e^{-jk_z z}$$

(2.43).

Notwithstanding the dielectric nature of the composite structure the magnetic permeability, μ_i, for each layer is kept independent; this is done for ease in determining the TM mode solutions later.

Equating the fields at the interfaces in equations (2.41) and (2.43) produces a set of eight linear equations from which it is possible to find each amplitude coefficient A_i, $i = 2\text{-}5$, in terms of A_1. Also eliminating the amplitude coefficient A_1 by dividing the boundary condition equations for the inner cladding and core interfaces, a phase delay is obtained that corresponds to the plane wave propagation through the upper and lower halves of the waveguide. Consequently the guidance condition is defined noting that for self consistency the phase delay must be a multiple of 2π. It should be noted that this combination of equations also gives the phase constant ψ^{TE}.

Following the above method the guidance condition, a transcendental equation which must be solved graphically or numerically to find the core wavenumber, k_1, is described by;

$$2k_1 d_1 - \phi_{upp}^{TE} - \phi_{lwr}^{TE} = p\pi \qquad p = 0, 1, \ldots$$

(2.44),

with the constant phase component of the TE oscillatory field in the core given by,

$$\psi^{TE} = \frac{\phi_{upp}^{TE} - \phi_{lwr}^{TE} - p\pi}{2}$$

(2.45).

The phase delay for plane waves propagating through the upper or lower half of the waveguide is,

$$\phi_{upp}^{TE} = \arctan\left(\frac{\mu_1\alpha_2}{\mu_2 k_1}\left(\frac{\mu_2\alpha_3 + \mu_3\alpha_2\tanh(\alpha_2(d_2 - d_1))}{\mu_3\alpha_2 + \mu_2\alpha_3\tanh(\alpha_2(d_2 - d_1))}\right)\right)$$

$$\phi_{lwr}^{TE} = \arctan\left(\frac{\mu_1\alpha_4}{\mu_4 k_1}\left(\frac{\mu_4\alpha_5 + \mu_5\alpha_4\tanh(\alpha_4(d_3 - d_4))}{\mu_5\alpha_4 + \mu_4\alpha_5\tanh(\alpha_4(d_3 - d_4))}\right)\right)$$

(2.46).

The parameter p denotes the guided mode number, where the TE_p mode has p nodes across its distribution.

Finally the transverse electric field amplitude is described by the equation,

$$E_x(y,z) = A_1^{TE}\begin{bmatrix} A_{upp}^{TE}e^{d_2(\alpha_2+\alpha_3)}\left(\frac{2\mu_3\alpha_2}{\mu_3\alpha_2 - \mu_2\alpha_3}\right)e^{-\alpha_3 y} & y \geq d_2 \\ A_{upp}^{TE}\left[\left(\frac{\mu_3\alpha_2 + \mu_2\alpha_3}{\mu_3\alpha_2 - \mu_2\alpha_3}\right)e^{2\alpha_2 d_2 - \alpha_2 y} + e^{\alpha_2 y}\right] & d_1 \leq y \leq d_2 \\ \cos(k_1 y + \psi^{TE}) & |y| \leq d_1 \\ A_{lwr}^{TE}\left[\left(\frac{\mu_5\alpha_4 + \mu_4\alpha_5}{\mu_5\alpha_4 - \mu_4\alpha_5}\right)e^{-2\alpha_4 d_4 + \alpha_4 y} + e^{-\alpha_4 y}\right] & d_4 \leq y \leq d_3 \\ A_{lwr}^{TE}e^{-d_4(\alpha_4+\alpha_5)}\left(\frac{2\mu_5\alpha_4}{\mu_5\alpha_4 - \mu_4\alpha_5}\right)e^{\alpha_5 y} & y \leq d_4 \end{bmatrix} e^{-jk_z z}$$

(2.47),

where the coefficients in the upper and lower cladding layers are,

$$A_{upp}^{TE} = \frac{\cos(k_1 d_1 + \psi^{TE})e^{-\alpha_2 d_1}}{\left(\left(\frac{\mu_3\alpha_2 + \mu_2\alpha_3}{\mu_3\alpha_2 - \mu_2\alpha_3}\right)e^{2\alpha_2(d_2 - d_1)} + 1\right)} \qquad A_{lwr}^{TE} = \frac{\cos(k_1 d_3 + \psi^{TE})e^{\alpha_4 d_3}}{\left(\left(\frac{\mu_5\alpha_4 + \mu_4\alpha_5}{\mu_5\alpha_4 - \mu_4\alpha_5}\right)e^{2\alpha_4(d_3 - d_4)} + 1\right)}$$

(2.48).

Having determined the TE field, it is a simple matter of making the appropriate substitutions according to the duality of Maxwell's equations to obtain the transverse

magnetic (TM) field solution, namely; $\underline{E} \rightarrow -\underline{H}$, $\underline{H} \rightarrow \underline{E}$, $\mu \rightarrow \varepsilon$, $\varepsilon \rightarrow \mu$. Therefore the magnetic field amplitude is described by,

$$H_x(y,z) = -A_1^{TM} \begin{bmatrix} A_{upp}^{TM} e^{d_2(\alpha_2+\alpha_3)} \left(\frac{2\varepsilon_3\alpha_2}{\varepsilon_3\alpha_2 - \varepsilon_2\alpha_3} \right) e^{-\alpha_3 y} & y \geq d_2 \\ A_{upp}^{TM} \left[\left(\frac{\varepsilon_3\alpha_2 + \varepsilon_2\alpha_3}{\varepsilon_3\alpha_2 - \varepsilon_2\alpha_3} \right) e^{2\alpha_2 d_2 - \alpha_2 y} + e^{\alpha_2 y} \right] & d_1 \leq y \leq d_2 \\ \cos\left(k_1 y + \psi^{TM}\right) & |y| \leq d_1 \\ A_{lwr}^{TM} \left[\left(\frac{\varepsilon_5\alpha_4 + \varepsilon_4\alpha_5}{\varepsilon_5\alpha_4 - \varepsilon_4\alpha_5} \right) e^{-2\alpha_4 d_4 + \alpha_4 y} + e^{-\alpha_4 y} \right] & d_4 \leq y \leq d_3 \\ A_{lwr}^{TM} e^{-d_4(\alpha_4+\alpha_5)} \left(\frac{2\varepsilon_5\alpha_4}{\varepsilon_5\alpha_4 - \varepsilon_4\alpha_5} \right) e^{\alpha_5 y} & y \leq d_4 \end{bmatrix} e^{-jk_z z}$$

(2.49),

where the coefficients in the upper and lower cladding layers are,

$$A_{upp}^{TM} = \frac{\cos\left(k_1 d_1 + \psi^{TM}\right) e^{-\alpha_2 d_1}}{\left(\left(\frac{\varepsilon_3\alpha_2 + \varepsilon_2\alpha_3}{\varepsilon_3\alpha_2 - \varepsilon_2\alpha_3} \right) e^{2\alpha_2(d_2 - d_1)} + 1 \right)} \qquad A_{lwr}^{TM} = \frac{\cos\left(k_1 d_3 + \psi^{TM}\right) e^{\alpha_4 d_3}}{\left(\left(\frac{\varepsilon_5\alpha_4 + \varepsilon_4\alpha_5}{\varepsilon_5\alpha_4 - \varepsilon_4\alpha_5} \right) e^{2\alpha_4(d_3 - d_4)} + 1 \right)}$$

(2.50).

The equivalent TM guidance condition is;

$$2k_1 d_1 - \phi_{upp}^{TM} - \phi_{lwr}^{TM} = p\pi \qquad p = 0, 1, ...$$

(2.51),

with the corresponding constant phase component,

$$\psi^{TM} = \frac{\phi_{upp}^{TM} - \phi_{lwr}^{TM} - p\pi}{2}$$

(2.52)

and the phase delay for the TM polarised plane waves in the upper or lower half of the waveguide is,

$$\phi_{upp}^{TM} = \arctan\left(\frac{\varepsilon_1\alpha_2}{\varepsilon_2 k_1} \left(\frac{\varepsilon_2\alpha_3 + \varepsilon_3\alpha_2 \tanh\left(\alpha_2(d_2 - d_1)\right)}{\varepsilon_3\alpha_2 + \varepsilon_2\alpha_3 \tanh\left(\alpha_2(d_2 - d_1)\right)} \right) \right)$$

$$\phi_{lwr}^{TM} = \arctan\left(\frac{\varepsilon_1\alpha_4}{\varepsilon_4 k_1} \left(\frac{\varepsilon_4\alpha_5 + \varepsilon_5\alpha_4 \tanh\left(\alpha_4(d_3 - d_4)\right)}{\varepsilon_5\alpha_4 + \varepsilon_4\alpha_5 \tanh\left(\alpha_4(d_3 - d_4)\right)} \right) \right)$$

(2.53).

Due to the similarity in the resulting mode solutions for the TE and TM fields, only the TE mode profiles are considered throughout the rest of this chapter.

2.4.3 Rare-earth-doped direct-bonded planar waveguides

2.4.3.1 Refractive index profile

The refractive index of the rare-earth-doped core of the LMA waveguides depends upon the doping concentration and the rare-earth ion itself. In all cases considered the core refractive index is increased with respect to the un-doped YAG inner cladding layers, thus obtaining a weak symmetric waveguide, which is in turn clad with sapphire, Figure 2.9, forming a strong or highly multimode waveguide. The index change of the doped YAG has been demonstrated to be linear with the doping concentration [19] for rare earth ions having an ionic radius up to 1.07 Å. A summary of the index change per doping percentage for the rare earth ions investigated is detailed in Table 2-1.

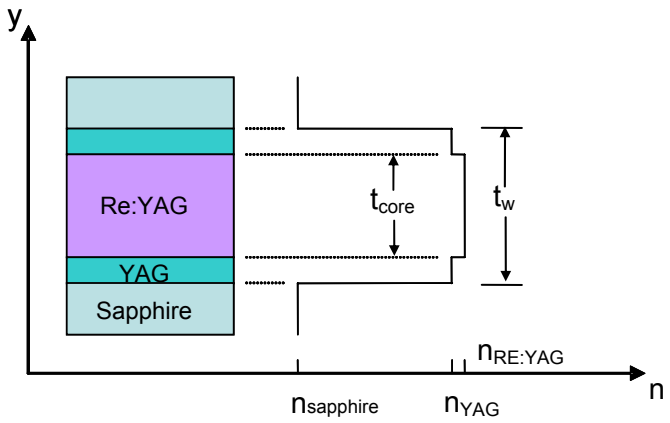

Figure 2.9: Cross sectional schematic of the refractive index profile for a RE:YAG/YAG/Sapphire LMA double-clad planar waveguide.

Rare earth ion	Refractive index change $x10^{-4}$ per at.%
Nd^{3+}	4 [18]
Er^{3+}	2.2 [19]
Tm^{3+}	1.9 [19]
Yb^{3+}	1.5 [20]

Table 2-1: Refractive index increase for YAG per rare earth doped concentration

In a classical double-clad fibre, the core is itself a single-mode waveguide isolated from the outer multi-mode cladding waveguide [21]. Whereas in the waveguides considered here this does not have to be the case, rather for the mode selection properties to be effective the next higher order core mode need only be weakly confined, with its field distribution extending well into the inner cladding, if not out to the outer cladding. This will be discussed in more detail, however first it is beneficial to demonstrate the way the core refractive index changes the modal properties of the LMA planar waveguide.

Using equations (2.44)-(2.48) the TE_p mode profile can be obtained corresponding to the physical characteristics of the waveguide structure of interest. For illustrative purposes imagine a nominal structure, representative of the LMA waveguides investigated herein, with physical properties as defined in Table 2-2, guiding light with a free space wavelength of 1μm, and for which a core-inner cladding index difference, Δn can be defined.

	Layer thickness (μm)	Refractive index
Core	20	1.816+Δn
Inner cladding	5	1.816
Outer cladding	>5	1.756

Table 2-2: Nominal symmetric double-clad waveguide characteristics.

It is then observed that by increasing the refractive index step between the core and inner cladding the calculated modes shown in Figure 2.10, are progressively more confined to the core. The four index steps, $\Delta n = 0$, 10^{-4}, 10^{-3}, and 10^{-2}, illustrated in Figure 2.10 transform the core layer from supporting no modes, i.e. a large 30μm three layer multimode guide, to 1, 3 and 8 modes respectively. Thus for the nominal example given here the limiting index step, for which it may still be considered to be a LMA double-clad waveguide with a single mode core, is between 10^{-4} and 10^{-3}. After which the possibility that the TE_1 mode could exceed threshold of a laser cavity increases with its percentage overlap with the doped core. Considering the normalised profiles of Figure 2.10 it is obvious that the lower order modes corresponding to an index difference between $\Delta n = 10^{-3} - 10^{-2}$ have a strong overlap with the core region, indicated by the two vertical dotted lines, therefore it would be expected that in such cases a waveguide laser would operate multimode. Reviewing Table 2-1, it is evident that for typical rare-earth doping

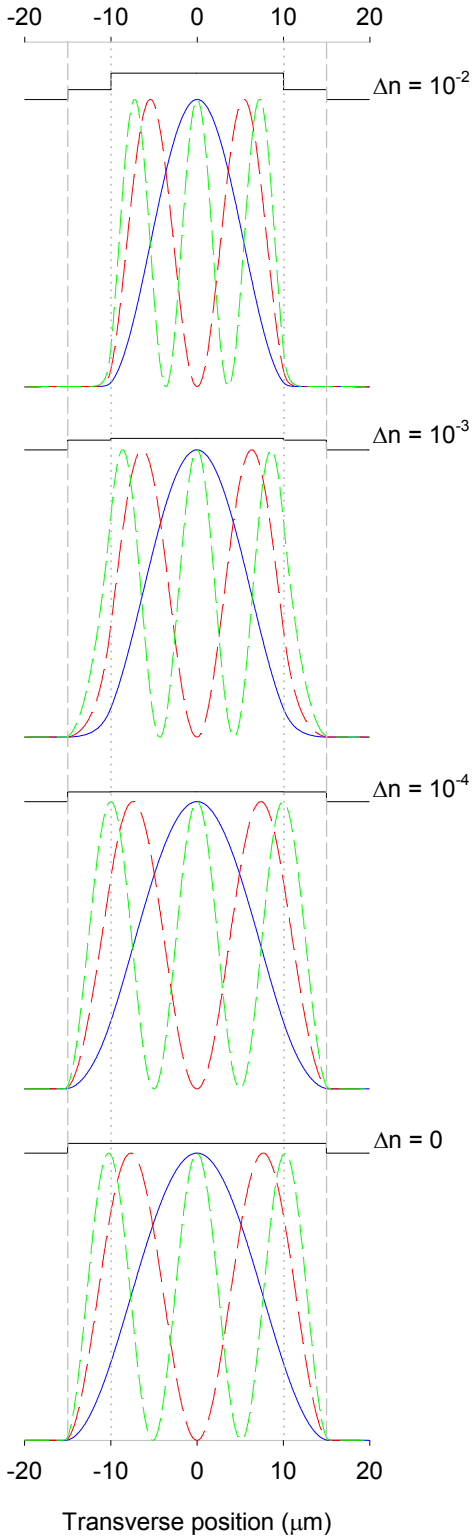

Figure 2.10: Normalised TE_0 (——), TE_1 (— —), and TE_2 (— —) profiles for the waveguide prescribed in Table 2-2, with increasing refractive index difference, Δn (——). Note: refractive index profile is to scale, with Δn magnified by 10.

concentrations used to achieve good laser performance, for example ~1% Nd, ~10% Yb, Tm, and ~50% Er, the index step between the central layers is of the order of $\Delta n = 10^{-3}$ -10^{-2}.

Therefore care must be taken with the waveguide design of rare-earth-doped 5-layer structures, including attention to the laser wavelength unique to the active ion, by ensuring that the higher order core modes are not well confined to the doped region. One other important reason to use the LMA waveguide in the planar geometry is the associated higher effective absorption coefficient, as discussed in the following section.

2.4.4 Large mode area planar waveguide absorption efficiency

A simple assumption can be made that the absorption coefficient for the pump radiation delivered to a waveguide will be reduced by a factor, η_{po}, equal to the ratio of the doped to un-doped areas of the central layers (doping ratio=t_{core}/t_w see Figure 2.9), compared to a uniformly doped material. This assumption does not account for the different overlap factors with the central doped region of the various propagation modes supported by the waveguide.

With this in mind a BPM[x] model was used to compare the absorption efficiency of the nominal structure defined in Table 2-2 to a similar structure with uniform doping throughout the YAG layers. The results, illustrated in Figure 2.11, show that the absorption coefficient is reduced to η_{po}=0.68 whereas the simple assumption above leads to a value of 2/3. The small difference in these figures is due to the larger relative absorption coefficient of lower order modes, which approach that of the uniformly doped material, compared to that of higher order modes, as illustrated by the lower pair of lines in Figure 2.11.

This modelling is based on a perfectly aligned diode, which leads solely to the excitation of even modes within the YAG layers. However, the same modelling for a diode offset vertically by 5µm, so that the odd modes are also excited, gives nearly identical results.

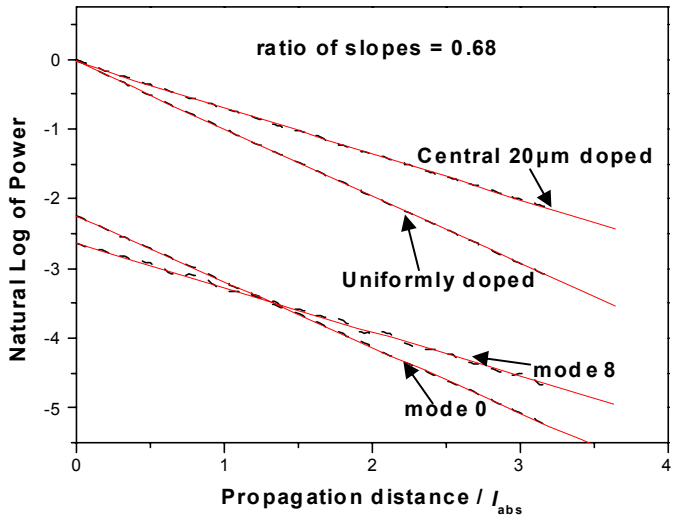

Figure 2.11: Pump power against distance in units of bulk material absorption length (l_{abs}). Dashed lines are the calculated power and the solid lines are linear fits. The upper two curves show the absorption in uniformly doped and centrally doped waveguides. The lower two curves show the absorption of the lowest order mode and a higher order mode in the centrally doped waveguide.

[x] Beam propagation method (BPM) – is a numerical analysis technique to determine the evolution of an electromagnetic field as it propagates through some predefined system. The method starts with an initial field and then calculates successive distributions at incremental planes along the direction of propagation, by applying the wave equation and local boundary conditions. Each successive field is the source for the next incremental step until the last plane is reached and the final field distribution determined.

2.4.5 Gain mode selection in large mode area planar waveguide lasers

For a uniformly side-pumped LMA PW, it can be assumed that *r(x,y,z) = d(x,y,z)*, a consequence of exciting many higher order modes, therefore the second term of equation (2.7) simply disappears leaving no dependence on the doping distribution, that is,

$$\Delta N(x,y,z) = \frac{(L + \ln(R_l^{oc}))d(x,y,z)}{2l\sigma(1 + S\phi(x,y,z))I_r} \quad \textbf{(2.54).}$$

For practical double-clad devices, as illustrated in section 2.4.3, doping the core normally induces a finite index change; therefore, combining the equations defined in section 2.2.1 with equation (2.54), it is possible to investigate the mode selection properties for real LMA PW lasers.

In a CW laser oscillator the gain is clamped at the level of the cavity loss, as stated by equation (2.4). Therefore the gain for the p^{th} mode, can be determined relative to the TE_0 lasing mode, $\phi(x,y,z)$, including saturation effects by the mode already oscillating, by rearranging equation (2.8) and using equation (2.54) for $\Delta N(x,y,z)$, such that,

$$G_p^{rel} = \frac{G_p}{L - \ln(R_l^{oc})} \quad \textbf{(2.55),}$$

where L represents the loss exponent for the cavity. To demonstrate that the TE_0 mode is the first waveguide mode to reach threshold in the nominal LMA PW laser investigated, irrespective of the doping ratio and index step, equation (2.55) is solved with the lasing intensity set to zero, the thickness for the central layers, $t_w = 30\mu m$ (see Figure 2.9), and a free space wavelength of $1\mu m$. Figure 2.12(a) illustrates the results using mode profiles obtained from the solutions of equations (2.44)-(2.47), at various doping ratios and accounting for the refractive index steps indicated. Figure 2.12(b) then represents the relative gain for the TE_1 and TE_2 modes at three saturating power levels with the TE_0 mode as the oscillating field.

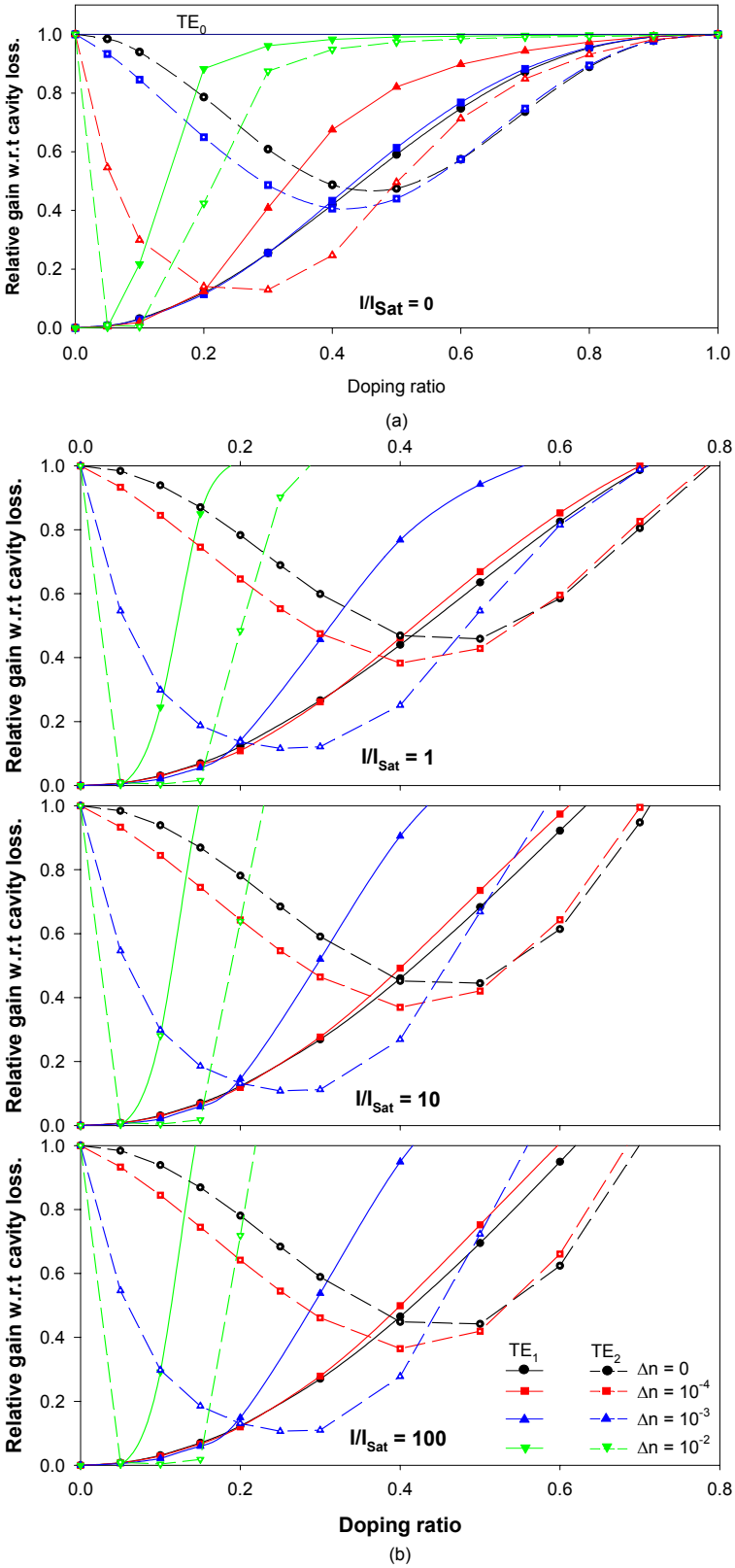

Figure 2.12: Relative gain for the TE_1 and TE_2 modes as a function of doping ratio. Corresponding to (a) threshold I=0, and (b) the saturation levels I/I_{sat} = 1, 10, 100, with refractive index steps, $\Delta n = 0, 10^{-4}, 10^{-3}$, and 10^{-2}, and an outer cladding spacing of 30 μm.

It should be noted that the TE_1 mode is in general the second mode to reach threshold and corresponds to the second highest overlap with the doped core region as discussed below. As suggested in section 2.4.3, it can be seen in Figure 2.12 that for higher order modes having a significant overlap with the doped region, as found for a refractive index step of $\Delta n = 10^{-2}$ and the nominal structure of Table 2-2, i.e. a doping ratio of ~0.67, the relative gain is well above unity for all saturation levels considered. In fact for each of the index steps considered, the points where $G_1^{rel} = 1$ correspond to the core waveguide supporting only two modes, the peaks of the TE_1 profile falling just within the doped region. This is illustrated for a highly saturated condition, $I/I_{sat}=100$, in Figure 2.13 for the cases $\Delta n = 10^{-3}$ and 10^{-2}.

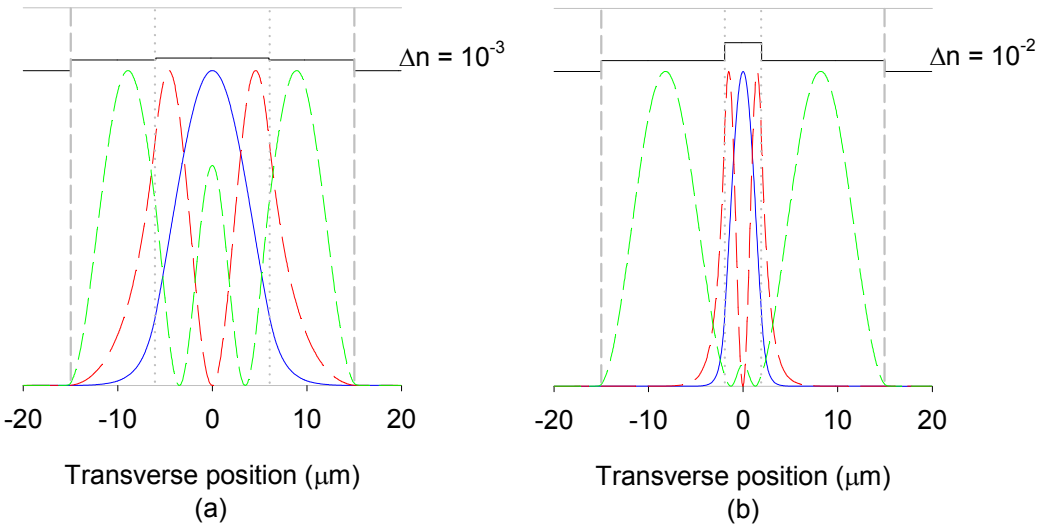

Figure 2.13: Normalised TE_0 (———), TE_1 (— —), and TE_2 (— — —) mode profiles when $G_1^{rel} = 1$ for a double-clad waveguide with t_w=30μm (— — —) and a core index step (———) of (a) $\Delta n = 10^{-3}$ with a doping ratio ~ 0.4, and (b) $\Delta n = 10^{-2}$ with a doping ratio ~ 0.13

2.4.6 Index profile limitations for mode selection

As illustrated above, including a refractive index profile associated with a non-uniform doping distribution modifies the spatial distribution of the laser field which in turn affects the mode selection characteristics. In the case of the double-clad waveguide with no core index step, i.e. $\Delta n = 0$, a limit for the doped layer thickness is found that is ~ 60% of the outer cladding spacing. This corresponds to an overlap of the TE_1 mode with the doped region equal to 70%. Thus for a high numerical aperture waveguide with non-uniform

doping distribution, the mode selection is dependent upon the laser field distribution and the overlap of the higher order modes with the saturated doped region. Specifically, it is a purely gain selection process, preferentially allowing one mode to exceed threshold over another; in the cases treated above, the fundamental with respect to higher order modes.

For the double-clad waveguide example, when an index step associated with the doping distribution is sufficient to support guided modes isolated from the outer cladding, as illustrated for the two mode case with TE_0 and TE_1 in Figure 2.13(b), the relative confinement for each of the higher order modes within the doped region is dependent upon the induced waveguide properties. Thus this process is a result of index mode selection and is the basis for the cladding-pumped fibre [21]. For the slab waveguide it is empirically found that the point at which the confinement factor is sufficient for the TE_1 mode to exceed threshold is ~64%. Where the confinement factor is defined by [14],

$$\Gamma_p = \frac{\int_{-t_{core}/2}^{t_{core}/2} |\phi(y)|^2 dy}{\int_{-\infty}^{\infty} |\phi(y)|^2 dy} \qquad \textbf{(2.56),}$$

$\phi(y)$ being the amplitude spatial field, i.e. a guided mode such as TE_1, and t_{core} is the doped core thickness. Following the same assumptions listed in the previous section for cavity loss and oscillating field, this empirical confinement factor corresponds to a limit for the core layer thickness related to the numerical aperture by,

$$t_{\lim} \approx \frac{3\lambda_0}{4NA} \qquad \textbf{(2.57),}$$

where NA is the numerical aperture of the core waveguide, i.e. $NA = \sqrt{n_{core}^2 - n_{cladding}^2}$.

Equation (2.57) can be used as a rule of thumb for an isolated slab waveguide giving the maximum core thickness allowed for a specific index difference between the core and surrounding cladding, whilst maintaining good mode selection properties.

However, due to the fact that for a planar device the pump radiation often needs to be absorbed in a reasonable distance, the doping ratio must be kept as large as possible (see

section 2.4.4). Therefore a balance must be found between the limit imposed on the core thickness, through equation (2.57), and the confining effects for the guided modes when the outer cladding layers are brought into close proximity with the core, as illustrated in Figure 2.13(a) and typical of the LMA PW. The results of an empirical study to determine the maximum doping ratio as a function of the waveguide aperture, i.e. t_w in Figure 2.9, where the relative gain for the TE_1 mode reaches unity, is shown in Figure 2.14. As illustrated, the maximum doping ratio reduces dramatically for increased waveguide aperture and index step, which is important for power scaling opportunities that require larger waveguides to achieve reasonable launch efficiencies. Considering Figure 2.14 it is conceivable that the LMA PW is a viable geometry for power scaling, particularly if the index step, Δn, about the core is kept below 10^{-4}.

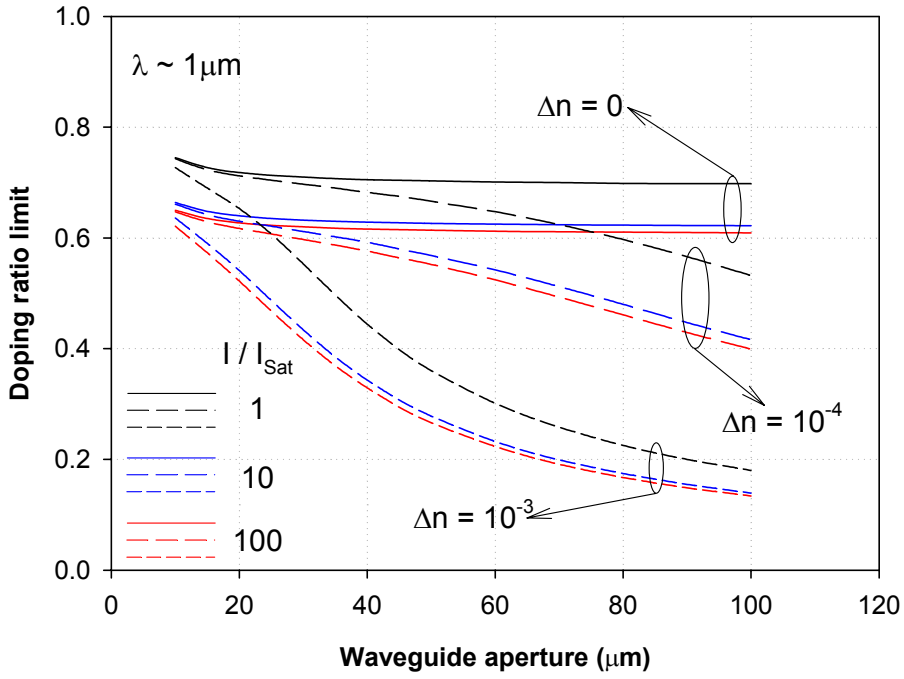

Figure 2.14: Doping ratio limit as a function of the separation between outer cladding layers, t_w.

2.5 References

[1] W. P. Risk, "Modeling of Longitudinally Pumped Solid-State Lasers Exhibiting Reabsorption Losses," *Journal of the Optical Society of America B-Optical Physics*, vol. 5, pp. 1412-1423, 1988.

[2] R. J. Beach, "CW theory of quasi-three level end-pumped laser oscillators," *Optics Communications*, vol. 123, pp. 385-393, 1996.

[3] W. B. Joyce and R. W. Dixon, "Thermal resistance of heterostructure lasers," *Journal of Applied Physics*, vol. 46, pp. 855 - 862, 1974.

[4] J. M. Eggleston, T. J. Kane, K. Kuhn, J. Unternahrer, and R. L. Byer, "The Slab Geometry Laser - Part 1. Theory," *IEEE Journal of Quantum Electronics*, vol. 20, pp. 289-301, 1984.

[5] K. Kubodera and K. Otsuka, "Single-transverse-mode $LiNdP_4O_{12}$ slab waveguide laser," *Journal of Applied Physics*, vol. 50, pp. 653-659, 1979.

[6] T. Y. Fan and R. L. Byer, "Modeling and CW Operation of a Quasi-3-Level 946nm Nd-YAG Laser," *IEEE Journal of Quantum Electronics*, vol. 23, pp. 605-612, 1987.

[7] M. J. F. Digonnet and C. J. Gaeta, "Theoretical-Analysis of Optical Fiber Laser-Amplifiers and Oscillators," *Applied Optics*, vol. 24, pp. 333-342, 1985.

[8] M. P. Petrov, R. V. Kiyan, E. A. Kuzin, E. A. Rogacheva, and V. V. Spirin, "Gain Saturation in 3-Level and 4-Level Fiber Amplifiers," *Optics Communications*, vol. 109, pp. 499-506, 1994.

[9] J. Nilsson, J. D. Minelly, R. Paschotta, A. C. Tropper, and D. C. Hanna, "Ring-doped cladding-pumped single-mode three-level fiber laser," *Optics Letters*, vol. 23, pp. 355-357, 1998.

[10] G. L. Bourdet, "Theoretical investigation of quasi-three-level longitudinally pumped continuous wave lasers," *Applied Optics*, vol. 39, pp. 966-971, 2000.

[11] W. A. Clarkson, "Thermal effects and their mitigation in end-pumped solid-state lasers," *Journal of Physics D-Applied Physics*, vol. 34, pp. 2381-2395, 2001.

[12] W. Koechner, *Solid State Laser Engineering - Chapter 7*, vol. 1, 4th ed. Berlin Heidelberg: Springer Verlag, 1999.

[13] D. Lee, *Electromagnetic Principles of Integrated Optics - Chapter 2*, 3rd ed. New York: John Wiley and Sons, 1986.

[14] B. E. A. Saleh and M. C. Teich, *Fundamentals of Photonics*, 1st ed. New York: Wiley, 1991.

[15] A. W. Snyder and J. D. Love, *Optical Waveguide Theory*. New York: Chapman and Hall, 1983.

[16] A. Yariv, *Quantum Electronics*, 3rd ed. New York: John Wiley, 1989.

[17] D. Lee, *Electromagnetic Principles of Integrated Optics - Chapter 4*, 3rd ed. New York: John Wiley and Sons, 1986.

[18] C. L. Bonner, T. Bhutta, D. P. Shepherd, and A. C. Tropper, "Double-clad structures and proximity coupling for diode-bar- pumped planar waveguide lasers," *IEEE Journal of Quantum Electronics*, vol. 36, pp. 236-242, 2000.

[19] S. F. Akhmetov, G. L. Akhmetova, G. A. Gazizova, V. S. Kovalenko, and T. F. Mirenkova, "Rare Earth Metal Aluminium Garnets," *Russian Journal of Inorganic Chemistry*, vol. 22, pp. 1613-1615, 1977.

[20] F. D. Patel, E. C. Honea, J. Speth, S. A. Payne, R. Hutcheson, and R. Equall, "Laser demonstration of $Yb_3Al_5O_{12}$ (YbAG) and materials properties of highly doped Yb:YAG," *IEEE Journal of Quantum Electronics*, vol. 37, pp. 135-144, 2001.

[21] L. Zenteno, "High-Power Double-Clad Fiber Lasers," *Journal of Lightwave Technology*, vol. 11, pp. 1435-1446, 1993.

Chapter 3

END - PUMPED CONTINUOUS WAVE WAVEGUIDE LASERS

3.1 Introduction

Solid-state lasers have gathered increased popularity as compact, efficient, high-power sources for a variety of applications. Efficient laser operation is dependent upon the properties of the active host, the pump source, and oscillator geometry. Typically these require; the use of efficient high-power diode pump sources, a pump power well over the lasing threshold requirement, efficient waste heat removal from the lasing region, good overlap between the pump and signal beams, and relatively low resonator losses compared to the output coupling. Many pump conditioning schemes and resonator geometries have been reported that satisfy some or all of these requirements, for example, see [1] and references therein. In this chapter it is demonstrated that the planar waveguide geometry, especially in the configuration where the pump and laser fields are co-linear, i.e. longitudinal or end-pumping, offers many interesting properties that could be used to fulfil the above requirements.

Optical confinement offered by a planar waveguide leads to a high pumping intensity and lowering of the laser threshold pump power, particularly in the end-pumped geometry, making operation well above lasing threshold achievable for moderate powers. Furthermore, as the lasing mode is also guided and, in the case of the double-clad structures described here, fully contains the gain region, the spatial overlap is optimised for efficient output. The asymmetric geometry of the planar guide is also well matched to that of high-power diode pump sources, simplifying the required coupling optics. In addition, the double-clad YAG-sapphire composite has a thermal conductivity that is approximately that of sapphire; almost three times that of the YAG, which accounts for only 30μm of the overall structure thickness. Thus the heat source can be position closed to the heat sink by using thin outer cladding layers, offering significant benefits when considering the peak temperature rise and stress fracture limits within the lasing medium. Finally, one further advantage of the planar waveguide and small temperature rise is that

the optical guidance dominates the thermal lensing in the guided axis [2]. Therefore the output beam quality is defined by the waveguide structure in the guided axis and the thermally induced lens in the unguided axis. The latter effect is quite weak due to the efficient heat extraction from the active core and the use of a relatively "top-hat" pump beam that matches the fundamental laser mode [3].

Detailed in the rest of this chapter are the performance results for two diode-end-pumped LMA PW lasers. However, first a brief review of the pump beam quality requirements is made. The subsequent section, is devoted to a Nd:YAG LMA PW laser, its performance operating on four laser transitions is described and compared to results obtained from the model developed in chapter 2. The final section reports the performance of the first reported Er:YAG double-clad waveguide laser.

3.2 Diode coupling

Optical excitation of an active material typically requires the pump distribution be conditioned by intermediary optics whilst transferring the radiation to the region of interest. Similarly in-plane pumping of a waveguide, the pump radiation must be efficiently launched or coupled into it. Therefore the beam quality of the incident radiation, perpendicular to the plane, with wavelength, λ_p, should be less than a limit imposed by the waveguide aperture, t_w, and numerical aperture, NA, namely [4],

$$M_y^2 < \frac{NA \cdot t_w}{\lambda_p} \qquad \textbf{(3.1).}$$

Substituting in parameters which describe the waveguides investigated in this chapter, $NA = 0.47$ and $t_w = 30\mu m$, for a pump wavelength of $\lambda_p \sim 0.8\mu m$, gives a limiting beam quality of $M_y^2 < 17.5$.

The end-pumped configurations reported in this and the following chapter typically use a high-brightness diode pump source which has a beam quality, at least in one axis, less that the limit defined by equation (3.1). The set-up, as illustrated in Figure 3-1, consists of a cylindrical lens focussing the slow or "poor" beam quality axis before a spherical short focal length lens forming a beam reducing telescope in this axis. Conversely the pump beam in the other axis is simply focussed to a beam waist which is positioned at the entrance aperture of the waveguide. This coupling scheme efficiently launches the pump

radiation into the planar waveguide, whilst the in-plane beam quality is conditioned such that its Rayleigh range is of the order of an absorption length.

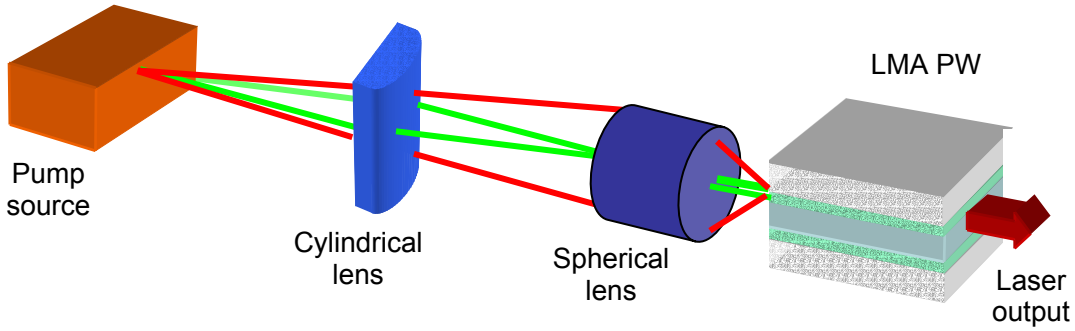

Figure 3-1: Schematic for the end-pumping configuration.

3.3 Nd:YAG large mode area planar waveguide laser

3.3.1 Introduction

The Nd:YAG double-clad waveguide has been reported previously in a side-pumped configuration [5, 6]. In this section an end-pumped double-clad planar waveguide laser is demonstrated based on a YAG/sapphire bonded structure that can readily fulfil the aforementioned requirements for compact and efficient, multi-Watt, diffraction-limited laser sources. The inherent waveguide properties are especially advantageous for weak and/or quasi-three-level transitions, which normally have relatively high laser thresholds and can be sensitive to temperature excursions. Described here is the laser performance for four transitions of Nd:YAG, indicated in Figure 3-2, including operation of the weak 1.83µm and quasi-three-level 946nm transitions.

3.3.2 Experimental set-up

The structure, illustrated in Figure 3-3, has a 30µm-deep YAG region, of which the central 20µm is doped with 1at.% Nd, it is 5mm wide by 10mm long waveguide and was fabricated by Onyx Optics via the direct bonding technique. Applying the analysis of Findlay and Clay [7] to determine the cavity losses of a 4-level laser system, a propagation loss of <0.2dB/cm at 1.064µm was found, reflecting previously reported values for similar waveguide structures [4, 8]. It was noted that this analysis worked well for small cavity output coupling (T_l^{oc}<30%), but was found to result in an increasing loss when extending

to higher T_l^{oc}. This was attributed to upconversion due to the high intensity pumping used when characterising the structure with a Ti:sapphire laser. Increasing the output coupling beyond 30% meant that the laser threshold was approaching half of the pump saturation intensity of 17kWcm^{-2} and twice that determined as a level beyond which Auger processes should be considered [9].

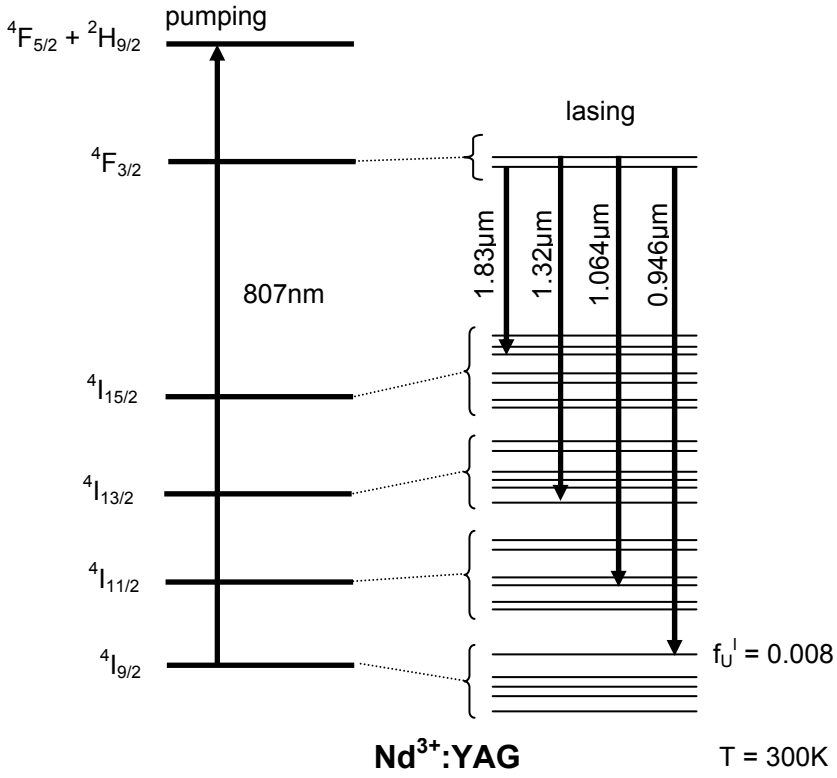

Figure 3-2: Energy level diagram for Nd:YAG, illustrating the Stark level splittings and the fractional population (f_U^l) of the terminal laser level for the 946nm quasi-three-level transition. The arrows indicate the Stark levels coupled by the laser radiation.

The pump source, from unique m.o.d.e AG[xi], consists of two broad-stripe single emitters, micro-beam-shaped and polarisation combined to form a single, approximately square-shaped beam of M^2 ~17 in both axes. Delivering almost 10W at 807nm, the output was collimated and allowed to propagate in free space. Noting the limit imposed by equation (3.1) this pump source, which had the beam quality of the broad-stripe diodes

[xi] unique m.o.d.e AG, D-07745 Jena, Germany.

improved in one axis at the expense of the other, was efficiently launched into LMA PW. At the same time it could be focussed to a smaller in-plane beam waist than in earlier experiments, which used a single 4W 200μm wide broad-stripe diode [10]. In this fashion the pump beam could be conditioned in the unguided axes such that its Rayleigh range was equivalent to the absorption length within the waveguide. The improvement of the pump beam size, with respect to earlier experiments with the single 200μm-wide pump diode, in the unguided plane allowed a better overlap between pump and laser fields, leading to significantly improved extraction efficiency and beam quality.

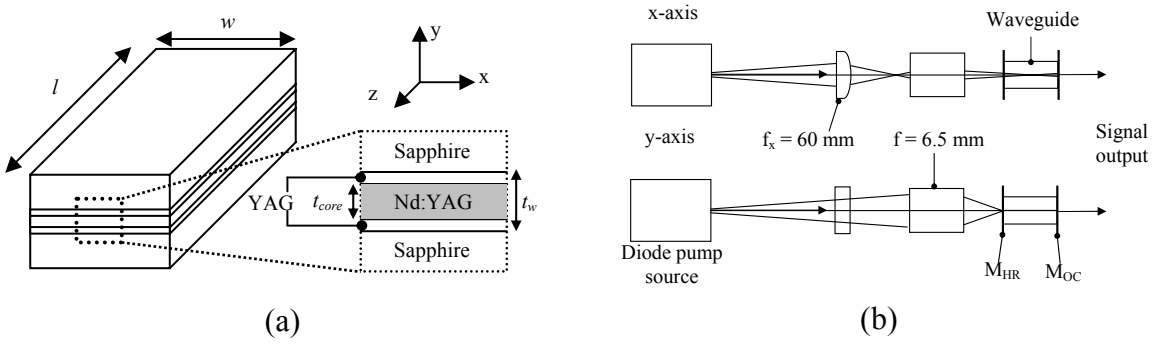

Figure 3-3: (a) Nd:YAG LMA double-clad planar waveguide (b) End-pumping set-up schematic.

A schematic of the experimental set-up is illustrated in Figure 3-3(b). The diode pump module was mounted on an air-cooled heatsink, with the diode temperatures maintained by internal thermo-electric peltier devices controlled via a separate external power supply and driver. The two diodes connected in series required 26W of electrical power to produce an optical output of 9.7W of pump power centred about 807nm. The optical coupling scheme consisted of an anti-reflection (AR) coated plano-convex cylindrical lens of focal length, f_x = 60mm, focusing in the x-axis, followed by a spherical low f-number[xii] diode-collimating lens module[xiii] with focal length f = 6.5mm and NA = 0.5. The lenses were arranged such that the in-plane x-axis beam waist was $\omega_{px0} = 100 \pm 3\mu m$ positioned ~5mm inside the waveguide structure with respect to the input face (leading to a calculated average pump radius over the crystal length of $\omega_{px} = 128\mu m$), and the y-axis

[xii] f- number = f /ϕ, where f = focal length of a lens, and ϕ the working diameter.

[xiii] Melles Griot – Part Number GLC 001.

beam waist was $\omega_{py} = 15 \pm 1\mu m$. The pump beam quality was observed to degrade using this coupling scheme and was measured to be $M_x^2 = 29$ and $M_y^2 = 18$ after the spherical focussing lens. An incident pump power of 8.6W was delivered to the pump-input mirror.

The waveguide was mounted on a precision 6-axis translation stage allowing easy positioning with respect to the focus of the pump beam. It should be noted that the waveguide was simply fixed to a copper block with a thermally conductive adhesive and not actively cooled. Thin lightweight mirrors (M_{HR}, M_{OC}), coated on one face only, were attached to the waveguide end faces via the surface tension of a thin layer of fluorinated liquid, Fluorinert[xiv], thus forming a quasi-monolithic flat-flat laser cavity of 10mm length. This procedure, although flexible for optimising the cavity output coupling, was not suitable for long-term high-power operation. Two problems were encountered, first achieving a good contact between mirror and waveguide structure over the excited region, and secondly the stability of the mirror position with increasing oscillating power. Both of these problems could be overcome by directly coating the end-faces for an optimised device.

3.3.3 Laser performance

Each specific laser transition was selected by tailoring the mirror reflectance for the desired output coupling whilst discriminating against the others, ensuring that its threshold was lowest. A summary of the laser performance obtained is shown in Table 3-1 and Figure 3-4. It should be noted that the waveguide length was not fully optimised for longitudinal pumping and slightly better output performance would be expected for a shorter crystal length, especially for the 946nm quasi-three-level $^4F_{3/2} \rightarrow {}^4I_{9/2}$ transition, which has moderate re-absorption loss.

An Ando spectrum analyser[xv] was used to measure the three shorter wavelengths, while 1.8μm operation was observed using an extended range InGaAs pin photodiode and a Bentham monochromator[xvi]. The two observed wavelengths for the $^4F_{3/2} \rightarrow {}^4I_{13/2}$ line were

---

[xiv] Fluorinert™: manufacturer 3M™, St Paul, MN 55144-1000 USA.

[xv] ANDO spectrum analyser Model number: AQ6317

[xvi] Bentham monochromator Model Number: TM300.

found to depend upon the mirror contact and position, and correspond to transitions of nearly equal emission cross-section, originating from the second Stark level of the $^4F_{3/2}$ manifold. The 1.318μm transition terminates on the first Stark level, and the 1.338μm transition the third, of the $^4I_{13/2}$ manifold [11].

	$^4F_{3/2}\rightarrow{}^4I_{9/2}$	$^4F_{3/2}\rightarrow{}^4I_{11/2}$	$^4F_{3/2}\rightarrow{}^4I_{13/2}$	$^4F_{3/2}\rightarrow{}^4I_{15/2}$
Wavelength (μm)	0.946	1.064	1.318/1.338	1.833
Maximum output power (W)	3.5	4.3	2.7	0.4[1]
Slope efficiency η_s w.r.t. absorbed power (%)	57	58	36	7

[1] Laser power accounts for output from both ends of the cavity.

Table 3-1: Summary of laser performance for the four transitions studied in Nd:YAG.

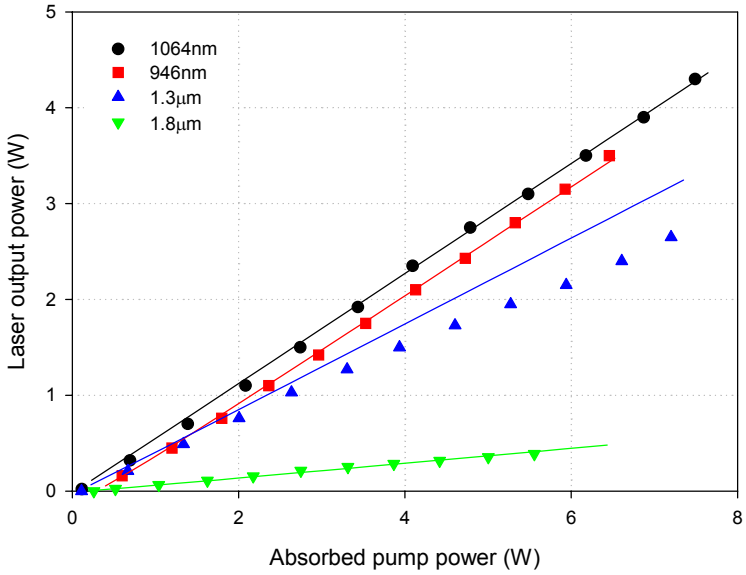

Figure 3-4: Laser output power versus absorbed pump power for the ● $^4F_{3/2}\rightarrow{}^4I_{9/2}$, ■ $^4F_{3/2}\rightarrow{}^4I_{11/2}$, ▲ $^4F_{3/2}\rightarrow{}^4I_{13/2}$, and ▼ $^4F_{3/2}\rightarrow{}^4I_{15/2}$ transitions. The symbols represent the experimental data while the solid lines were obtained by numerically solving equation (2.5)

Laser output power for the four transitions as a function of the absorbed pump power is represented by the data points in Figure 3-4. The percentage of the 9.7W of available pump power that was absorbed depended upon the coupling optics transmission, launch efficiency, mirror transmissions, and absorption coefficient; consequently it varied between each transition. For the 946nm, 1.064μm and 1.3μm transitions, the output power

was maximised by optimising the output coupler reflectance (mirrors with reflectivity spaced by 5-10%, depending upon the transition, were available). It was found that the above reflectance values agreed well with the theoretical optimum calculated by solving equation (2.5) as a function of the output coupling. The results of Figure 3-4 show very efficient multi-Watt operation for the transitions that used an optimised resonator and, in general, good agreement with the theoretical plots, represented by the solid lines.

The output beam quality was determined by measuring the second-moments radius as it propagated through a beam waist. Firstly, both axes were collimated with cylindrical lenses of focal lengths $f_x = 150$mm and $f_y = 25$mm, for the x and y axes defined in Figure 3-3. Then, after attenuating the beam via a single reflection from an uncoated glass wedge and passing it through a plano-convex lens of 50mm focal length, the second-moments radius or 'variance' was measured using a Gentec Beam-Scope[xvii] scanning slit, mounted on a translation stage. A Gaussian-propagation fitting function was used to determine the M^2 for the two independent axes defined by the waveguide. These results give $M_x^2 = 1.00\pm0.02$ and $M_y^2 = 1.28\pm0.05$, as shown in Figure 3-5 along with a beam profile image from a CCD camera.

The slightly higher M^2 value in the guided axis may be due to the fact that the doping fraction of 0.67 is greater than the calculated value for strict fundamental-mode selection, especially as the intra-cavity laser intensity is ~ 100 times the saturation intensity for Nd:YAG, $I_s = 2.3\text{kWcm}^{-2}$. A slightly smaller doping fraction would therefore improve the beam quality at the expense of an increased absorption length. It is also possible that the small increase in M^2 was due to the lenses used to collimate and focus the waveguide output beam during the M^2 measurement. In either case, it is clear that the double-clad waveguide laser can produce a high-spatial-quality output beam.

The measurement shown in Figure 3-5 was for a flat-flat cavity operating on the $^4F_{3/2} \rightarrow {}^4I_{11/2}$ transition formed by a high reflectance mirror and the Fresnel reflectance of a bare end face, i.e. an output coupler reflectance of ~8%. With this arrangement an output power of ~1W was observed for a maximum available pump power of 9.7W. The use of this cavity for beam quality measurements was necessary to circumvent beam profile

[xvii] Gentec EO, Québec, QC, G2E 5N7, Canada

instability caused by the relative movement between two mirrors mounted on the waveguide end faces. Particularly over the relatively long time required to make a full M^2 measurement. Coating directly onto the waveguide end faces would alleviate this problem as described earlier. Observation of the output beam at higher output powers using a CCD camera showed no noticeable degradation in the beam profile from that shown in the inset of Figure 3-5.

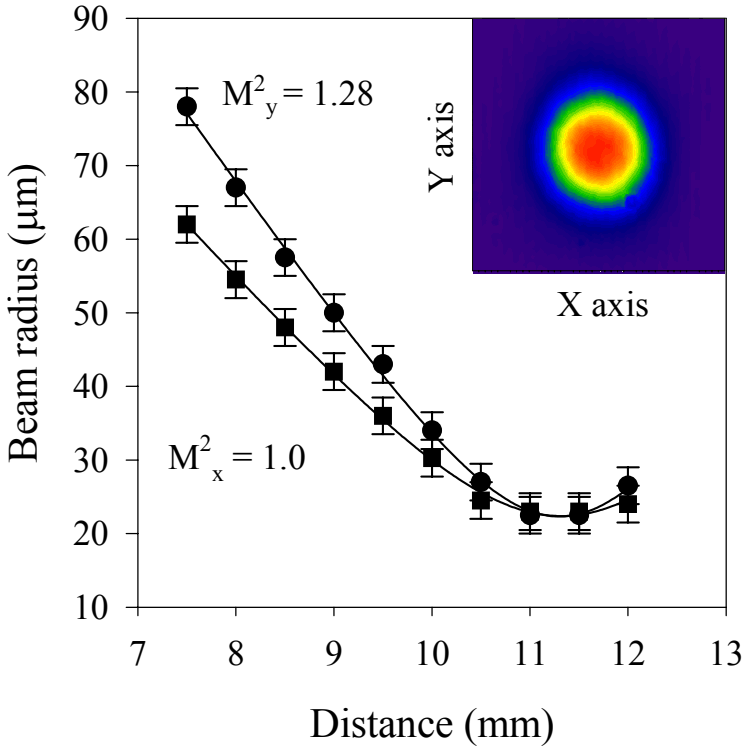

Figure 3-5: Beam quality measurement of a collimated output beam. Inset is the collimated beam intensity profile captured on a CCD camera.

3.3.4 Modelling

3.3.4.1 Introduction

To apply the analysis of Chapter 2 to the LMA double-clad planar waveguide structure one must first define the doping profile, and then the pump and lasing photon distributions. A schematic of the double-clad waveguide is shown in Figure 3-3, indicating the coordinate system used for the following analysis. In the planar waveguide structure investigated, the core region was Nd^{3+}-doped YAG, with un-doped YAG inner-cladding

layers and an outer-cladding of sapphire. Thus the doping distribution may be described by a step function over the core volume

$$d(x,y,z) = \frac{1}{t_{core} w l} \qquad |y| \le \frac{t_{core}}{2}$$

(3.2)

where t_{core} is the core thickness, w is the width of the waveguide and l the length.

For a highly multimode waveguide structure, as used here, the pump distribution may be assumed to be uniform across the doped core, consistent with exciting a large number of waveguide modes. However, in the plane of the waveguide, where there is no guiding structure, the pump beam is assumed not to diffract greatly and is approximated by a Gaussian profile with an average beam radius ω_{px}. Finally, if we consider pumping through the cavity high-reflectance mirror and allowing for double-pass absorption through the reflectance of the output coupler at the pump wavelength R_p^{oc}, the normalised pump photon density can be described by

$$r(x,y,z) = \frac{\alpha \exp\left(\frac{-2x^2}{\omega_{px}^2}\right)\left[1 + R_p^{oc}\exp(-2\alpha(l-z))\right]\exp(-\alpha z)}{\sqrt{\frac{\pi}{2}}\omega_{px} d\left(1 + R_p^{oc}\exp(-\alpha l)\right)(1-\exp(-\alpha l))} \qquad |y| \le \frac{t_{core}}{2}$$

(3.3)

The reduced pump absorption coefficient, α, accounts for the double-clad nature of the waveguide structure as discussed in Chapter 2 section 2.4.4. It should be noted that this equation assumes that the integration limits in the x-axis are much greater than the average pump beam radius ω_{px} (i.e. that the pump beam is smaller than the width of the waveguide, w).

In the unguided plane of the resonator, the pumping mode size, diffraction-losses, and the thermal effects define the laser mode. For the monolithic case with plane mirrors on the end faces of the waveguide, the laser mode will have negligible diffraction over the cavity length and is once again assumed to have a Gaussian profile with an average beam radius, ω_{lx}. Our last assumption is that the laser power stays constant (i.e. we assume small output coupling). As such the lasing photon distribution, which is in a fundamental guided mode far from cut-off, can be described by,

$$\phi(x,y,z) = \frac{2\sqrt{2}}{\sqrt{\pi}\omega_{lx}t_w l}\cos^2\left(\frac{\pi y}{t_w}\right)\exp\left(\frac{-2x^2}{\omega_{lx}^2}\right) \quad \textbf{(3.4).}$$

Again it should be noted that this equation assumes that the integration limits in the x-axis are much greater than the average beam radius ω_{lx}.

3.3.4.2 Laser performance

The parameters used in modelling the laser performance that have not already been discussed in the text, are given in Table 3-2. The value for the pump absorption coefficient takes into account the decrease in absorption efficiency due to the LMA double-clad waveguide structure. The launch efficiency of the pump was estimated from the measured pump waist size in the guided axis and the known waveguide dimensions.

The dimensions of the lasing mode were determined by imaging the output face of the waveguide onto a CCD camera or scanning slit, measuring the image dimensions, and then calculating the original mode size from the magnification of the imaging system. Measurements of guided-mode radii for the different signal wavelengths (except for 1.8μm) were found to be 13 ± 1μm, which is close to that predicted theoretically. The in-plane mode radii were measured as 120 ± 15μm, dependent upon the wavelength of operation. For simplicity this single value for signal beam radius was used in the performance modelling. The instruments used to measure the mode sizes were not sensitive to 1.8μm, and so we assumed that this mode was also of similar dimensions. It should be noted that the Rayleigh range for the non-guided beam waist is much longer than the crystal length, confirming our assumption of negligible diffraction over the length of the cavity. The values for the emission cross-sections are those commonly found in the literature [12, 13] adjusted, if necessary, to take into account our use of the factor f^l, which is the combined fractional populations of the Stark levels involved. In the case of the 1.833μm transition we were unable to find a value for the cross-section and have used a fitted value as described below. The basic background propagation loss of the waveguide was then the only parameter to be fitted to our results and gave a figure very near to our expected level of ~0.1dB/cm.

Modelling parameters.				
Pump Wavelength λ_p (μm)			0.807	
Maximum pump power (W)			9.7	
Average in-plane pump beam radius, ω_{px}, (μm)			128	
Pump Absorption coefficient (m^{-1})			0.02	
Coupling optics transmission (%)			89	
Launch efficiency (%)			93	
Transitions (lifetime τ=230µs)	$^4F_{3/2}\rightarrow{}^4I_{9/2}$	$^4F_{3/2}\rightarrow{}^4I_{11/2}$	$^4F_{3/2}\rightarrow{}^4I_{13/2}$	$^4F_{3/2}\rightarrow{}^4I_{15/2}$
Combined fractional pop. f^l at 300 K	0.61	0.4	0.4	0.6
Emission cross section, σ ($x10^{-24}$ m^2)	4	65	24	1.2
HR mirror transmission at λ_p (%)	82	95	92	89
O/C mirror reflectivity at λ_p, R_p^{OC} (%)	98	99	93	11
O/C mirror reflectivity at λ_l, R_l^{OC} (%)	87	78	81	99.2[1]
Cavity round trip loss exponent, L	0.05[2]	0.04	0.04	0.04
Lower laser level population, n_1^0	$1.1x10^{24}$	0	0	0
Lasing mode radius, ω_{lx} (μm)	120	120	120	120

[1] Reflectance value is the combined reflectance of the two cavity mirrors.

[2] Additional loss due to HR mirror reflectivity of ~99 %.

Table 3-2: Summary of parameters used to model the laser performance for the four transitions studied in Nd:YAG.

Perhaps the most impressive performance is for the quasi-three-level 946nm transition shown in Figure 3-4. The laser results appear to compare favourably with other recent reports of diode-pumped 946nm bulk lasers [14, 15] as shown in Table 3-3. While direct comparisons are hard to make due to the different pump sources used in these experiments, the results suggest an advantage for the waveguide in terms of efficiency, beam quality and cooling requirements.

The only transition to show significant deviation from the expected behaviour is that at 1.3µm. From the work of Guyot et al [16, 17] it would appear that this behaviour can not be attributed to upconversion or excited-state absorption effects, which are known to cause problems in Nd^{3+}-doped glass in this wavelength region [18]. As has already been noted, there are two competing wavelengths of operation for the $^4F_{3/2}\rightarrow{}^4I_{13/2}$ transition, it is tentatively suggested that there is significant gain at the non-lasing wavelength, which is

also within the wavelength range to see significant feedback from the resonator, thus affecting the output power of the lasing transition.

Gain Medium	Diode Pump Source	Incident Pump Power (W)	Output Power (W)	M^2	Cooling
Bulk [14]	Beam-shaped diode bar	13.6	3.0	1.5	Active
Bulk [15]	Fibre-coupled diode bar	22	5.3	3	Active
Waveguide (this work)	Beam-shaped, polarisation coupled broad-stripe diodes	8.6	3.5	1.0 x 1.3	Passive

Table 3-3: Comparison of recent reported results for multi-Watt diode pumped 946nm Nd:YAG lasers.

Figure 3-4 illustrates that a low gain transition such as $^4F_{3/2} \rightarrow {}^4I_{15/2}$ can benefit from the guided geometry. Data for the emission cross-section at 1.833μm is not available but the branching ratio to this wavelength region is ~50 times less than that for the 1.06μm region [19], and reports of laser operation appear to be very restricted with, to our knowledge, just one previously reported result for diode pumping [20]. In that result 3mW of output was obtained for 2.2W of pump, with active cooling down to a temperature of –28°C. The result reported here already shows considerably more power with no active cooling, and a good theoretical fit to our results is obtained using a ~70 times smaller cross-section than that for the 1.064μm transition. Unfortunately a range of mirrors to optimise the output coupling for this transition was unavailable, but the theoretical prediction from using equation (2.5), and the experimentally fitted emission cross-section, is that 1.7W of output power could be obtained with a 90% reflectivity output coupler for the experimental configuration detailed. However, in order to avoid lasing at 1.064μm the resonator mirrors would need less than 2.5% reflectivity at this wavelength. A compromise of using a 95% reflectivity output coupler would still give 1.4W of output at 1.833μm, with a requirement of less than 10% reflectivity at 1.064μm. It is again hard to draw fair comparisons between this performance and what might be expected in a bulk configuration, as there are a large number of parameters to adjust for optimum performance in each set-up. Nevertheless, noting that the guided mode size of 13μm is ~9 times smaller than the bulk confocal focussing condition for the described pump source and crystal length, the available gain in the waveguide is increased by an order of magnitude compared to the bulk configuration.

3.3.4.3 Spatial mode selection

An analysis of the spatial-mode selectivity for the longitudinally pumped waveguide, using equations (2.7) and (2.8) and the guided-mode spatial distributions defined by equations (3.2)-(3.4), leads to a similar conclusion that as long as the doping ratio t_{core}/t_w (see Figure 3-3(a)) is kept below 0.6 then fundamental-mode operation is strictly selected. Note however, this analysis assumes $\Delta n = 0$, which is expected to scale with refractive index step as demonstrated in chapter 2 for the side-pumped configuration. Thus in the analysis of laser operation in the double-clad waveguide only the fundamental guided mode was considered. The modal gain against doping fraction curves, as shown in Figure 3-6 for the case of high signal saturation, are very similar for 4-level (at 1064nm) or quasi-three-level operation (at 946nm), at least for the experimental parameters described here, suggesting that the second term in equation (2.7), when integrated in equation (2.8), has a negligible effect.

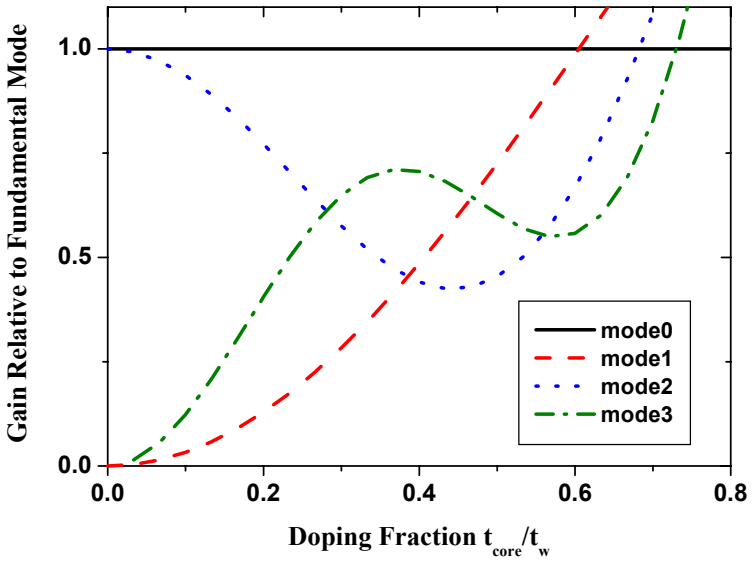

Figure 3-6: Relative gain for the first four guided modes at 946nm against doping fraction for a resonating one-directional power 100 times greater than the saturation power.

3.3.4.4 Thermal characteristics

The waveguide investigated herein was treated as a 6-layer hetero-structure (the doped-core region being split into two equally thick layers for the purposes of our modelling), with an infinitely thin heat source between them, as illustrated in Figure 3-7. The structure is symmetric with the characteristics of each layer type detailed in the table of Figure 3-7.

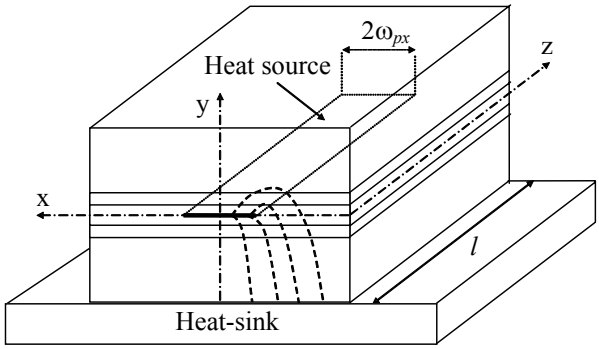

	Sapphire	YAG	Nd:YAG
Thermal conductivity k_i (W/mK)	35	13	13
Thickness	3 mm	5 μm	10 μm

Figure 3-7: Schematic of a rectangular stripe heat source at the centre of the active waveguide core. Model layer characteristics included. The heavy dashed lines representing thermal flux contours between heat source and sink are for visualisation purposes only.

Figure 3-8 shows the calculated temperature profile as a function of the in-plane coordinates (x, z), and represents the temperature at the heat source, i.e. the centre of the waveguide core. For a heating power of ~1.0W deposited into a stripe of width $2\omega_{px} = 256\mu m$, the peak temperature rise at the front face of the waveguide is ~6.4K, falling to 1.6K at the rear face of the structure. This heating power is consistent with the quantum defect heating expected in our experiments when lasing on the $^4F_{3/2} \rightarrow {}^4I_{9/2}$ transition, which, due to its quasi-three-level nature, is the most susceptible to increases in temperature. Three notes should be made at this point. Firstly, if the thermal conductivity of the sapphire layer in the above model is changed to that of YAG, the peak temperature rise at the front face increases to ~16 K, which is 2.5 times that shown in Figure 3-8. This illustrates that the structure's thermal resistance is dominated by the properties of sapphire rather than the active host material YAG. Secondly, reducing the sapphire substrate thickness to 250 μm, which would give an overall waveguide thickness of ~ 0.5mm, would halve the temperature rise. Thirdly, the temperature rise could of course be further reduced by heat sinking both faces of the waveguide.

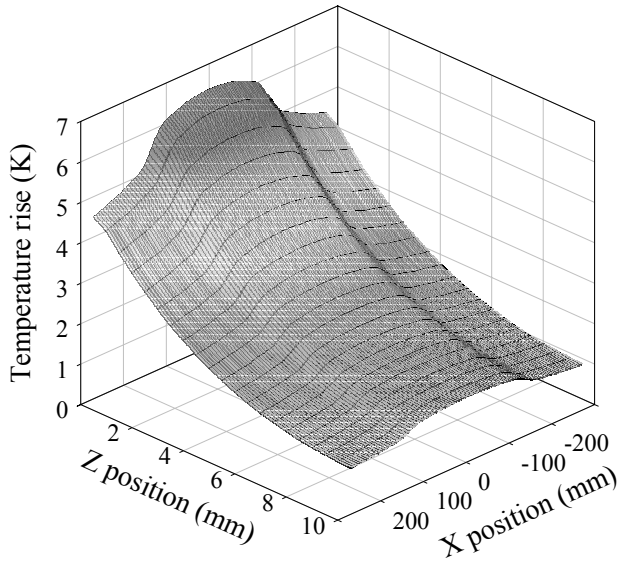

Figure 3-8: Temperature profile at the centre of the waveguide core, y=0, assuming a stripe heat source width 256μm and a heating power of ~1.0 W.

It should also be noted that an interesting advantage of using a highly multimode waveguide, from which fundamental mode operation is selected, is that the same waveguide can be used for operation at a large range of wavelengths. In the laser results demonstrated here, there is a factor of two between the longest and shortest wavelength transitions, and in fact the waveguide design would be effective for wavelengths well beyond the transmission window of YAG.

3.4 Er:YAG large mode area planar waveguide laser

3.4.1 Introduction

Tri-valent Erbium as the active ion in crystal hosts has gathered increasing importance for infra-red sources around the peak in the water absorption spectra at 2.9μm [21]. Primarily driven by medical applications, where the strong absorption coefficient ($\alpha \sim 10\,000 cm^{-1}$) leads to a penetration depth of the order of one micron, allows highly precise microsurgery with minimal damage to surrounding areas. Moreover laser sources around this wavelength are also of interest for remote sensing applications corresponding to a small transmission window in the water vapour absorption spectrum [22].

Notwithstanding the complex energy dynamics of the Er^{3+} ion, Watt-level diode-pumped outputs have been demonstrated with bulk Er:YAG lasers in the QCW [23, 24] and CW

[25, 26] regime. Some of the energy transfer mechanisms for Er:YAG are illustrated in Figure 3-9. CW operation of the ~2.8μm transition of Er:YAG is only possible with intense pumping and high doping concentrations, up to ~50at.%Er. This is found to be dependent upon population recycling through upconversion, circumventing "bottle-necking" at the lower laser level that otherwise self-terminates laser action [27, 28]. It should be noted that the fluorescence lifetime of the upper laser level manifold, $^4I_{11/2}$, is $\tau_u \sim 100\mu s$, almost two orders of magnitude shorter than the lower laser manifold, $^4I_{13/2}$, $\tau_l \sim 4\text{-}10ms$ [27].

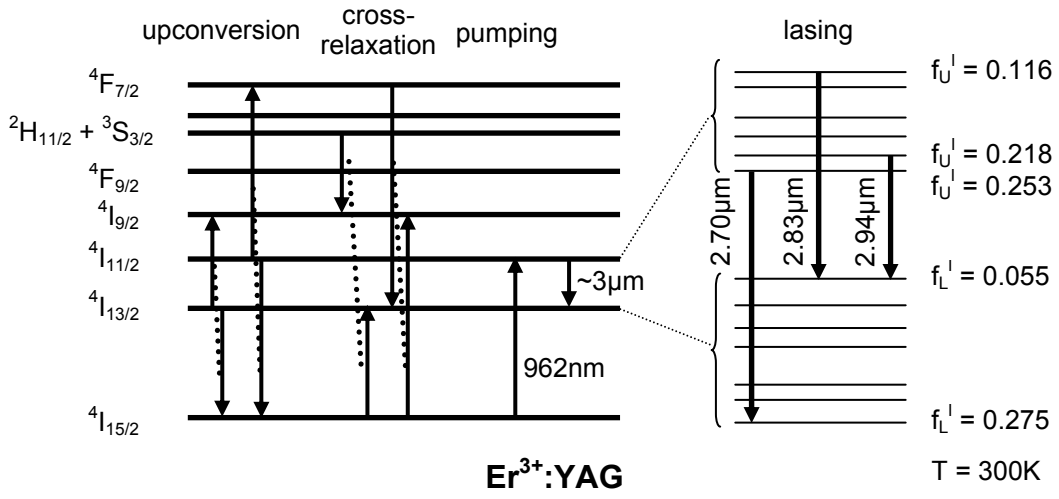

Figure 3-9: Transfer processes and energy level diagram for Er:YAG, illustrating the Stark level splitting's and the respective fractional populations ($f_{U,L}^l$) for the stronger transitions.

Reportedly other hosts, i.e. garnets such as GGG or YSGG, and fluoride crystals i.e. YLF and BaYF, have better spectroscopic properties than YAG for ~2.8μm operation when doped with Er^{3+} active ions [28-30]. However, the advantageous thermo-mechanical properties of YAG often dictate its use in high-average-power applications.

Two advantages associated with the planar waveguide geometry are high gains and intense pumping, both requirements for the ~2.8μm Er:YAG transition. In addition, the thermal management benefits of the LMA planar waveguide as demonstrated in section 3.3.4.4 offer a reduced temperature rise, beneficial in lowering the laser threshold and increasing slope efficiency [26, 31]. Presented in the following sections are the preliminary findings for the first reported diode-pumped Er:YAG double-clad waveguide laser.

3.4.2 Experimental set-up

The 1cm-long YAG/Sapphire LMA waveguide structure, fabricated by Onyx Optics using the direct bonding technique, is of the same design as that shown in Figure 3-3, with Erbium rather than Neodymium doping, i.e. t_{core}=20μm and t_w=30μm. A 50at.% Er^{3+}-doping concentration was selected to maximise absorption and upconversion [23, 26]. One sapphire substrate was polished to a thickness of ~300μm and the other ~4mm. The end faces of the guide were uncoated and polished plane and parallel, to within a few minutes of arc.

A pump source was constructed using two 4W SDL Inc.[xviii] CW InGaAs broad-stripe diode lasers (DL), as pictured in Figure 3-10. The diodes' centre wavelengths were ~958 nm at 25°C and a full driving current of 4.75A. Each diode was mounted on separate aluminium heatsinks (HS) affixed to thermo-electric (TE) cooling devices that removed the waste heat and controlled the temperature, through which the centre wavelength could be tuned. Connected in electrical series, both diodes had a common drive current leading to a voltage drop of ~3.5V and a maximum power consumption of ~17W. Similarly the TE coolers were also connected in series, implying that both diodes were cooled at the same rate, where the close match in centre wavelength meant it was unnecessary to have independent control. A PT100 platinum temperature sensor (S) fixed to one diode mount monitored the heatsink temperature for external control.

Collimation of the diodes' fast-axes was achieved using Doric fibre lenses[xix] (C1), with a focal length of f_y ~ 1mm. These lenses, positioned with a micro-positioning stage, were fixed to the diode heatsink with ultra-violet curable cement at the fibre ends. This fast bonding technique minimised the effects of defocus (beam-quality degradation) associated with shrinkage of the curing glue. That is, the shrinkage occurs along the axis of the fibre lens perpendicular to the optical axis and independent of the sensitive positioning requirements. Similarly, for the slow axis collimation an f_x ~ 4mm plano-convex lens (C2) was positioned and fixed to the heatsink using the same technique. The outputs of the two collimated TE polarised diodes were then combined via a broadband cube polarisation

[xviii] SDL Inc. now JDS Uniphase. Diode part number - SDL 6380-A

[xix] Graded index fibre lens, manufacturer - Doric Lenses Inc, Ancienne-Lorette, Canada.

beam-splitter (PBS) after the polarisation of one diode had been rotated by 90° using a half-wave plate (λ/2). To optimise the overlap of the beams in the far field, two thin BK7[xx] circular wedges (W) were fabricated, which when used as a pair could steer one beam over a cone angle of ~ 4°. All optics were AR coated for the pump wavelength. As shown in Figure 3-10, the whole assembly could be fully enclosed in a protective housing with an output window for the pump beam to exit. The completed diode pump source module was then mounted on an air-cooled heatsink, circumventing the need for an external cooling unit as typically required in high-average power lasers.

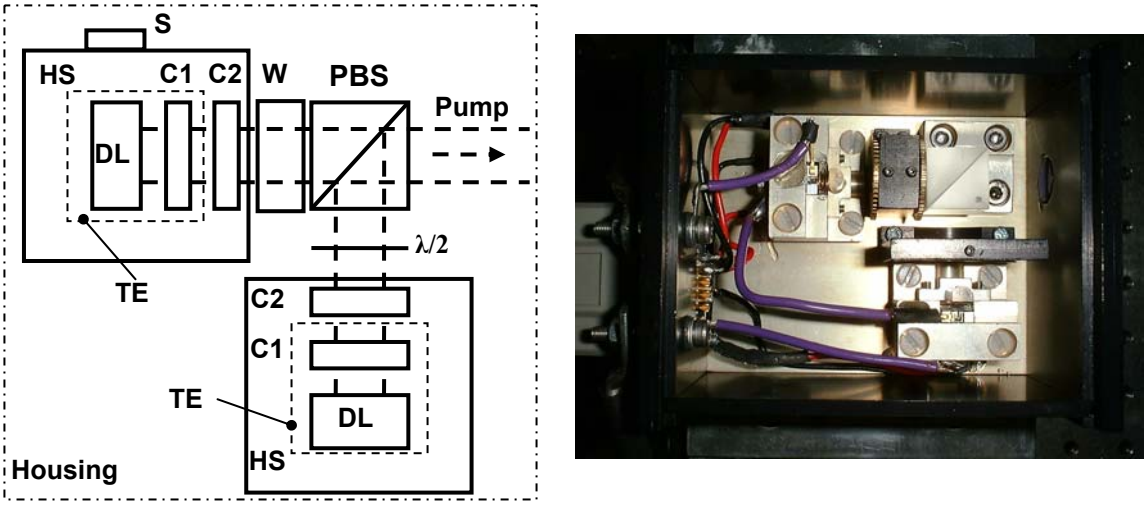

Figure 3-10: Diode pump source set-up, constructed for end-pumping experiments.

The beam-quality of the orthogonal axes from the diode pump source was measured using a Gentec beam-scope, giving beam quality parameters of $M_x^2 = 23.5 \pm 0.5$ and $M_y^2 = 2.5 \pm 0.1$. Full-width half-maximum (FWHM) angular divergences were also measured, giving $\theta_x = 15 \pm 2$mrad and $\theta_y = 2.2 \pm 0.1$mrad. The centre wavelength could be temperature tuned at a rate of ~0.25nm/°C, whereas it would shift at a rate of ~1.9nm/A with increasing the diode current.

Using a similar configuration to that introduced in section 3.3.2, the optical coupling scheme is shown in Figure 3-11. Here the x-axis of the pump beam is conditioned by a

[xx] Borosilicate Schott glass.

cylindrical-spherical beam-reducing telescope and the y-axis simply focussed into the waveguide via the spherical lens module. This lens combination had a pump transmission of 90 ± 1% over the full pump source power range. The pump beam-quality was degraded in both axes to $M_x^2 = 30 \pm 1$ and $M_y^2 = 4 \pm 0.5$ due to the aberrations incurred passing through the coupling optics.

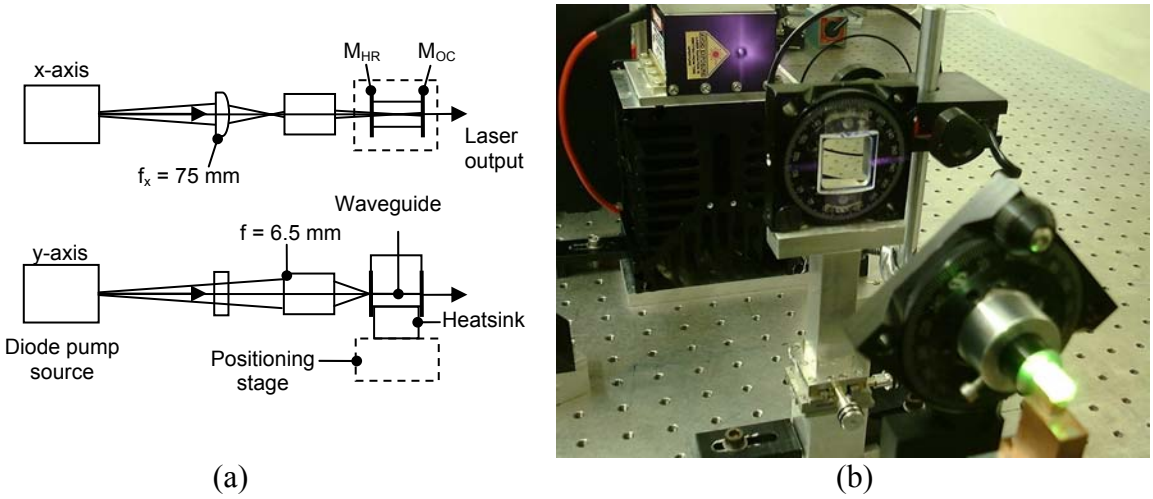

Figure 3-11: (a) Schematic and (b) photo of optical coupling scheme for end-pumping configuration.

The waveguide, bonded to a water-cooled copper block with thermally-conductive adhesive, was oriented with the thin substrate closest to the heatsink for optimum heat removal. The water-cooled heatsink was fixed to a precision positioning stage for alignment with respect to the pump focus. Thin lightweight single-side coated mirrors were attached to the end faces of the plane-plane waveguide structure as described previously in section 3.3.2. It should be noted that Fluorinert, the liquid used to hold the mirrors in place, does not show significant absorption at the wavelengths of interest.

A monochromator and liquid nitrogen cooled InSb photo-detector were used to verify the laser wavelength. To reduce back-ground noise the photo-detector was covered with a Germanium filter with a cut-off wavelength of ~1.6μm. Mechanically chopping[xxi] the pump beam, the amplified photo-detector output and chopper frequency were passed to a lock-in amplifier[xxii]. The lock-in amplifier output was then recorded by a computer as it

[xxi] Stanford Research chopper driver Model number: SR540

[xxii] Stanford Research Model Number: SR530

scanned the monochromator grating across the wavelength range of interest, generating an image of the laser spectrum. Calcium Fluoride (CaF) lenses were required to image the laser output beam onto the entrance slit, due to strong absorption in BK7 around the expected operating wavelength.

3.4.3 Laser performance

At a maximum operating current of 4.75A and when heated to 45°C the diode pump source had a centre wavelength of ~962nm with a spectral width of $\Delta\lambda \sim 6$nm, therefore coupling to the upper three Stark levels of the $^4I_{11/2}$ manifold. After the conditioning optics the maximum incident pump power was ~5.3W. The measured beam waist in the y-axis was $8 \pm 0.5\mu$m and in the x-axis $97 \pm 3\mu$m, positioned ~2.7mm inside the waveguide. Single pass absorption, under non-lasing conditions, and as a function of the diode current was determined by measuring the pump power with and without the waveguide in place. A Molectron[xxiii] thermopile detector was used for the pump and laser power measurements, with a Germanium filter covered when measuring the laser power to ensure only radiation of wavelength longer than 1.6μm was detected. A maximum output power of 450mW was observed for ~4.5W of absorbed pump.

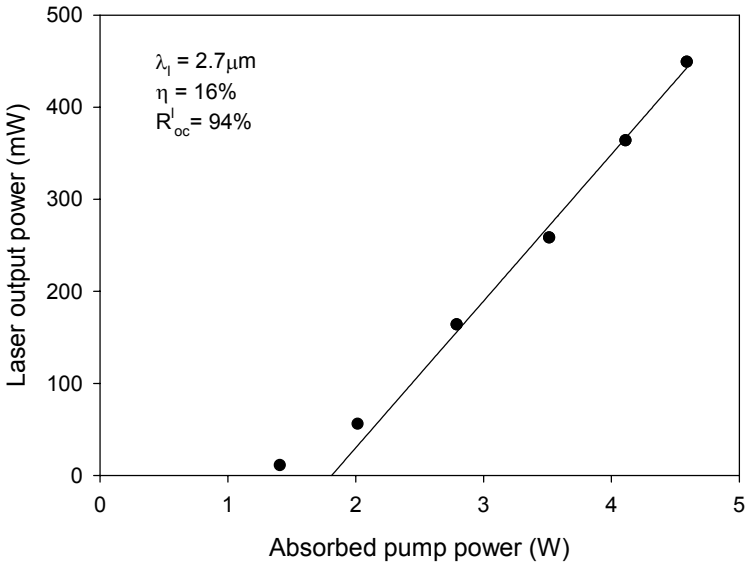

Figure 3-12: Laser output power as a function of absorbed pump power.

[xxiii] Laser power detectors , Molectron Europe Ltd., UK - Model Numbers: PM10, PM150

The laser output power as a function of absorbed pump power observed for an output coupler reflectance of $R_l^{oc} = 94 \pm 3\%$ is shown in Figure 3-12, from which a slope efficiency of 16% was obtained. Note the large error range for the output coupler reflectance is a result of etalon effects associated with the uncoated second surface of the thin mirror. A double pass of the pump and a varying input mirror transmission, from 78 – 86%, were included in the calculation of absorbed pump power as a function of the central diode wavelength dependence on the diode current.

The laser wavelength was determined to be 2695 ± 3nm, corresponding to the transition between the lowest Stark levels of the $^4I_{11/2}$ and $^4I_{13/2}$ manifolds, as indicated in Figure 3-9. This transition has the largest stimulated emission cross section, $\sigma = 5.1 \times 10^{-20} cm^2$ [28], of the commonly observed wavelengths shown in Figure 3-9 [23, 26]. There was no evidence of the other two indicated Stark level transitions, despite the use of mirrors with lower output coupling at these wavelengths.

The output power was found to be dependent upon the stability of the mirror contact, the mirrors moving significantly more than in the previous experiments with the Nd:YAG LMA PW laser. Reasonable mirror contact could only be maintained at high powers for less than a few minutes at a time. Notwithstanding, the output beam appeared to be single lobed when viewed on a heat sensitive card, as illustrated by Figure 3-13. Although

Figure 3-13: Picture of Er:YAG LMA PW laser output, viewed on a heat sensitive card.

determination of the beam quality was not possible due to the temporary nature of the cavity mirrors attachment, an approximate measure of the beam width in the unguided axis was made. A single-slit Gentec beam-scope with an InAs detector sensitive to the laser wavelength, was positioned within a few millimetres of the output coupler and the measurement taken whilst chopping the pump beam with a 50% duty cycle, thus reducing the thermal load on the cavity and providing a longer stability period. A second-moments beam radius of ~230μm was observed, with the profile having a good fit to Guassian, indicating that it may have been near-diffraction limited.

3.4.4 Discussion

Achieving efficient CW laser operation with Er^{3+} ions around 2.9μm is an ongoing research topic that involves accounting for many of the possible energy transfer dynamics, including their dependence upon the host medium [28-30]. Therefore although a complete study of the laser performance is not undertaken here, suggestions for the observed performance and future optimisation are proposed.

Firstly it is noted that high pumping intensity is required to enhance the upconversion recycling of excited ion population from the lower to upper laser levels, in fact pump intensities >50kWcm^{-2} have been suggested [24]. A ~1W end-pumped monolithic laser reported by Chen *et al.*, essentially the bulk equivalent to the laser described here, required speciality high-power diffraction-limited diode lasers as its pump source with an incident intensity of ~140kWcm^{-2}. The experiment described here with two standard broad-stripe high-power diodes and 20% more pump power delivered an intensity of ~220kWcm^{-2} to the waveguide structure. These levels are approaching the $\lambda_p \approx 963$nm pump saturation intensity for Er:YAG, i.e. $I^p_{sat} \approx 350$kWcm^{-2} [22]. Additionally the spatial dependence of the pump intensity will also affect the available gain in longitudinally pumped configurations. Consequently the length of the cavity with respect to the absorption length will play a significant role in the overall laser efficiency. A possible factor in the lower than expected efficiency for the laser described here, was that the 1cm cavity was significantly longer than the expected small signal absorption length of ~1mm [23].

Despite the cavity mirrors having a lower output coupling at the longer wavelengths indicated in Figure 3-9, the laser wavelength was found to be 2.7μm. This can be

understood by noting that for an end-pumped laser, the threshold pump power may be written as [32],

$$P_{th} \propto \frac{(L+T)}{\sigma} \qquad \textbf{(3.5).}$$

Thus for transitions with a common upper laser level manifold and the same pump and laser field distribution, the threshold for each transition is dependent upon the cavity loss and its respective cross-section, σ. Where L is the round trip cavity loss exponent and T_l^{oc} is the cavity output coupling. Any loss associated with reabsorption at the laser wavelength can be included in the parameter L. Assuming a round trip loss L = 0.07 (~0.16dBcm^{-1}) common to each wavelength, the threshold condition for the 2.7μm transitions is smaller than the others as shown in Table 3-4. Therefore lasing on this transition is expected as it is the first to reach threshold, as was experimentally observed.

Laser wavelength (μm)	Stimulated emission cross-section (x 10^{-20} cm^{-2}) [28]	$T_l^{OC}=-ln(R_l^{HR}R_l^{OC})$ (%)	$P_{th} \propto \frac{(L+T_l^{oc})}{\sigma}$
2.7	5.1	7.2	0.028
2.8	3.4	3.1	0.030
2.9	2.6	3.3	0.040

Table 3-4: Determination of the relative threshold for the dominant Stark level transitions between the $^4I_{11/2} \rightarrow {}^4I_{13/2}$ manifolds. An approximation for the round trip cavity loss, L = 0.07 has been used, consistent with the other LMA PW lasers investigated.

As discussed in chapter 2 the mode selection properties of the LMA PW laser can enforce single-mode behaviour in the guided axis. It was highlighted however that if the refractive index step between the doped and un-doped YAG layers is too great, the induced waveguide becomes isolated from the outer cladding, negating the mode selection properties of the double-clad structure. According to Akhmetov *et al.* [33] there is a linear increase in refractive index of 2.2 x 10^{-4} per at.% Erbium, in Er:YAG. Therefore the index step expected between 50at.% Er:YAG and un-doped YAG is Δn ~ 0.01. Following the same process discussed in Chapter 2, this index step and a laser wavelength of 2.94μm implies robust single-mode selection for a waveguide aperture of t_w = 30μm (see Figure 3-3) limits the core thickness to d = 11μm. Such a doping ratio would result in an

absorption coefficient ~37% of uniformly doped Er:YAG, with a similar decrease in pump intensity.

CW operation of the $^4I_{11/2} \rightarrow {}^4I_{13/2}$ transition in an end-pumped Er:YAG LMA PW has been demonstrated for the first time. This preliminary study suggests laser operation could be further optimised for greater efficiency and to target the 2.94μm wavelength specifically. Identified improvements include reducing the cavity length with respect to the absorption length, coating the end faces of the waveguide directly and ensuring that the figure of merit described by equation (3.5) is smallest for the 2.94μm transition. Furthermore it is suggested that the dielectric coatings be designed such that they have minimal water ingress and an extremely high damage threshold. Finally, for robust single-mode performance the index step between core and inner-cladding should be verified and the core thickness adjusted accordingly. Alternatively index matching techniques could be employed for the core-inner cladding layers. For example using an equivalent Tm^{3+} doping concentration in the YAG inner-cladding to that of Er^{3+} in the core, where Tm^{3+} has no absorption around the wavelengths of interest, would reduce the index step to $0.3x10^{-4}$ per at.%. Therefore waveguides with large apertures as investigated here would still be able to select fundamental guided-mode performance.

3.5 Summary

Discussed in this chapter were the first multi-Watt CW demonstrations of an end-pumped Nd:YAG LMA PW laser at three different wavelengths. In addition, operation on a fourth but very weak transition of Nd:YAG at ~1.8μm, was achieved. These results illustrate the remarkable versatility of the PWL to operate either in a high-power or high-gain regime, whilst maintaining good spatial-mode-control independent of the operating wavelength.

Increasing the wavelength range offered by the LMA PW lasers, ~0.5W Er:YAG double-clad waveguide laser operating at 2.7μm was realised. Further refinements to the oscillator configuration could be expected to deliver multi-Watt outputs at the highly desirable wavelength of 2.94μm. High pump intensities and good thermal characteristics are paramount for this active material, which requires small temperature rises and a large population inversion to counteract population "bottle-necking" in the terminal 3μm laser level, both of which are easily achieved with the planar waveguide structure.

Models for the laser and thermal performance of the end-pumped LMA PW lasers were found to match well with the observed characteristics of these devices. Low threshold powers, high slope-efficiencies, good electrical to optical efficiency, and negligible temperature effects with minimal cooling requirements, are all characteristics that offer compact, simple, and efficient high-power laser systems useful for a variety of applications.

3.6 References

[1] W. Koechner, *Solid State Laser Engineering - Chapter 5*, vol. 1, 4th ed. Berlin Heidelberg: Springer Verlag, 1999.

[2] D. P. Shepherd, S. J. Hettrick, C. Li, J. I. Mackenzie, R. J. Beach, S. C. Mitchell, and H. E. Meissner, "High-power planar dielectric waveguide lasers," *Journal of Physics D-Applied Physics*, vol. 34, pp. 2420-2432, 2001.

[3] W. A. Clarkson, "Thermal effects and their mitigation in end-pumped solid-state lasers," *Journal of Physics D-Applied Physics*, vol. 34, pp. 2381-2395, 2001.

[4] D. P. Shepherd, C. L. Bonner, C. T. A. Brown, W. A. Clarkson, A. C. Tropper, D. C. Hanna, and H. E. Meissner, "High-numerical-aperture, contact-bonded, planar waveguides for diode-bar-pumped lasers," *Optics Communications*, vol. 160, pp. 47-50, 1999.

[5] R. J. Beach, S. C. Mitchell, H. E. Meissner, O. R. Meissner, W. F. Krupke, J. M. McMahon, W. J. Bennett, and D. P. Shepherd, "Continuous-wave and passively Q-switched cladding-pumped planar waveguide lasers," *Optics Letters*, vol. 26, pp. 881-883, 2001.

[6] C. L. Bonner, T. Bhutta, D. P. Shepherd, and A. C. Tropper, "Double-clad structures and proximity coupling for diode-bar- pumped planar waveguide lasers," *IEEE Journal of Quantum Electronics*, vol. 36, pp. 236-242, 2000.

[7] D. Findlay and R. A. Clay, "The measurement of internal losses in 4-level lasers," *Physics Letters*, vol. 20, pp. 277-8, 1966.

[8] C. T. A. Brown, C. L. Bonner, T. J. Warburton, D. P. Shepherd, A. C. Tropper, D. C. Hanna, and H. E. Meissner, "Thermally bonded planar waveguide lasers," *Applied Physics Letters*, vol. 71, pp. 1139-1141, 1997.

[9] S. Guy, C. L. Bonner, D. P. Shepherd, D. C. Hanna, and A. C. Tropper, "High-inversion densities in Nd:YAG: Upconversion and bleaching," *IEEE Journal of Quantum Electronics*, vol. 34, pp. 900-909, 1998.

[10] J. I. Mackenzie, C. Li, D. P. Shepherd, H. E. Meissner, and S. C. Mitchell, "Longitudinally diode-pumped Nd:YAG double-clad planar waveguide laser," *Optics Letters*, vol. 26, pp. 698-700, 2001.

[11] A. A. Kaminskii, *Laser Crystals - Chapter 4*, vol. 14. Berlin Hiedelberg: Springer Verlag, 1990.

[12] T. Y. Fan and R. L. Byer, "Modeling and CW Operation of a Quasi-3-Level 946nm Nd-YAG Laser," *IEEE Journal of Quantum Electronics*, vol. 23, pp. 605-612, 1987.

[13] W. Koechner, *Solid State Laser Engineering - Chapter 2*, vol. 1, 4th ed. Berlin Heidelberg: Springer Verlag, 1999.

[14] W. A. Clarkson, R. Koch, and D. C. Hanna, "Room-temperature diode-bar-pumped Nd:YAG laser at 946 nm," *Optics Letters*, vol. 21, pp. 737-739, 1996.

[15] P. Zeller and P. Peuser, "Efficient, multiwatt, continuous-wave laser operation on the $^4F_{3/2} \rightarrow {}^4I_{9/2}$ transitions of Nd:YVO_4 and Nd:YAG," *Optics Letters*, vol. 25, pp. 34-36, 2000.

[16] Y. Guyot and R. Moncorge, "Excited-State Absorption in the Infrared-Emission Domain of Nd^{3+}-Doped $Y_3Al_5O_{12}$, $YLiF_4$, and $LaMgAl_{11}O_{19}$," *Journal of Applied Physics*, vol. 73, pp. 8526-8530, 1993.

[17] Y. Guyot, H. Manaa, J. Y. Rivoire, R. Moncorge, N. Garnier, E. Descroix, M. Bon, and P. Laporte, "Excited-State-Absorption and Up-Conversion Studies of Nd^{3+}-Doped-Single Crystals $Y_3Al_5O_{12}$, $YLiF_4$, and $LaMgAl_{11}O_{19}$," *Physical Review B*, vol. 51, pp. 784-799, 1995.

[18] P. R. Morkel, M. C. Farries, and S. B. Poole, "Spectral Variation of Excited-State Absorption in Neodymium Doped Fiber Lasers," *Optics Communications*, vol. 67, pp. 349-352, 1988.

[19] A. A. Kaminskii, *Laser Crystals - Chapter 1*, vol. 14. Berlin Hiedelberg: Springer Verlag, 1990.

[20] T. S. Kubo and T. J. Kane, "Diode-Pumped Lasers at 5 Eye-Safe Wavelengths," *IEEE Journal of Quantum Electronics*, vol. 28, pp. 1033-1040, 1992.

[21] D. M. Wieliczka, S. S. Weng, and M. R. Querry, "Wedge Shaped Cell for Highly Absorbent Liquids - Infrared Optical-Constants of Water," *Applied Optics*, vol. 28, pp. 1714-1719, 1989.

[22] S. A. Payne, R. J. Beach, C. Bibeau, C. A. Ebbers, M. A. Emanuel, E. C. Honea, C. D. Marshall, R. H. Page, K. I. Schaffers, J. A. Skidmore, S. B. Sutton, and W. F. Krupke, "Diode arrays, crystals, and thermal management for solid-state lasers," *IEEE Journal of Selected Topics in Quantum Electronics*, vol. 3, pp. 71-81, 1997.

[23] C. E. Hamilton, R. J. Beach, S. B. Sutton, L. H. Furu, and W. F. Krupke, "1-W Average Power Levels and Tunability from a Diode-Pumped 2.94μm Er-YAG Oscillator," *Optics Letters*, vol. 19, pp. 1627-1629, 1994.

[24] C. Ziolek, H. Ernst, G. F. Will, H. Lubatschowski, H. Welling, and W. Ertmer, "High-repetition-rate, high-average-power, diode-pumped 2.94μm Er:YAG laser," *Optics Letters*, vol. 26, pp. 599-601, 2001.

[25] B. J. Dinerman, "3μm CW Laser Operations In Erbium-Doped YSGG, GGG, and YAG," *Optics Letters*, vol. 19, pp. 1143-1145, 1994.

[26] D. W. Chen, C. L. Fincher, T. S. Rose, F. L. Vernon, and R. A. Fields, "Diode-pumped 1-W continuous-wave Er:YAG 3μm laser," *Optics Letters*, vol. 24, pp. 385-387, 1999.

[27] W. Q. Shi, M. Bass, and M. Birnbaum, "Effects of Energy-Transfer among Er^{3+} Ions on the Fluorescence Decay and Lasing Properties of Heavily Doped Er-$Y_3Al_5O_{12}$," *Journal of the Optical Society of America B-Optical Physics*, vol. 7, pp. 1456-1462, 1990.

[28] S. A. Payne, L. K. Smith, and W. F. Krupke, "Cross-Sections and Quantum Yields of the 3μm Emission for Er^{3+} and Ho^{3+} Dopants in Crystals," *Journal of Applied Physics*, vol. 77, pp. 4274-4279, 1995.

[29] M. Pollnau, T. Graf, J. E. Balmer, W. Luthy, and H. P. Weber, "Explanation of the CW Operation of the Er^{3+} 3μm Crystal Laser," *Physical Review A*, vol. 49, pp. 3990-3996, 1994.

[30] M. Tikerpae, S. D. Jackson, and T. A. King, "Theoretical comparison of Er^{3+}-doped crystal lasers," *Journal of Modern Optics*, vol. 45, pp. 1269-1284, 1998.

[31] R. Spring and W. Luthy, "Temperature-Dependence of a 2.94μm YAG-Er Laser and Population of the Laser Levels," *Journal of Applied Physics*, vol. 69, pp. 581-583, 1991.

[32] W. P. Risk, "Modeling of Longitudinally Pumped Solid-State Lasers Exhibiting Reabsorption Losses," *Journal of the Optical Society of America B-Optical Physics*, vol. 5, pp. 1412-1423, 1988.

[33] S. F. Akhmetov, G. L. Akhmetova, G. A. Gazizova, V. S. Kovalenko, and T. F. Mirenkova, "Rare Earth Metal Aluminium Garnets," *Russian Journal of Inorganic Chemistry*, vol. 22, pp. 1613-1615, 1977.

Chapter 4

END - PUMPED PASSIVELY Q-SWITCHED WAVEGUIDE LASERS

4.1 Introduction

Several applications require very high power optical sources, although not always of a continuous nature, for example: non-contact distance measurements for mapping or range-finders; remote-sensing for metrology or hazardous environments; materials processing such as welding, cutting, and marking; also non-linear optical conversion for which onset occurs only at very high intensities. In general to exceed the Mega-Watt peak power barrier requires; costly, bulky, and complex laser systems. Consequently there is significant interest to develop affordable, compact, robust, and high-power Q-switched devices that are more readily used in field applications or industrial environments, rather than the laboratory alone.

All solid-state passively Q-switched (PQS) lasers have been demonstrated to provide a compact efficient method for generating high-peak-power sources without the additional complexity of actively controlled switches [1]. These devices operate through fast optical saturation effects that increase a medium's transmission under the influence of high-intensity radiation, i.e. saturable absorption. Microchip lasers [2] are well suited for diode-pumped compact sources and when configured with an intra-cavity passive Q-switch, can deliver high peak powers at a single-frequency [3]. A Nd:YAG microchip laser has been reported to operate at peak power levels approaching the MW regime [2]. Here we investigate waveguide lasers similar in design to the microchip laser but instead utilising the double-clad waveguide geometry to benefit from higher gains and better thermal management properties, offering greater average power scalability.

The following sections of this chapter describe the first known demonstration of PQS end-pumped double-clad planar waveguide lasers. Firstly though, a brief introduction to the concept of passive Q-switching using Cr^{4+}-doped YAG as a saturable absorber (SA) and a CW-pumped active medium, is required. After which the operation and performance of a

Yb:YAG PQS LMA PW laser is described; similarly a Nd:YAG PQS LMA PW laser was also demonstrated although found to be unsuited to high-power operation in the end-pumped waveguide configuration.

4.2 Passive Q-switching concept

Laser Q-switching is a well understood phenomenon discussed in many textbooks (for example see [4-6]. Q-switching denotes a technique used to generate "giant pulses", that is pulses of short duration and high peak power. This is achieved by spoiling the resonator quality factor, Q [7], such that a large population inversion density and thus high gains may be created. Whereupon switching the cavity-Q to a high value, that is reducing the round trip loss, on a time scale comparable to the resonator round trip time, permits rapid amplification of the oscillating field that sweeps out the available gain. Repeating the process generates a train of high peak power laser pulses.

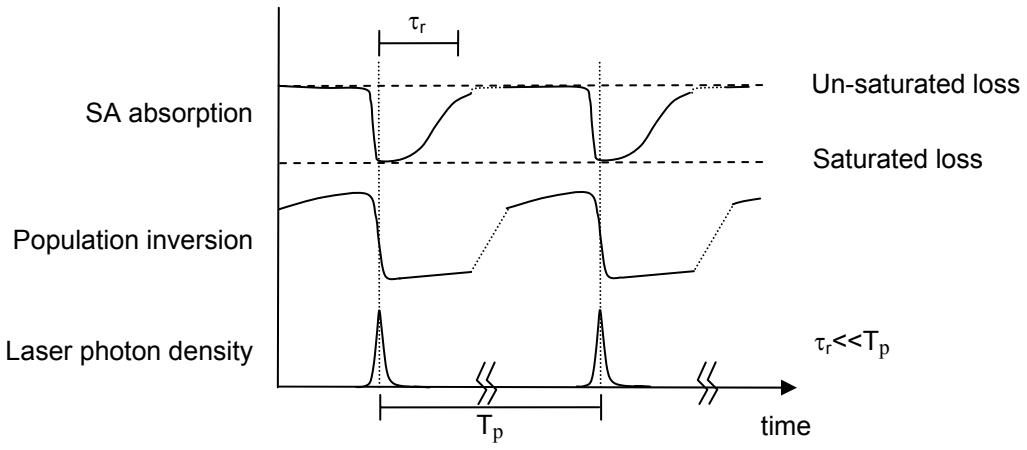

Figure 4-1: Timing diagram for a passively Q-switched laser, with a saturable absorber recovery τ_r much faster than the time between pulses, T_p.

Passive Q-switching is achieved by placing an optically-saturable absorbing medium intra-cavity. Following the timing diagram of Figure 4-1, initially the SA absorption is high, frustrating amplification of an oscillating field, whereby with continued pumping the population inversion increases until the round-trip gain is equal to the total loss of the resonator, including the saturable loss of the passive Q-switch. Above threshold, the amplified intra-cavity laser field reduces SA absorption to its saturated loss state. The increasing laser photon density reaches a maximum when the gain is reduced to the non-saturable cavity loss, whereby a proportion of the remaining population inversion is

promptly extracted to complete a "giant" pulse. For a SA with fast recovery, τ_r, the initial small-signal saturable loss is restored before significant gain is recreated through ongoing pumping leading to a repetitive pulse train, of period T_p, defined by the pumping rate and residual population inversion density after each laser pulse.

Advantages of the PQS laser are derived from the simplification of the overall system through the use of fewer components, requiring no external voltage or radio frequency drivers or controllers to actively modulate the cavity loss. Similarly due to the relatively insensitive alignment requirements for saturable absorbing materials, integration into the laser system is quite easy. Disadvantages include a reduced ability to control or vary the pulse characteristics that are defined by the gain area and resonator loss, and pulse to pulse timing jitter associated with fluctuations in the resonator parameters pertaining to the threshold condition, e.g. cavity length, pumping rate, or intra-cavity loss. However, recently techniques based on modulating the pumping rate have been reported to reduce timing jitter in PQS lasers, [8, 9].

4.2.1 Cr^{4+}:YAG saturable absorber

Several different media have been used as saturable absorbers in laser systems, i.e. gases, dyes, semiconductors, and crystal impurities or dopants, see reference [4] and those therein. G Youxi *et al.* were the first to demonstrate self-Q-switching with a doped YAG crystal exhibiting gain and saturable loss [10]. Subsequently Zharikov *et al.* also demonstrated saturable absorption properties of Chromium-doped garnets around 1μm, leading to PQS behaviour of Nd,Cr:GSGG [11-13]. Several years later there appeared renewed interest with further reports of Cr^{4+}-doped YAG demonstrating "self" Q-switching when co-doped with Neodymium [14, 15]. Yankov [16] then extended these investigations using several Nd-doped hosts and a discrete Cr^{4+}:YAG element. Due to the opto-mechanical robustness of YAG and the long term stability of Cr^{4+} ions in the crystal lattice, this material has gained considerable acclaim for compact PQS lasers. An all-solid-state option was chosen here for its simplicity, compactness, and compatibility. Further, having the same host material for the active and saturable ions favoured easy integration via the direct-bonding technique, into the waveguide structures.

Treated as a four-energy-level system, the specifics of which are still not well understood due to screening effects by other ions in the crystal host, Cr^{4+} has two dominant energy transfer processes to consider [17]. As detailed in Figure 4-2, ground-state absorption

(GSA) occurs between the $^3A_2$ (level 1) and $^3T_2$ (level 2) electronic states, where level 2 rapidly decays through phonon interactions to the ^1E (level 3) excited state. A second photon absorption can occur from the excited-state level 3 to a higher energy state, level 4, where it is believed to decay nonradiatively back to level 3. Thus excited-state absorption (ESA) is an extra source of loss and must be accounted for when modelling PQS laser performance [18].

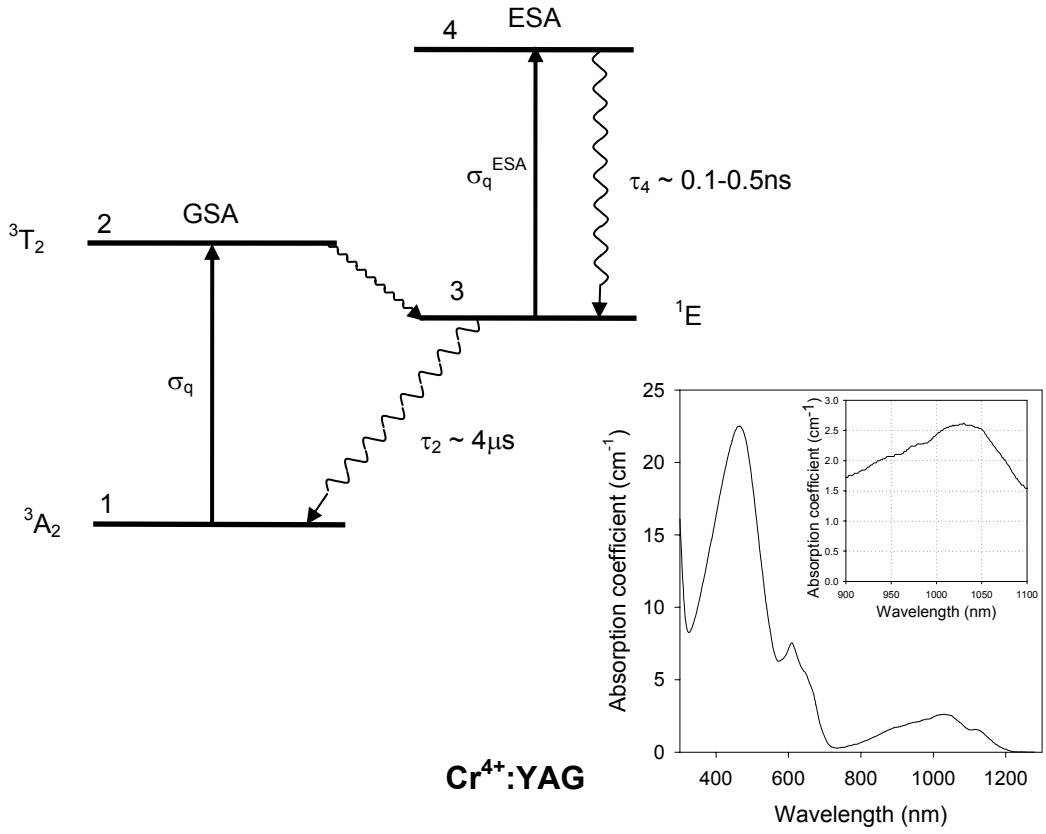

Figure 4-2: Energy level diagram for Cr^{4+}:YAG, showing ground state and excited state absorption transitions, (GSA) and (ESA) respectively. Cr^{4+} absorption spectra after [19]

Xiao and Bass [18] extended the general optimised solutions for passive Q-switching reported by Degnan [20] to include ESA. Subsequently Patel and Beach [21] introduced a new formalism, based on earlier work of Beach [22] that allowed for sensitivity studies away from the optimum solution. In the following section the equations of Patel and Beach are reviewed and modified slightly to account for the LMA PW geometry and non-uniform doping.

4.2.2 Passive Q-switching theory

As was first detailed by Szabo and Stein [23], the laser photon density within a PQS oscillator can be described by a system of coupled differential equations. Patel and Beach present a model based on a plane wave analysis that is well suited to the waveguide geometry investigated here. As such the coupled differential equations for the laser photon density and population inversion densities in the active and saturable material are given by [21],

$$\frac{d\phi(t)}{dt} = \frac{c\eta_{lo}\phi(t)}{l_{cav}}\left[\Delta n_l(t) l_l \sigma_l + \Delta n_q(t) l_q \sigma_q\left(1 - \frac{\sigma_q^{ESA}}{\sigma_q}\right) - n_{0q} l_q \sigma_q^{ESA}\right] + \frac{c\phi(t)}{l_{cav}}\ln\left(\sqrt{T_{sp}^2 R_{OC}^l}\right)$$

$$\frac{d\Delta n_l(t)}{dt} = -f^l c\eta_{lo}\sigma_l \Delta n_l(t)\phi(t), \qquad f^l = f_L^l + f_U^l$$

$$\frac{d\Delta n_q(t)}{dt} = -f^q c\eta_{lo}\sigma_q \Delta n_q(t)\phi(t), \qquad f^q = f_L^q + f_U^q$$

(4.1)

where: $\phi(t)$ is the intra-cavity laser photon density; c is the speed of light; η_{lo} is the overlap of the laser field with the doped region of the LMA waveguide; l_{cav} is the optical cavity length; $\Delta n_i(t)$ is the population inversion density, l_i the length, and σ_i the spectroscopic cross section referenced to the appropriate transition Stark levels, with Boltzmann occupation factors $f_{L,U}^i$ of the L (lower) and U (upper) energy manifolds corresponding to the laser wavelength, for $i = l, q$, being the gain and saturable media respectively; σ_q^{ESA} is the excited-state cross section for the SA at the laser wavelength; n_{0q} is the concentration of the absorber ion; T_{sp} is the single-pass transmission corresponding to cavity losses not associated with the SA; and lastly R_l^{oc} is the output coupling reflectance.

Note the equations of (4.1) differ slightly from that given in [21] whereby non-uniform doping, i.e. the LMA PW, is catered for via the term η_{lo}. Solving equations (4.1) one obtains a transcendental equation for the output pulse energy:

$$E_{out} = \frac{A\ln\left(R_l^{oc}\right)}{2\frac{\sigma_q^{ESA}}{\sigma_q}\ln\left(T_q\right) + \ln\left(T_{sp}^2 R_l^{oc}\right)} \cdot \left\{ \begin{array}{l} \frac{F_l^{sat}}{\eta_{lo}}\ln\left(\frac{1}{\sqrt{T_q^2 T_{sp}^2 R_l^{oc}}}\right)\left[1 - \exp\left(\frac{2\eta_{lo}E_{out}}{F_l^{sat} A\ln\left(R_l^{oc}\right)}\right)\right] \\ + \frac{F_q^{sat}}{\eta_{lo}}\ln\left(T_q\right)\left(1 - \frac{\sigma_q^{ESA}}{\sigma_q}\right)\left[1 - \exp\left(\frac{2\eta_{lo}E_{out}}{F_q^{sat} A\ln\left(R_l^{oc}\right)}\right)\right] \end{array} \right\}$$

(4.2)

where A is the cross-sectional area of the laser field in the active medium; T_q is the small-signal transmission of the saturable absorber in the waveguide geometry given by $\exp(-n_{0q} l_q \eta_{lo} \sigma_q)$; and $F_i^{sat} = h\nu_l / f^i \sigma_i$ is the saturation fluence of the active ($i = l$) and passive Q-switch ($i = q$) material.

The temporal pulsewidth is calculated by taking the ratio of the pulse energy to the peak laser output power. This latter parameter is found by determining when the intra-cavity laser photon density reaches a maximum, i.e. equating the first expression of equations (4.1) to zero, then integrating over the population inversion density prior to and up until the peak of the Q-switched pulse, which results in:

$$\phi_{\max} = \frac{1}{\eta_{lo}\sigma_l f^l l_{cav}} \cdot \left\{ \begin{array}{c} \eta_{lo}\sigma_l \Delta n_l^{\text{int}} l_l \left(1 - \dfrac{\Delta n_l^{\max}}{\Delta n_l^{\text{int}}}\right) \\ + \xi \ln\left(T_q\right)\left(1 - \dfrac{\sigma_q^{ESA}}{\sigma_q}\right)\left[1 - \left(\dfrac{\Delta n_l^{\max}}{\Delta n_l^{\text{int}}}\right)^{1/\xi}\right] \\ + \left[\dfrac{\sigma_q^{ESA}}{\sigma_q}\ln\left(T_q\right) + \ln\left(\dfrac{1}{\sqrt{T_{sp}^2 R_l^{oc}}}\right)\right]\ln\left(\dfrac{\Delta n_l^{\max}}{\Delta n_l^{\text{int}}}\right) \end{array} \right\} \tag{4.3}$$

with new parameters $\xi = \sigma_l f^l / \sigma_q f^q$, and $\Delta n_l^{int\,(max)}$ the initial (maximum) population inversion density in the active material.

Thus the laser pulsewidth is given by,

$$\tau_p = \frac{2E_{out}}{\phi_{\max} h\nu_l cA \ln\left(\dfrac{1}{R_l^{oc}}\right)} \tag{4.4}.$$

The final parameter of interest, from an operational perspective, is the repetition rate at which the laser pulses are generated. Assuming that $\tau_p << T_p$, the time between subsequent pulses, the repetition rate is approximated by $1/T_p$. This is found numerically through determination of the time it takes for the population inversion density to reach Δn_l^{int}, from the post-pulse residual inversion, Δn_l^{fin} ;

$$\Delta n_l^{fin} = \Delta n_l^{\text{int}} \exp\left(\frac{2\eta_{lo} E_{out}}{F_l^{sat} A \ln(R_l^{oc})} \right)$$

(4.5).

Where $\Delta n_l{}^{int}$ is obtained noting that the term $\eta_{lo}\sigma_l \Delta n_l{}^{int} l_l$ represents the gain that trips the passive Q-switch, equivalent to the small-signal single-pass cavity loss, that is;

$$\eta_{lo}\sigma_l \Delta n_l^{\text{int}} l_l = \ln\left(\frac{1}{\sqrt{T_q^2 T_{sp}^2 R_l^{oc}}} \right)$$

(4.6)

and following the same method as detailed in Chapter 2 section 2.2.2, for the side-pumped laser modelling. Firstly, the manifold line-integrated population density and its rate of change due to the pumping field intensity, have to be defined.

$$N_j(t) = \int_0^{l_l} n_j(z,t) dz$$

(4.7)

is the manifold line-integrated population density, although now with respect to the longitudinal (z) axis and where ($j = L, U$) is the notation for the L – lower or U – upper energy level. The time rate of change of upper manifold line-integrated population density, $N_U(t)$, depends upon the pumping intensity, $I_p(t)$, through the expression,

$$\frac{dN_U(t)}{dt} = \frac{I_p(t)}{h\nu_p} F_A \left[1 + (1 - F_A) R_p^{oc} \right] - \frac{N_U(t)}{\tau_f}$$

(4.8),

with $h\nu_p$ the pump photon energy; R_p^{oc}, the reflectance at the pump wavelength of a mirror that allows for a double pass of the pump (noted as the output coupler here); τ_f the fluorescence lifetime of the upper manifold; and F_A the single-pass fractional pump absorption as defined by equation (2.13), although the Stark-level line-integrated population inversion density coupled by the pump radiation, ΔN^p, is now,

$$\Delta N^p(t) = \left(f_L^p + \frac{d_L^p}{d_U^p} f_U^p \right) N_U(t) - f_L^p n_{0l} l_l$$

(4.9).

Here the degeneracy factors, d_j^p, have been included for completeness, for pump radiation-coupled Stark levels of the lower and upper manifolds, with f_j^p the respective Boltzmann occupation factors, and n_{0l} the active ion concentration.

Using equation (4.6) and the expression for the Stark level line-integrated population inversion density coupled by the laser radiation,

$$\Delta N^l(t) = \left(\frac{d_U^l}{d_L^l} f_L^l + f_U^l \right) N_U(t) - \frac{d_U^l}{d_L^l} f_L^l n_{0l} l_l \tag{4.10},$$

where d_j^l are the degeneracy factors for laser radiation-coupled Stark levels of the lower and upper manifolds, with f_j^l the respective Boltzmann occupation factors. One obtains the expression for the population density of the upper manifold at the onset of the Q-switch pulse, t^{int},

$$N_U\left(t^{\text{int}}\right) = \frac{1}{\left(\frac{d_U^l}{d_L^l} f_L^l + f_U^l \right)} \left[\frac{d_U^l}{d_L^l} f_L^l n_0^l l_l - \frac{\ln\left(\sqrt{T_q^2 T_{sp}^2 R_l^{oc}}\right)}{\eta_{lo} \sigma_l} \right] \tag{4.11}.$$

Equation (4.11) sets the target upper manifold population for the numerical solution of equation (4.8), from which the last parameter of interest, the build up time and hence repetition rate is found.

4.3 Yb:YAG large mode area planar waveguide laser

4.3.1 Introduction

Yb:YAG is attracting growing interest as a competitor to Nd:YAG for high-power laser sources due to its low quantum defect, broad absorption and emission lines, lack of upconversion losses, and comparatively high saturation fluence [21, 24]. The two-level energy scheme of Yb:YAG, derived from the crystal field splitting of the ^{2}F electronic state, is shown in Figure 4-3 [25]. Pump and laser wavelengths used in the following experiments and fractional Stark levels population at 300K are listed beside the appropriate levels.

Due to its relatively long fluorescence lifetime of ~0.95ms and therefore greater energy

storage capacity [26], Yb:YAG is capable of producing higher energy Q-switch pulses than similar laser configurations using Nd:YAG as the active medium [21]. To date passive Q-switching of bulk Yb:YAG lasers has been achieved using semiconductor saturable absorber mirrors (SESAM) [27] and Cr^{4+}:YAG as a saturable absorber [28, 29]. Reported here is the first demonstration of an end-pumped PQS double-clad Yb:YAG waveguide laser with an integrated Cr^{4+}:YAG SA. Highly efficient operation was achieved, with near-diffraction-limited output, when pumped by two polarisation-coupled broad-stripe laser diodes.

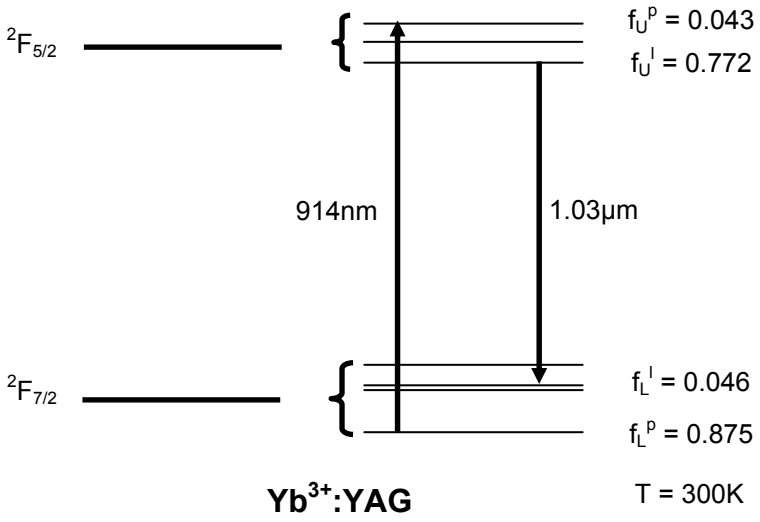

Figure 4-3: Energy level diagram for Yb:YAG.

4.3.2 Experimental set-up

The configuration of the 1cm-long waveguide, fabricated by Onyx Optics using the direct bonding technique, is shown schematically in Figure 4-4. As demonstrated in the previous chapter, the high numerical aperture LMA YAG/sapphire waveguide allows efficient coupling of high-power diode sources. In addition, restricting the 10at.% Yb^{3+}-doping to the 8µm-thick central YAG layer leads to preferential operation on the fundamental spatial-mode. A Cr^{4+}:YAG section, situated centrally in the core region, acts as a saturable absorber to provide passively Q-switched operation. The saturable absorber is 540µm long, had a measured absorption coefficient of 4.34cm^{-1} at 1.064µm, and was placed in the centre of the cavity so that spatial-hole burning would have a maximum effect on longitudinal mode selection [2]. Therefore the corresponding bulk small signal

transmission is ~76% for the SA thickness used here. The waveguide had coatings applied directly to its polished end-faces to form a plane-plane laser cavity with an output coupler reflectivity of $R_l^{oc} = 20\%$

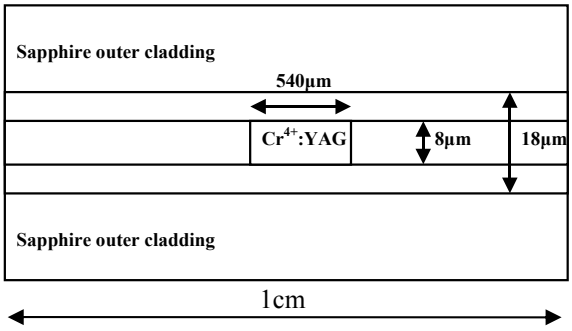

Figure 4-4: Schematic diagram of the double-clad waveguide used in these experiments.

Using the same pump source design as detailed in section 3.4.2 two polarisation-coupled broad-stripe diodes operating around 914nm were used for these experiments. The absorption at this wavelength, although less than that of the more commonly used pump wavelengths of 941nm or 968nm, was sufficient for the purpose of the experiment. A schematic of the pump source and optical coupling scheme is illustrated in Figure 4-5. The diode output beams were collimated in both axes using two cylindrical lenses (C1 and C2) and combined, after polarisation rotation of one via a half-wave plate, at the polarising beam splitter (PBS). For an electrical power of 16.3W the source supplies a maximum optical power of 7.2W incident on the first cylindrical beam-conditioning lens (C3). The final spherical focussing lens (FL) provides measured second-moments beam-radii waists of 7.5 ± 0.5µm in the guided (y)-axis and 100 ± 3µm in the unguided (x)-axis, with M^2 values of 3.5 ± 0.5 and 21 ± 1, respectively. The y-axis beam waist was situated at the entrance to the waveguide while the x-axis beam waist was just over 3mm inside the waveguide. The waveguide was originally fabricated for side-pumping thus the cavity mirror coatings were not optimised for this set-up. Therefore to maximise pump input into the waveguide it was necessary to orient the composite with the output coupler at the pump input face. Consequently the laser signal was directed back toward the pump source and required the use of a dichroic mirror (D) to extract useful output.

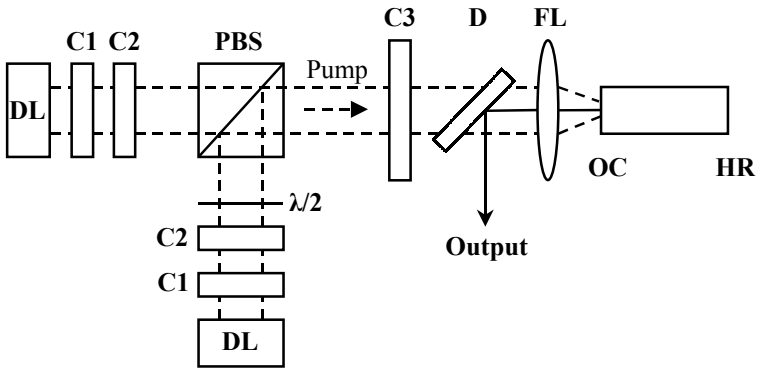

Figure 4-5: Experimental arrangement: broad-stripe diode lasers DL, cylindrical collimating lenses C1 (f_y=1mm) and C2 (f_x=4mm), half-wave plate λ/2, polarising beamsplitter PBS, beam conditioning lens C3 (f_x=75mm), focussing optic FL (f=6.5mm), and dichroic mirror D.

The centre wavelength of the diode emission, which had a ~5nm bandwidth, changed with increasing current from 908nm to 914nm. At a constant diode cooling temperature the single-pass pump absorption was measured to increase from 0.6 to 0.79 over the full 0 - 4.8A current range, ignoring waveguide propagation losses and the pump-transmission of the passive Q-switch. From the measurements of the unabsorbed transmitted pump power and with the knowledge of the transmission of the optics and mirror coatings at the pump wavelength, the absorbed pump power was calculated as a function of drive current. The resultant values were consistent with reported absorption cross-sections in this wavelength range and the reduced absorption due to the double-clad structure [24, 25].

4.3.3 Laser performance

Figure 4-6 (a) shows the average output power versus diode power (incident on lens C3 in Figure 4-5) characteristic for this laser. A maximum of 2.3W output was measured after the dichroic splitter with a corresponding slope efficiency of ~46%. The efficiency with respect to absorbed power (~53%) is only slightly higher than this value due to the changing absorption efficiency with increasing pump power. The onset of pulsed laser output occurred at a pump power of 1.37W and just below this threshold ~10mW of continuous wave output was observed. Figure 4-6(a) also shows how the pulse repetition frequency increases approximately linearly to a maximum value of 77kHz. The error bars indicate the observed increase in timing instability at the higher frequencies. This behaviour has been reported previously [30] and was attributed to the fact that, at such

high frequencies, the time between pulses approaches the excited state lifetime of the Cr^{4+} ion. Figure 4-6(b) illustrates a typical pulse train from the passively Q-switched waveguide laser using a large-area silicon low-bandwidth photodetector, such that the variation observed is due to changes in pulse to pulse energy, which itself is attributed to the variation in the timing jitter in the pulse switching. Measurements of the full-width half-maximum pulsewidth using a detector with a bandwidth of 1GHz and a 500MHz digital oscilloscope[xxiv], indicated stable values with a small decrease from just over 2ns to 1.6ns with increasing pump power. This change in pulsewidth is presumed to be due to a variation in the population inversion distribution, as suggested by equations (4.3) and (4.4). Similarly both the pulse energy and the peak power show a steady increase with pump power up to values of ~30μJ and 18kW respectively. This behaviour is consistent with that reported for previous passively Q-switched Yb^{3+}-doped lasers using Cr^{4+}:YAG as a saturable absorber [27, 29, 31]. The highest intensity generated in the waveguide was ~$2x10^9$ Wcm^{-2} with no damage observed to the waveguide or coatings.

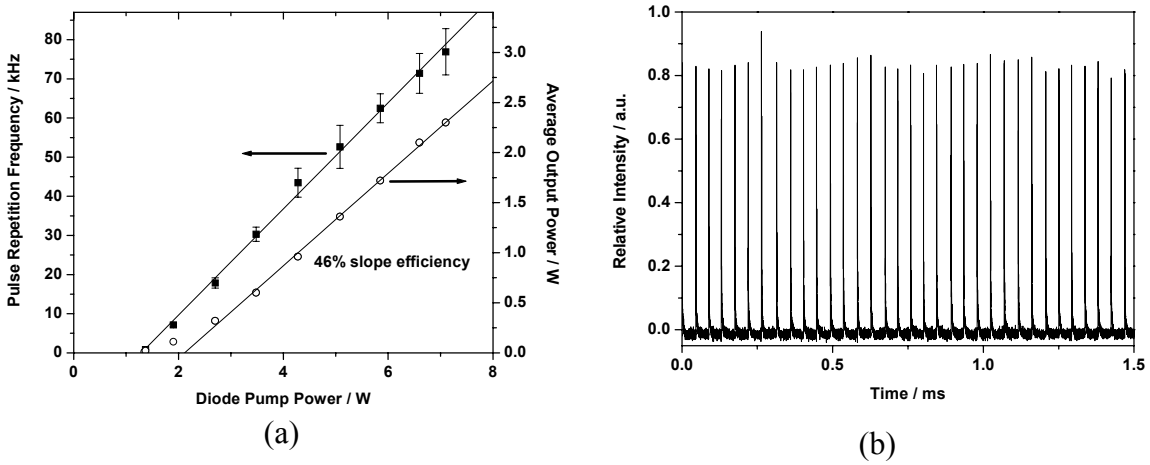

Figure 4-6: (a) Graph of pulse repetition frequency and average output power against diode pump power incident on lens C3 (Figure 4-5). (b) Trace of a typical output pulse train.

The output beam quality was assessed in the in-plane- and guided-axes using a dual slit Gentec Beamscope by measuring the second-moments beam radii around the foci of a 150mm focal length spherical lens. The laser output was first collimated in the unguided

[xxiv] Tektronix digital oscilloscope, Model number: TDS 7444A

axis using a 150mm cylindrical lens, noting that in the guided axis the beam was already well collimated by the pump focussing optic (FL, Figure 4-5). Attenuation was required, not to saturate the detector, and achieved via a single reflection from an uncoated glass wedge plus additional reflective filters. The M^2 values were found to increase from 1.0 in both axes near threshold, to 1.5 (x-axis) by 1.3 (y-axis) at high power. Thus, the double-clad waveguide structure, although designed for strict fundamental spatial-mode selection under continuous-wave operation, is also effective in this Q-switched regime.

As observed previously with LMA PW composites, the laser output was partially polarised, assumed to be due to induced stresses during the fabrication process. This attribute and the resultant output polarisation were found to depend upon the position across the width of the structure. Analysing the collimated beam with a polarisation beam splitter cube, the laser output was found to be typically >95% TM polarised. Thus this source would have suitable power and polarisation for non-linear conversion applications such as frequency doubling.

4.3.4 Discussion

Using the analysis described in section 4.2 with the parameters listed in Table 4-2, the calculated maximum pulse energy, pulsewidth, and repetition rate are in good agreement with measured results, as shown in Table 4-1.

	Model	Experiment
Pulse energy (μJ)	28.3	29.9±2.3 [1]
Pulsewidth (ns)	1.59	1.60±0.05
Repetition rate (kHz)	78	77±5

[1] Derived from average power x pulse to pulse period.

Table 4-1: Comparison of model to experimental results for Yb:YAG LMA PW laser.

One parameter strongly affecting the theoretical repetition rate is the pump intensity. Consequently, since the pump beam in the guided-axis may be approximated by a top-hat profile, consistent with the large multimode double-clad waveguide, a new parameter was introduced, η_{reduc}^{p}, which accounts for the reduction in pump intensity. This factor was calculated from the ratio of the maxima for Gaussian and Gaussian/top-hat area-normalised distributions. Although the cavity mode dimensions were not measured for this particular setup, values of ~120μm x 5μm were expected from previous end-pumped CW

measurements for the in-plane beam radii and the theoretical guided mode size for this waveguide design respectively. Furthermore the repetition rate and pulsewidth are dependent upon the ratio σ_q/σ_q^{ESA} and the laser field cross-sectional area, as one might imagine from equations (4.2)-(4.4). Thus, it was necessary to fit the values of σ_q and σ_q^{ESA}, which were found to be in reasonable agreement with those reported in references [17, 21], despite the different wavelength of interest and vast array of possible values reported in the literature, see references in [17], giving $\sigma_q = 3.6\text{x}10^{-19} - 7\text{x}10^{-18}$ cm^2 and $\sigma_q^{ESA} = 2.2\text{x}10^{-19} - 2\text{x}10^{-18}$ cm^2 at 1.064μm.

Active medium parameters			**Pump parameters**		
Laser photon energy (x10^{-19} J)	$h\nu_l$	1.93	Pump photon energy (x10^{-19} J)	$h\nu_p$	2.17
Laser field cross sectional area (x10^{-6} cm^2)	A	9.4	Pump intensity reduction factor	η_{reduc}^{p}	1.44
Spectroscopic cross section (x10^{-20} cm^2)	σ_l	2.46	Spectroscopic cross section (x10^{-20} cm^2)	σ_p	0.31
Laser lower-level fractional population (300K)	f_L^l	0.046	Pump lower-level fractional population (300K)	f_L^p	0.875
Laser upper-level fractional population (300K)	f_U^l	0.772	Pump upper-level fractional population (300K)	f_U^p	0.043
Laser saturation fluence (Jcm^{-2})	F_l^{sat}	9.58	Pump saturation fluence (Jcm^{-2})	F_p^{sat}	74.0
Ion concentration (x10^{20} cm^{-3})	n_{0l}	13.8	Pump power (W)	P_p	7.2
Gain medium length (cm)	l_l	0.946	Delivery efficiency	η_{del}	0.77
Saturable medium parameters			**Cavity parameters**		
Ground state absorption cross section (x10^{-18} cm^2)	σ_q	1.6	Optical cavity length (cm)	l_{cav}	1.81
Excited state absorption cross section (x10^{-18} cm^2)	σ_q^{ESA}	0.42	Refractive index	n	1.81
SA lower-level fractional population	f_L^q	1	Laser field overlap	η_{lo}	0.892
SA upper-level fractional population	f_U^q	0	Pump field overlap	η_{po}	0.444
SA saturation fluence (Jcm^{-2})	F_q^{sat}	0.09	Output coupler reflectance	R_l^{oc}	0.2
Small signal transmission (inc. laser field overlap)	T_q	0.785	Pump mirror reflectance	R_p^{oc}	0.4
SA length (cm)	l_q	0.054	Transmittance of measurement optics	T_m	0.94

Table 4-2: Modelling parameters for Yb:YAG LMA PW laser.

Amplified spontaneous emission is not expected to have the same detrimental affects on end-pumped performance as was suspected with the previously reported side-pumped configuration [30]. This is primarily due to the relatively small solid angle defined by the end-pumped configuration, and secondly the moderate initial gain required to trip the passive Q-switch saturation, i.e. the initial gain for the set-up described above was $\eta_{lo}\sigma_l\Delta n_l{}^{int} l_l \sim 1.1$.

In the pursuit of higher peak powers, halving the small-signal transmission of the Cr^{4+} saturable absorber whilst using the same analysis suggests that pulse energies >100μJ and pulsewidths of <500ps, at pulse repetition rates of ~20kHz, are feasible from the same set-up. Furthermore, decreasing the small-signal SA transmission (in the waveguide geometry) to ~20% and utilising the end face Fresnel reflectance as an output coupler of a 5mm long structure, theoretically at least, the MW peak power mark may be reached with ~0.14mJ/0.14ns pulses at a repetition rate of >10kHz. Optical damage to the coatings and/or crystal is ultimately likely to prevent these peak powers being achieved in the waveguide configuration described herein.

4.4 Nd:YAG large mode area planar waveguide laser

4.4.1 Introduction

The operation of a Nd^{3+}-doped LMA double-clad waveguide, similar in design to the Yb^{3+}-doped structure described in the previous section, was also investigated. End-pumped passively Q-switched performance at the laser wavelengths of 1.064μm and 946nm was demonstrated and found to be generally inferior to that of the Yb^{3+}-doped LMA PW in the waveguide configuration.

4.4.2 Experimental set-up

The set-up is similar to that described in section 3.3.2, using a beam-shaped pump source from unique m.o.d.e AG, which had an approximately square-shaped beam of $M^2 \approx 17$ in both axes. The pump power of ~10W at 807nm, could be efficiently launched into the large, high numerical aperture (NA=0.47) waveguide core, whilst at the same time a beam waist of ~90μm in the unguided plane was produced approximately 5mm inside the 10mm long structure. As illustrated in Figure 4-7, a plano-convex cylindrical lens of focal length, f_x = 60mm, positioned 240mm from the diode module focussed the in-plane axis before a spherical diode collimating module of focal length f = 6.5mm, positioned 100mm further

on. As such, an elliptical beam was produced at the end face of the waveguide, with $1/e^2$ second-moment radii of 15 x 185 μm^2 in the y and x planes respectively. The beam quality in the plane was degraded to $M_x^2 \approx 25$ using this coupling scheme.

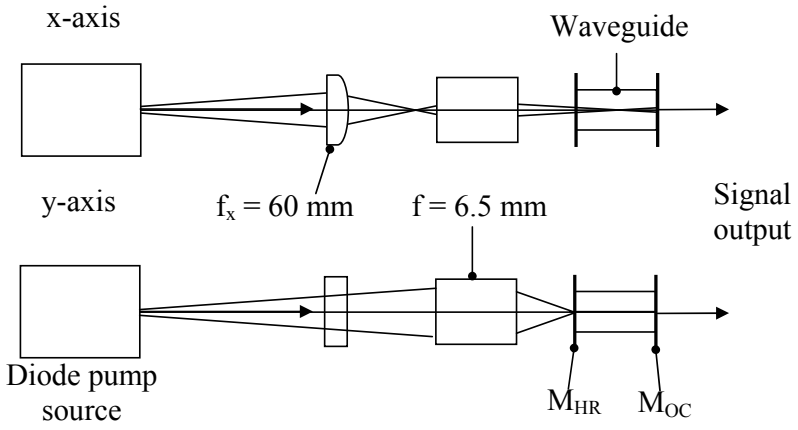

Figure 4-7: Diode coupling scheme for Nd:YAG PQS LMA PW laser.

The waveguide was mounted on a precision 6-axis translation stage for easy positioning with respect to the focus of the pump beam. It should be noted that the waveguide was simply fixed to a copper block with thermally conductive adhesive but not actively cooled. Thin lightweight mirrors (M_{HR}, M_{OC}), coated on one side only, and were attached to the waveguide end faces via the surface tension of a thin layer of fluorinated liquid, thus forming a quasi-monolithic flat-flat laser cavity of 10 mm length.

4.4.3 Laser performance

The laser output power at 1.064 μm for two values of output coupler reflectance is shown in Figure 4-8(a), along with the respective pulse repetition frequency in Figure 4-8(b). Although the average power appears to continue in a linear fashion for pulse repetition rates exceeding ~80kHz, the pulses were observed to collapse into a quasi-CW continuum. An example pulse shape is shown in Figure 4-9(a), with a corresponding pulse train, Figure 4-9(b), illustrating the pulse to pulse energy fluctuations for a pulse repetition frequency of ~65kHz. As mentioned previously, this behaviour is attributed to the pulse to pulse period approaching the recovery time of the Cr^{4+} ions [30]

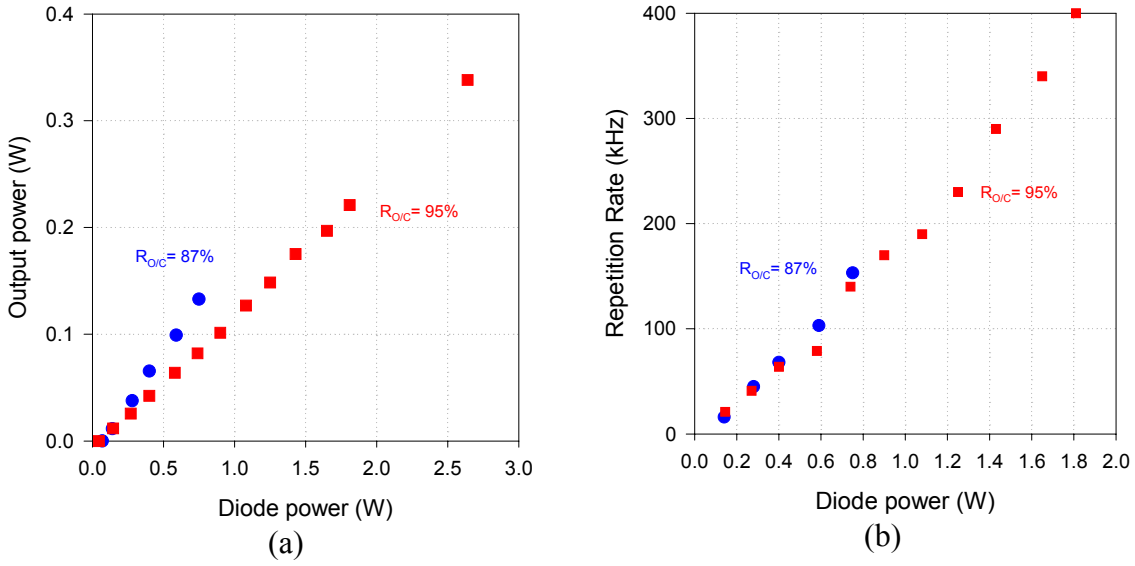

Figure 4-8: (a) Average output power and (b) pulse repetition frequency for two different output coupler mirrors.

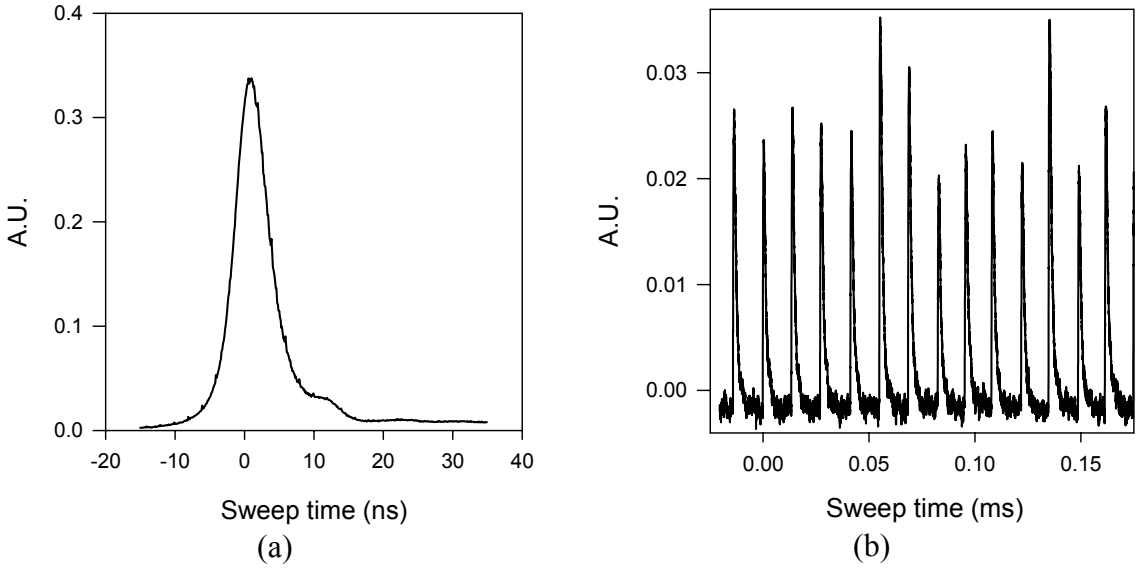

Figure 4-9: (a) Example of the pulse shape for operation at 1064 nm with an output coupling of ~5%. (b) Illustrates a pulse train for the same conditions as in (a).

Although laser operation at 946nm was also obtained with ~60mW of average output power for ~1.4W of pump power, considerable ASE was found at 1.064µm, a consequence of the relatively high threshold and initial gains. Double-pulsing was also observed, as illustrated in Figure 4-10. Nevertheless, for an output coupling of ~13% the

pulse to pulse stability was improved with respect to the 1.064 μm operation and the repetition rate was measured to be <10kHz, well within the response time of Cr^{4+}.

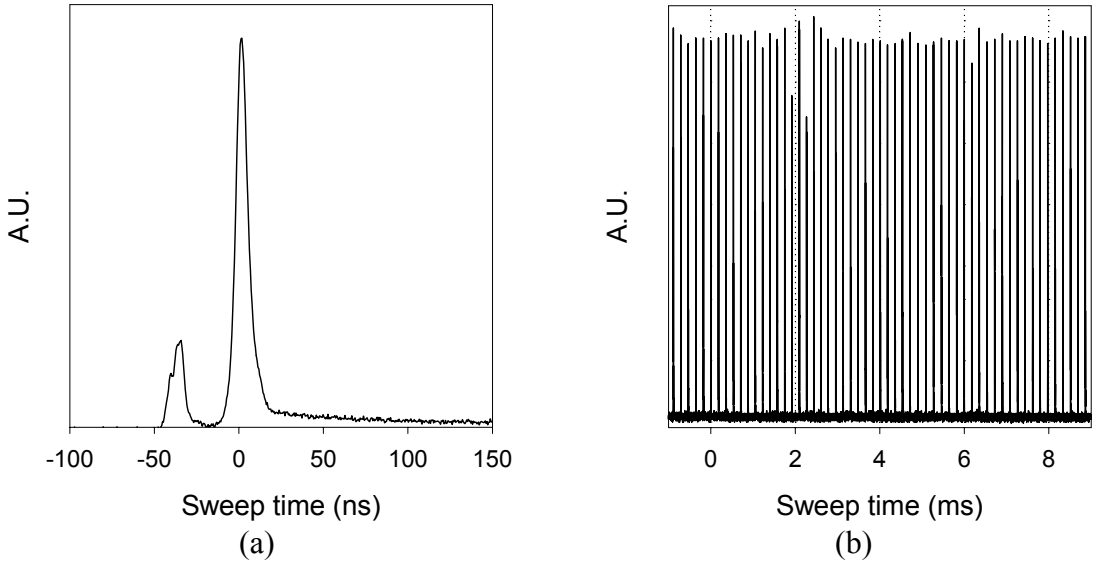

Figure 4-10: (a) Double-pulsing evident with higher output coupling, $R_{o/c}$ = 87%. (b) Pulse energy stability improved with respect to lower output coupling.

4.4.4 Discussion

The output performance was modelled as for the Yb:YAG device detailed in the previous section. A close match with the pulsewidth (~4-10ns) and repetition frequency (from 10 to >300kHz) could be obtained. In so doing a ~20% decrease in the SA ground-state absorption cross section was required with respect to that determined for the Yb:YAG LMA PW laser. Such a difference is expected noting the absorption spectra for Cr^{4+}:YAG reported by Dong *et al.* [19] (see inset Figure 4-2), where it is illustrated that at a wavelength of 1.03μm there is an increase of this magnitude in the maximum absorption coefficient, hence σ_q, with respect to that at 1.064μm. However, the difference for σ_q^{ESA} between these wavelengths was not reported and therefore kept constant between the two models. Similarly, for PQS operation at a laser wavelength of 946nm there is a further decrease in SA small-signal absorption of ~7% with respect to that at 1.064μm.

For 1.064μm operation the output was very unstable in terms of repetition rate, pulse energy, and double-pulsing. This unstable behaviour is thought to be due to the fact that the repetition rate is >100kHz soon after onset of laser operation. Modelling the Nd:YAG PQS PW lasers suggests that even with very high values of small-signal Cr^{4+} absorption it

would be difficult to achieve repetition rates below 100kHz in the end-pumped configuration and with the pump powers of interest here. Similarly, due to the short energy storage time of the Nd^{3+} ions, lower pulse energies than would be correspondingly found with Yb:YAG are expected. It appears that the high repetition frequency is primarily driven by the small mode-area associated with the waveguide geometry, thus making it an unsuitable configuration for passively Q-switching Nd:YAG. Larger mode volumes however, such as in a diode-bar side-pumped waveguide [30], will allow such operation.

4.5 Summary

Detailed in this chapter were the first demonstrations of passively Q-switched end-pumped large-mode-area planar waveguide lasers. An efficient, near-diffraction-limited Yb:YAG LMA PW laser produced 2.3W of average power, with 30μJ pulses and pulsewidths of 1.6ns, at repetition rates of up to almost 80kHz. These simple and compact devices and the associated high peak-powers, almost 20kW, could have a future in materials processing applications.

An end-pumped Neodymium-doped passively Q-switched planar waveguide laser was also demonstrated, although with inferior performance in comparison to its Ytterbium counterpart. Laser performance at 946nm on the quasi-three level $^4F_{11/2} \rightarrow {}^4F_{9/2}$ transition was obtained. However, a high threshold condition led to significant ASE at the stronger 1.064μm transition and a subsequent saturation of the available gain with reduced output performance.

Modelling of the laser performance using a simple plane-wave analysis predicts that although the end-pumped waveguide configuration is unsuited to Nd^{3+} active ions, Yb^{3+}-doping could be used to generate peak powers approaching the MW regime – materials permitting. This compares favourably with microchip laser technology that can produce a peak power of ~0.6MW using a 10.5mm long cavity length pumped by a fibre-coupled diode array delivering 12W of power [2]. It appears that the optical to optical efficiency for this result was ~3%, thus a comparable Yb:YAG LMA PW laser appears capable of generating the similar peak powers from a equally compact and robust device, with an almost tenfold improvement in efficiency.

4.6 References

[1] J. J. Zayhowski, "Passively Q-switched Nd:YAG microchip lasers and applications," *Journal of Alloys and Compounds*, vol. 303, pp. 393-400, 2000.

[2] J. J. Zayhowski, "Microchip lasers," *Optical Materials*, vol. 11, pp. 255-267, 1999.

[3] J. J. Zayhowski and C. Dill, "Diode-Pumped Passively Q-Switched Picosecond Microchip Lasers," *Optics Letters*, vol. 19, pp. 1427-1429, 1994.

[4] W. Koechner, *Solid State Laser Engineering - Chapter 1*, vol. 1, 4th ed. Berlin Heidelberg: Springer Verlag, 1999.

[5] B. E. A. Saleh and M. C. Teich, *Fundamentals of Photonics - Chapter 14*, 1st ed. New York: Wiley, 1991.

[6] A. E. Siegmann, *Lasers - Chapter 26*, 1st ed. New York: University Science Books, 1986.

[7] W. Koechner, *Solid State Laser Engineering - Chapter 3*, vol. 1, 4th ed. Berlin Heidelberg: Springer Verlag, 1999.

[8] N. D. Lai, M. Brunel, F. Bretenaker, and A. Le Floch, "Stabilization of the repetition rate of passively Q-switched diode-pumped solid-state lasers," *Applied Physics Letters*, vol. 79, pp. 1073-1075, 2001.

[9] J. B. Khurgin, F. Jin, G. Solyar, C. C. Wang, and S. Trivedi, "Cost-effective low timing jitter passively Q-switched diode- pumped solid-state laser with composite pumping pulses," *Applied Optics*, vol. 41, pp. 1095-1097, 2002.

[10] G. Youxi, Y. Guangtao, J. Tiangla, G. Yeuying, L. Xiangheng, and Z. Lanmin, "Growth of specially doped YAG laser crystal and its multifunction properties," *Conference on Lasers and Electro-Optics Proceedings 1984*, 1984.

[11] E. V. Zharikov, A. M. Zabaznov, A. M. Prokhorov, A. P. Shkadarevich, and I. A. Shcherbakov, "Use of GSGG:Cr,Nd crystals with centres as active elements in solid-state lasers," *Kvantovaya Elektronika*, vol. 13, pp. 2348-2349, 1986.

[12] A. A. Danilov, V. L. Evstigneev, N. N. Ilichev, A. A. Malyutin, M. Y. Nikolskii, A. F. Umyskov, and I. A. Shcherbakov, "A Compact Passively Q-Switched GSGG-Cr-$^{3+}$,Nd-$^{3+}$ Laser," *Kvantovaya Elektronika*, vol. 14, pp. 905-906, 1987.

[13] A. D. Gondra, V. M. Gradov, A. A. Danilov, V. V. Dybko, E. V. Zharikov, B. A. Konstantinov, M. Y. Nikolskii, Y. I. Rogalskii, S. A. Smotryaev, Y. I. Terentev, A. A. Shcherbakov, and I. A. Shcherbakov, "A Q-Switched GSGG-Cr, Nd Laser with an Efficient Pumping System," *Kvantovaya Elektronika*, vol. 14, pp. 916-917, 1987.

[14] S. Q. Li, S. H. Zhou, P. Wang, Y. C. Chen, and K. K. Lee, "Self-Q-Switched Diode-End-Pumped Cr,Nd-YAG Laser with Polarized Output," *Optics Letters*, vol. 18, pp. 203-204, 1993.

[15] S. H. Zhou, K. K. Lee, Y. C. Chen, and S. Q. Li, "Monolithic Self-Q-Switched Cr,Nd-YAG Laser," *Optics Letters*, vol. 18, pp. 511-512, 1993.

[16] P. Yankov, "Cr^{4+}YAG Q-Switching of Nd-Host Laser-Oscillators," *Journal of Physics D-Applied Physics*, vol. 27, pp. 1118-1120, 1994.

[17] G. H. Xiao, J. H. Lim, S. Yang, E. V. Stryland, M. Bass, and L. Weichman, "Z-scan measurement of the ground and excited state absorption cross sections of Cr^{4+} in yttrium aluminum garnet," *IEEE Journal of Quantum Electronics*, vol. 35, pp. 1086-1091, 1999.

[18] G. H. Xiao and M. Bass, "A generalized model for passively Q-switched lasers including excited state absorption in the saturable absorber," *IEEE Journal of Quantum Electronics*, vol. 33, pp. 41-44, 1997.

[19] J. Dong, P. Z. Deng, and J. Xu, "Spectral and luminescence properties of Cr^{4+} and Yb^{3+} ions in yttrium aluminum garnet (YAG)," *Optical Materials*, vol. 14, pp. 109-113, 2000.
[20] J. J. Degnan, "Optimization of Passively Q-Switched Lasers," *IEEE Journal of Quantum Electronics*, vol. 31, pp. 1890-1901, 1995.
[21] F. D. Patel and R. J. Beach, "New formalism for the analysis of passively Q-switched laser systems," *IEEE Journal of Quantum Electronics*, vol. 37, pp. 707-715, 2001.
[22] R. J. Beach, "Optimization of Quasi-3 Level End-Pumped Q-Switched Lasers," *IEEE Journal of Quantum Electronics*, vol. 31, pp. 1606-1613, 1995.
[23] A. Szabo and R. A. Stein, "Theory of laser giant pulsing by a saturable absorber," *J. Appl. Phys.*, vol. 36, pp. 1562-1566, 1965.
[24] F. D. Patel, E. C. Honea, J. Speth, S. A. Payne, R. Hutcheson, and R. Equall, "Laser demonstration of $Yb_3Al_5O_{12}$ (YbAG) and materials properties of highly doped Yb:YAG," *IEEE Journal of Quantum Electronics*, vol. 37, pp. 135-144, 2001.
[25] H. W. Bruesselbach, D. S. Sumida, R. A. Reeder, and R. W. Byren, "Low-heat high-power scaling using InGaAs-diode-pumped Yb:YAG lasers," *IEEE Journal of Selected Topics in Quantum Electronics*, vol. 3, pp. 105-116, 1997.
[26] T. Y. Fan, "Optimizing the Efficiency and Stored Energy in Quasi-3-Level Lasers," *IEEE Journal of Quantum Electronics*, vol. 28, pp. 2692-2697, 1992.
[27] G. J. Spuhler, R. Paschotta, M. P. Kullberg, M. Graf, M. Moser, E. Mix, G. Huber, C. Harder, and U. Keller, "A passively Q-switched Yb : YAG microchip laser," *Applied Physics B-Lasers and Optics*, vol. 72, pp. 285-287, 2001.
[28] Y. Kalisky, C. Labbe, K. Waichman, L. Kravchik, U. Rachum, P. Deng, J. Xu, J. Dong, and W. Chen, "Passively Q-switched diode-pumped Yb : YAG laser using Cr^{4+}- doped garnets," *Optical Materials*, vol. 19, pp. 403-413, 2002.
[29] J. Dong, P. H. Deng, Y. P. Liu, Y. H. Zhang, J. Xu, W. Chen, and X. L. Xie, "Passively Q-switched Yb : YAG laser with Cr^{4+}:YAG as the saturable absorber," *Applied Optics*, vol. 40, pp. 4303-4307, 2001.
[30] R. J. Beach, S. C. Mitchell, H. E. Meissner, O. R. Meissner, W. F. Krupke, J. M. McMahon, W. J. Bennett, and D. P. Shepherd, "Continuous-wave and passively Q-switched cladding-pumped planar waveguide lasers," *Optics Letters*, vol. 26, pp. 881-883, 2001.
[31] A. A. Lagatsky, A. Abdolvand, and N. V. Kuleshov, "Passive Q switching and self-frequency Raman conversion in a diode-pumped Yb:$KGd(WO_4)_2$ laser," *Optics Letters*, vol. 25, pp. 616-618, 2000.

Chapter 5

SIDE-PUMPED WAVEGUIDE LASERS

5.1 Introduction

Increasing the power of solid-state lasers while maintaining good beam quality and hence high-brightness, requires the use of high-power pump sources that also minimise the detrimental effects associated with waste heat. Laser diode bars, which have a reasonable spectral brightness and can provide >60W of CW power from an emission area of ~ 1 x 10 000μm^2, are well suited to this requirement. Efficient transfer of the pump power from such a diode bar to the oscillating laser mode typically requires some degree of beam conditioning, the extent of which depends upon the resonator geometry. As mentioned in the introductory Chapter, the diode laser geometry closely matches that of the planar waveguide, allowing simple and efficient launching of its pump power.

The pumping configuration investigated in this Chapter involves coupling of the diode radiation into the waveguide transverse to the direction of laser propagation, i.e. side-pumping. Although less intense than end-pumping, side-pumping in combination with the planar waveguide structure can still generate high inversion densities suitable for quasi-three-level transitions [1]. This is especially important in high-power applications that have been increasingly turning toward alternatives to Nd^{3+} doped active materials, such as Yb^{3+}, or even Tm^{3+} for wavelengths in the 2 micron region, both of which exhibit quasi-three-level properties. Thus, with a single diode bar, pump intensities greater than 10kWcm^{-2} (10W into a 1cm-long, 10μm-thick waveguide) may be delivered to the active medium. This is comparable to the saturation intensity for the rare-earth ions in a YAG host considered here.

Other benefits for high-power laser systems associated with side-pumping active LMA PW's are: the creation of a uniform gain profile perpendicular to the layers; a large ratio between the cooled-surface area and active medium thickness, important for reducing

thermal distortions that perturb beam quality and can lead to fracture of the host medium [2]; and lastly, three independent axes for the primary parameters of high-average-power solid-state laser systems, i.e. the excitation, the waste heat removal, and the laser output.

The rest of this Chapter is organised as follows: the diode to waveguide coupling techniques employed in the experiments detailed are reviewed, whence a multimode Tm:YAG LMA PW laser is described, its performance characterised and a plane-wave energetics model, as detailed in Chapter 2, applied. In addition, results obtained from experiments investigating Nd:YAG LMA PW lasers are reported. The first is a monolithic unstable resonator and is followed by an extended cavity configuration, both attempting to improve the beam quality in the unguided axis.

5.2 Diode coupling to large mode area planar waveguides

5.2.1 Introduction

Several methods for transforming the output characteristics of diode laser bars exist, for example beam-shaping [3], diffractive elements [4], and step-mirrors [5]. Each of these techniques equalise the divergence in the two axes defined by the diode bar, and possess varying degrees of transfer efficiency. In contrast, the compatible geometry of the planar waveguide with that of the high-power diode bar negates the requirement for beam shaping, allowing simple and compact coupling schemes. Discussed in the following sections are two methods utilised for coupling the radiation of a diode bar into the core of a double-clad high-numerical aperture waveguide.

5.2.2 Proximity coupling

The waveguide design and the proximity coupling of a single diode bar to the double-clad structure are shown schematically in Figure 5-1. In the experiments described here, the double-clad waveguide can be pumped from one or both sides by diodes with a typical full-width half-maximum divergence, θ_{FWHM}, of 35° in the fast axis. Assuming a diffraction-limited Gaussian output beam from the diode in this axis, and an anti-reflection (AR) coated input face, we can make an estimate of the delivery efficiency into the central YAG layers using,

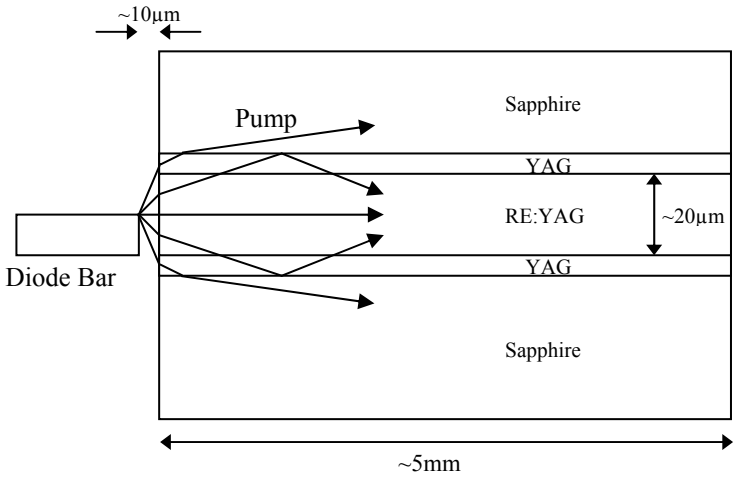

Figure 5-1: Schematic diagram of proximity-coupling a diode bar to a rare earth (RE) doped LMA double-clad waveguide

$$\eta_{del} = \frac{\int_{-\min\left(\vartheta_{inc},\sin^{-1}(NA)\right)}^{\min\left(\vartheta_{inc},\sin^{-1}(NA)\right)} \exp\left[-\ln(16)\left(\frac{\theta}{\theta_{FWHM}}\right)^2\right] d\theta}{\int_{-90}^{90} \exp\left[-\ln(16)\left(\frac{\theta}{\theta_{FWHM}}\right)^2\right] d\theta} \qquad \textbf{(5.1)}$$

where θ is the angle of propagation (in degrees) of the divergent diode beam with respect to the axis of the planar waveguide. If the half-angle subtended by the YAG central layers to the diode emission aperture, θ_{inc}, is smaller than the angular acceptance of the waveguide, $\sin^{-1}(NA)$, then equation (5.1) describes the overlap of the diverging pump beam with the physical aperture of the YAG central layers. Any light incident on the waveguide outside this aperture is not totally internally reflected. If the angular acceptance of the waveguide is less than θ_{inc} then equation (5.1) describes the fraction of the diverging pump beam that is contained by the numerical aperture of the YAG/sapphire waveguide. In our experimental set up (θ_{inc}=56°, NA=0.47) it is the latter condition that applies. Equation (5.1) will slightly underestimate the delivery efficiency due to the fact that pump light propagating at angles larger than the waveguide NA is not totally lost, as partial reflection will still occur at each bounce from the YAG/sapphire interface. A very small contribution would also be made to the absorbed power by light reflecting from the upper sapphire/air interface.

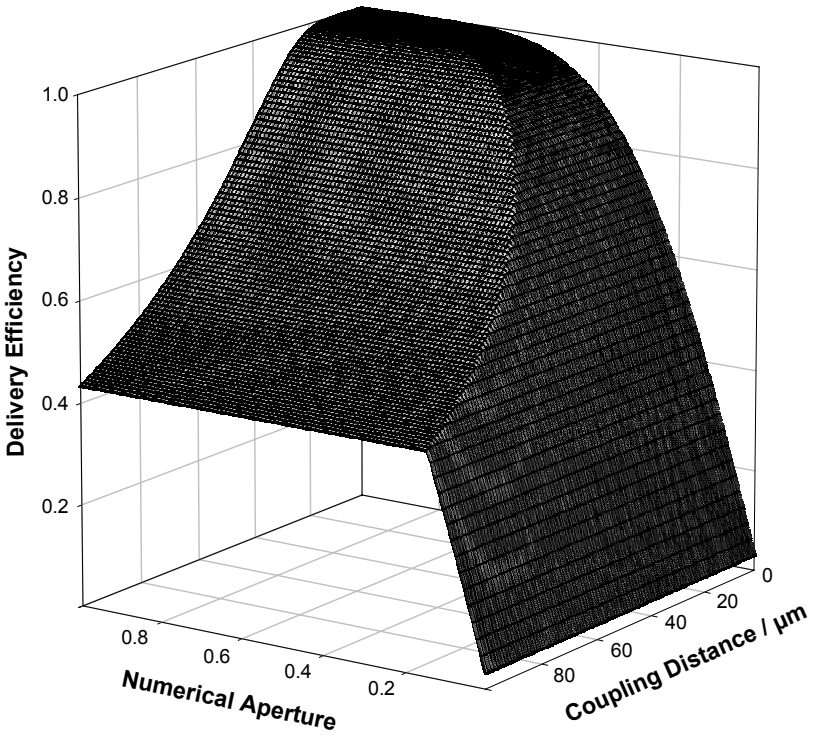

Figure 5-2: Delivery efficiency against coupling distance and waveguide numerical aperture for a waveguide aperture of 30μm.

Figure 5-2 shows how the delivery efficiency varies with diode coupling distance and the waveguide *NA*. It can be seen that the delivery efficiency saturates as the *NA* is increased for a given coupling distance, and as the coupling distance is reduced for a given *NA*. It also shows, that for the particular values of diode beam divergence and waveguide dimensions used here, the coupling efficiency approaches 100% when the coupling distance is <20μm and the numerical apertures is >0.6. A delivery efficiency of 0.942 is calculated for our combination of coupling distance (10μm) and *NA* (0.47).

Figure 5-3 shows the results of beam propagation method (BPM) modelling, using a commercial software package from Kymata Software, of the calculated pump intensity at the other side of the waveguide (assuming no absorption and infinitely thick sapphire layers), which shows how the remaining ~5% of the pump light is lost to radiation modes. The real value of the delivery efficiency may vary from this figure due to non-diffraction-limited beam quality from the diode, reflections from the AR coating, and (as previously discussed) reflection of power beyond the *NA* of the waveguide. Nevertheless, it is clear that this is a very compact and efficient method of pump delivery.

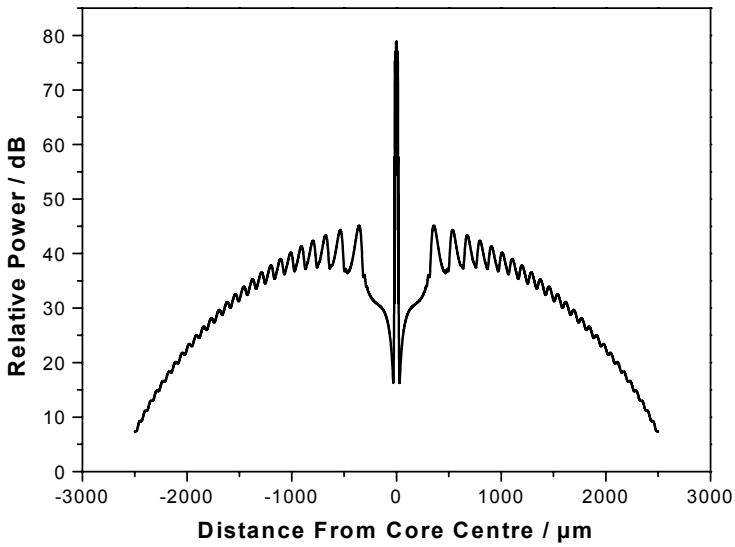

Figure 5-3: Calculated pump power distribution at the end of the waveguide assuming no absorption (NB logarithmic scale).

5.2.3 Lens coupling

Another technique to couple the pump radiation from a diode bar into a planar waveguide is to condition the beam with cylindrical optics such that an image of the bar is positioned at the entrance to the waveguide. There are some minor drawbacks with this technique, the main being that the beam quality of the fast axis of the diode bar is typically degraded when collimating the beam, a consequence of its high divergence and the opto-mechanical alignment tolerances. Consequently the resulting image is generally degraded; however in the experiments reported here this is acceptable and easily captured by the large waveguide aperture. A second disadvantage is the increased space and optical complexity, in comparison with proximity coupling, required to launch the pump light. Finally launching the pump in this fashion requires clear side faces, which is not compatible with one method for suppressing parasitic lasing paths, as detailed later, where the side face is grooved matching the diode bar emitter pitch.

The advantage of this technique is that diode-bar arrays (i.e. diode-stacks) are also compatible, which is not the case with proximity-coupling. It therefore represents a robust method for power scaling side-pumped LMA PW lasers and will be discussed in the future works section of Chapter 6.

5.3 Tm:YAG large mode area planar waveguide laser

5.3.1 Introduction

High power lasers around 2μm are of interest for several applications due to the strong absorption by water and human tissue, low atmospheric absorption, and eye-safe properties of light in this wavelength region. Operation of Tm:YAG on the $^3F_4 \rightarrow {}^3H_6$ transition is an attractive system for such lasers as it allows pumping by AlGaAs diodes around 0.8μm, while maintaining high efficiency and low thermal loading. This is possible, despite the large difference between the pump and laser photon energies, because of a favourable cross-relaxation process that leads to a pumping quantum efficiency approaching 2. The disadvantages of the Tm^{3+} system include its quasi-three-level nature, the presence of energy-transfer upconversion, and a relatively low emission cross-section.

End- and side-pumped bulk Tm:YAG lasers have been reported at continuous-wave (CW) powers of >100W using lens ducts [6] and parabolic concentrators [7] to achieve the required intense pumping density. Waveguide geometries have also been used for 2μm laser systems both in planar [8] and fibre [9] format. Reported here is a double-clad Tm:YAG planar waveguide that delivers 15W output at 2μm when side-pumped by two 20W diode bars. A model of the performance of this laser is also presented, including the delivery and absorption of the pump power and the expected thermal load, in order to investigate its potential for power scaling.

5.3.2 Experimental set-up and performance

The direct-bonded LMA double-clad planar waveguide structure detailed here and shown in Figure 5-4, is similar to those described previously with Nd^{3+}- and Yb^{3+}-doped YAG [10, 11]. A 20μm-thick 10at.%-Tm^{3+}-doped YAG core, was direct bonded between two 5μm thick un-doped YAG inner cladding layers. Sapphire substrates were also direct bonded to form the outer cladding layers. The width and length dimensions were 0.5cm and 1cm respectively. Laser cavity mirrors were coated directly onto the flat end-faces of the waveguide with an output coupler transmission of 10% at 2.02μm. The side-faces of the waveguide were tilted by ~3° (with respect to the vertical axis) to frustrate parasitic lasing in the plane of the waveguide. They were also anti-reflection coated at the pump wavelength.

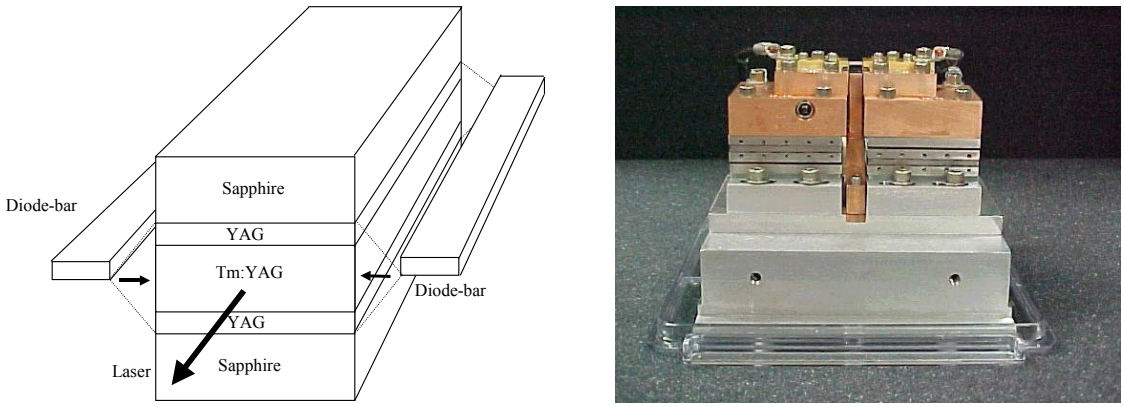

Figure 5-4: (a) Schematic diagram of the experimental set-up and the 5 layer waveguide structure. (b) Picture of the proximity coupled set up, photo courtesy of Maxios Laser Corporation.

Two CW diodes from Coherent Inc[xxv]. were proximity coupled to the waveguide on custom alignment fixtures from Maxios Laser Corporation[xxvi], Figure 5-4(b). These diodes had a centre wavelength of 785nm and produced up to 44W of combined power. They were water-cooled, along with the waveguide mount, through a common base plate. Laser threshold was found at 8W incident pump power. The resulting maximum output power was 15W, corresponding to an optical to optical efficiency of 34%, and with a measured slope efficiency of 44% with respect to incident power.

Single-pass absorption of the diode pump radiation was measured to be 71%, under single-side pumping and lasing conditions; therefore the slope efficiency with respect to absorbed power was ~61%. Figure 5-5 shows the results for both double-sided and single-sided pumping with the main difference being a slightly higher threshold for the single-sided pumping case. The gain distribution in the unguided plane is expected to be relatively uniform with double-sided pumping, while the single-sided pumping has much stronger gain closest to the pumped face corresponding to the effective absorption measured here. The intensity profiles of the laser output in the guided and unguided axes were measured by scanning a 250μm square InAs PIN photodiode across the beam, whilst monitoring its amplified voltage output. Single traces of the intensity profile at the beam

[xxv] Coherent Inc., Santa Clara, CA 95054 USA

[xxvi] c/o- Onyx Optics, Dublin, CA 94568 USA

centre for the respective axes are shown in Figure 5-6. A comparison is made between the guided and unguided axes for single and double-sided pumping. It was observed that the guided modes were a very good fit to a Gaussian distribution and did not vary with power or the pumping scheme. In the non-guided plane the double-sided pumping lead to a symmetric near-Gaussian output, whereas the single-sided pumping gave an asymmetric mode with the peak intensity shifted towards the pumped side.

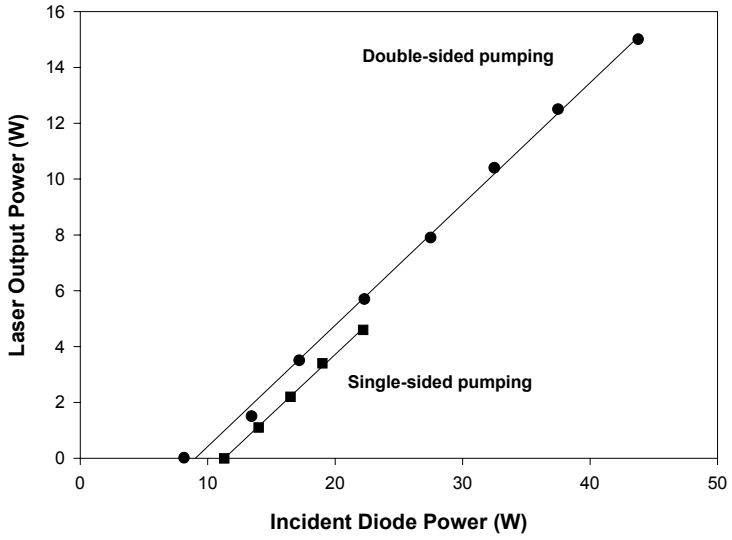

Figure 5-5: Tm:YAG LMA double-clad planar waveguide laser output power characteristics.

The beam dimensions were determined via a second-moments analysis. By tracing the beam as it propagated from the output and fitting the Gaussian propagation curve to the results, using the apertures of the waveguide and in-plane width to define the initial beam waists, it was found that the guided axis had an M^2=1.1±0.1, however for the unguided axis the M^2 was >300. As discussed in Chapter 2 the diffraction-limited nature of the output in the guided axis is due to the fact that the gain is restricted to the core and selects fundamental mode operation of the highly multi-mode double-clad waveguide (supporting 15 modes at 2μm). No attempt has been made to control the mode in the non-guided axis, which had a high cavity Fresnel number[xxvii] (>500) [12] due to the 10mm long and 5mm wide gain region.

[xxvii] Fresnel number, $N_F = w^2/2\lambda l$. Where w is the width of waveguide, l is its length, and λ the laser wavelength in the material.

It was observed that the laser output was partially polarised, with a ratio of 9:1 TE:TM polarisation. Although not confirmed experimentally, it is believed that this partial polarisation may be a consequence of stress birefringence from the direct bonding fabrication process.

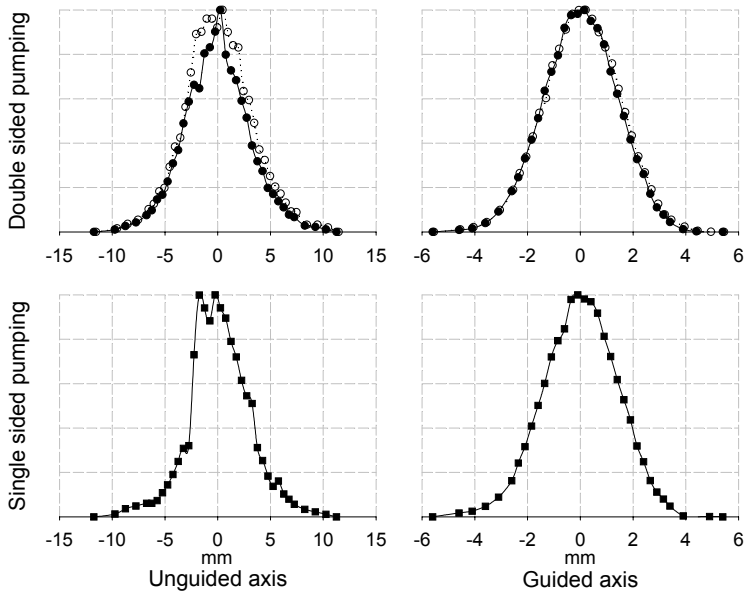

Figure 5-6: Beam profile scans 40mm from the cavity mirror. A comparison between double and single-sided pumping is made for both the guided and unguided axes. The profiles for the double-sided pumping at 15W (··o··) and 4W (-●-) output powers are shown. The latter power being the maximum achievable with single-sided pumping.

5.3.3 Modelling

5.3.3.1 Laser performance

The laser performance of the double-clad Tm:YAG waveguide shown in Figure 5-5, when pumped from both sides with two 20W diode bars, was compared to predictions using the plane-wave model described in Chapter 2. This model, modified to account for cross-relaxation and up-conversion in the Tm^{3+} system, is likely to be a good approximation due to the relatively uniform nature of the gain distribution and laser saturation, which is provided by the double-clad waveguide structure in one axis and the plane-wave nature of the highly multimode output in the other. For the 10at%-doped, 5mm-wide, double-clad waveguide and the R_l^{oc}=0.9 output coupler used in our experiments, the single-pass pump absorption (see Chapter 2) is calculated to be 0.73 (compared to a non-saturated

absorption of 0.756), in good agreement with experimental observation. Thus, the double-sided pumping will also give a relatively uniform gain profile in the non-guided plane (with a calculated 24% variation in the upper-laser-level population density across the width of the guide for the case of unsaturated pump absorption).

The Tm:YAG energy levels and the pumping, cross-relaxation, up-conversion and lasing processes are shown in Figure 5-7.

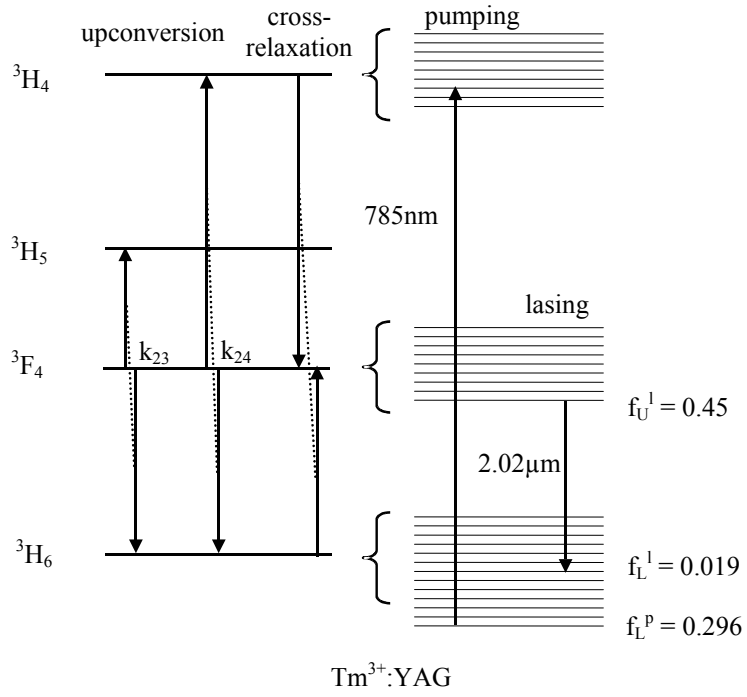

Figure 5-7: Schematic diagram of the Tm:YAG energy levels involved in the 2µm laser operation. Upconversion and cross-relaxation processes considered in the model are indicated on the left and the Boltzmann occupation factors of the relevant Stark levels at 306K are shown on the right.

Table 5-1 lists the parameters used to model the lasing performance. The quantum yield, which accounts for the cross relaxation process shown in Figure 5-7, is calculate to be 1.97 using the method presented by Honea *et al.* [6] and accounting for our doping level of 10 at.%. The mode fill efficiency is set at 1 as the laser mode is expected to efficiently sweep out the available gain. The emission and absorption cross-sections are set relative to the Boltzmann occupation factors [6, 13]. The overlap of the pump with the doped area was discussed in Chapter 2, and the overlap of the laser field with the doped area is calculated assuming that the laser operates on the fundamental guided mode (as found

experimentally). The Boltzmann factors are calculated using the Stark splittings reported by Gruber *et al.* [14], and assuming an average operating temperature of 306K and that the lifetime of $^3H_4$<<$^3F_4$.

Quantum yield	η_{QY}	1.97
Mode fill efficiency	η_{Mode}	1
Delivery efficiency	η_{del}	0.94
Pump 785nm photon energy	$h\nu_p$	$2.5\text{x}10^{-19}$ J
Laser 2.02μm photon energy	$h\nu_l$	$9.8\text{x}10^{-20}$ J
Output Coupler Reflectivity	R_l^{oc}	0.9
Pump absorption cross-section	σ_p	$1.0\text{x}10^{-24}$ m^2
Pump overlap with doped region	η_{po}	0.68
Laser emission cross-section	σ_l	$3.3\text{x}10^{-25}$ m^2
Laser overlap with doped region	η_{lo}	0.96
One-way waveguide transmission	T_{sp}	0.99
Effective excited state storage lifetime	τ_{eff}	$2.1\text{x}10^{-3}$ s
Waveguide length	l	$1\text{x}10^{-2}$ m
Waveguide width	w	$5\text{x}10^{-3}$ m
Doped core thickness	t_{core}	$20\text{x}10^{-6}$ m
Tm doping density	n_o	$1.38\text{x}10^{27}$ m^{-3}
Terminal laser Stark level Boltzmann occupation factor at 306K	f_L^l	0.019
Initial laser Stark level Boltzmann occupation factor at 306K	f_U^l	0.451
Initial pump Stark level Boltzmann occupation factor at 306K	f_L^p	0.296
Terminal pump Stark level Boltzmann occupation factor at 306K	f_U^p	0

Table 5-1: Laser Model Parameters

The values for the effective lifetime and waveguide transmission are found by fitting to the experimental laser performance (threshold and slope efficiency) shown in Figure 5-5. The effective lifetime of ~2.1ms is related to the low-excitation $^3F_4$ lifetime, τ_f=10.5ms, the upconversion rate coefficient, k_{uc}, and the population density of the upper laser manifold, N_U, by

$$\tau_{eff} = \frac{1}{\frac{1}{\tau_f} + k_{uc}\frac{N_U}{l}} \quad \textbf{(5.2).}$$

Here, k_{uc} represents an overall value accounting for both of the upconversion processes illustrated in Figure 5-7. Rustad and Stenersen [15] have shown that the overall upconversion rate is dominated by k_{23} and for which values were measured against doping level by Shaw *et al.* [16]. Fitting the model to the experimental results leads to a value $k_{uc}=3.9\pm0.5\text{x}10^{-24}\,m^3s^{-1}$, in good agreement with the published data at a doping level of 10at.%. The fitted one-way transmission corresponds to a propagation loss coefficient of 0.07±0.01dB/cm at 2.02μm. This is somewhat lower than the values found for similar Nd and Yb-doped double-clad waveguides [11], (<0.2dB/cm) and is approaching reported values at 1μm for bulk Nd:YAG rods [17] (0.03dB/cm). The good fit to the experimental data, Figure 5-8, using very reasonable parameter values, allows predictions to be made for optimisation and power scaling of this system with some confidence.

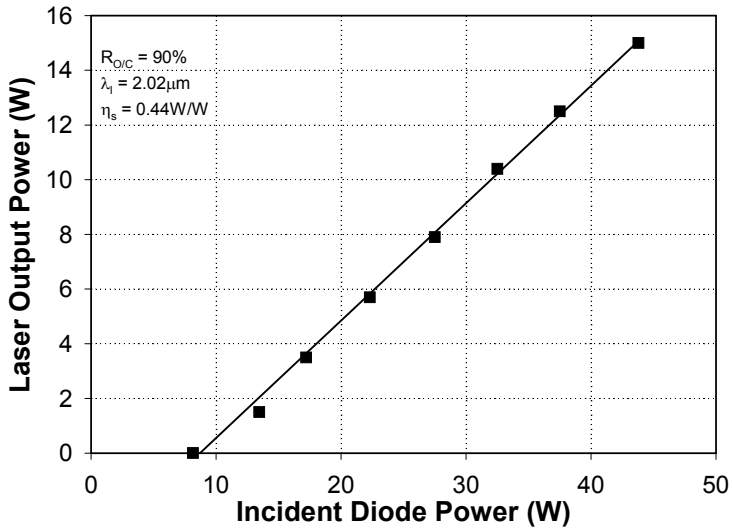

Figure 5-8: Modelling fit to experimental data, with variables $k_{uc}=3.9\pm0.5\text{x}10^{-24}m^3s^{-1}$ and the propagation loss = 0.07±0.01dB/cm.

5.3.3.2 Output channels for the absorbed power

The model allows for easy identification of the routing of the absorbed pump power into the various possible output channels. Here, the output channels are identified as; the output power calculated using equations (2.20)-(2.22), the fluorescence power,

$$P_{fl} = \frac{h\nu_l N_U}{\tau_f} wt_{core}$$

(5.3)

the upconversion power,

$$P_{uc} = h\nu_l N_U{}^2 k_{uc} \frac{wt_{core}}{l}$$

(5.4)

the quantum-defect (Q.D.) thermal power,

$$P_{therm} = \eta_{del} P_p \left(1 - e^{\eta_{op}\sigma_p N_U^p}\right)\left(1 - \frac{\eta_{QY}\nu_l}{\nu_p}\right)$$

(5.5)

and the power loss,

$$P_{loss} = P_p \left(\frac{R_l^{oc}}{1 - R_l^{oc}}\right)\left(1 - T_{sp}^2\right) e^{\eta_{ol}\sigma_l N_L^l}$$

(5.6).

Figure 5-9 shows a plot of these various output channel powers against output coupling for the maximum experimental input power of 43.8W and a fixed temperature of 306K. The graph shows that the use of an R_l^{oc}=0.9 output coupler is near optimum for this pump power level and that the power going to heat at this point is nearly 7W. It should be noted that a certain fraction of the upconversion power would also be converted to heat due to non-radiative decay of the ions promoted into the $^3H_5$ level. However, at optimum output coupling this contribution to the total heating power is small compared to the quantum-defect thermal power given in equation (5.5), and has been neglected in the thermal calculations. It can also be seen that the range of output coupling, and hence the achievable gain, is limited due to upconversion becoming the dominant output channel for the absorbed pump power. This is confirmed by Figure 5-10 where the theoretical output power is plotted against output coupling for various values of the upconversion rate coefficient. Experimental observations that lasing was not obtainable with a 50% output coupler is therefore attributed to the presence of upconversion. Similar effects due to energy-transfer upconversion have also recently been described in CW Nd^{3+}-doped lasers [18]. The main reason for the drop in output power at low reflectivity for the case where no upconversion is present is depletion of the ground state, leading to a smaller absorption efficiency.

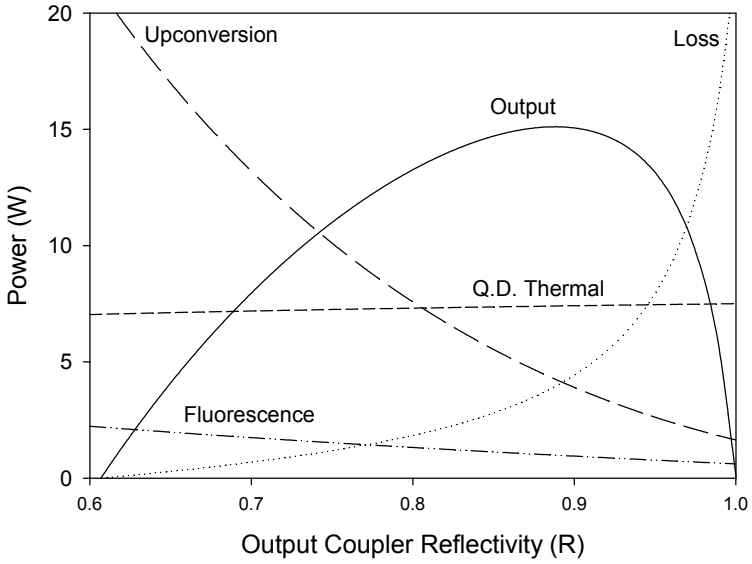

Figure 5-9: Output channels for the input power against output coupler reflectivity for the maximum pump power of 43.8W and at a fixed temperature of 306K.

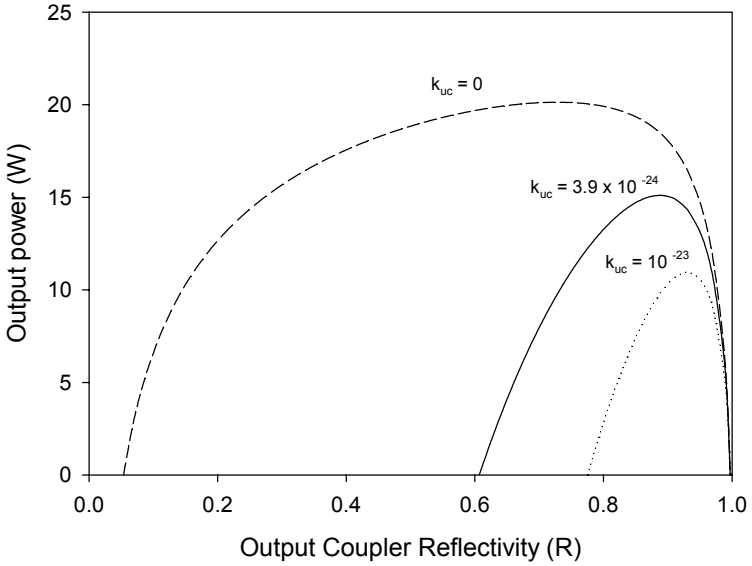

Figure 5-10: Output power against output coupler reflectivity for various values of upconversion rate coefficient k_{uc} (in m^3s^{-1}).

5.3.3.3 Optimisation of doping level

At this point it is interesting to consider what is the optimum Tm-doping level. If it is increased from the current 10at.% doping level the width of the guide should be decreased in order to maintain the same fractional power absorption and hence the relatively uniform gain distribution. Reducing the width would also help to decrease the Fresnel number of the cavity and hence improve the M^2 of the output in the non-guided plane. However, this would bring with it a penalty in terms of an increased upconversion coefficient [16] and a

greater thermal load per unit volume. Consequently, a drop in output power of nearly 1W is expected by going to a 15at.% doping level. If the doping level is reduced from 10at.% the width of the guide must increase to maintain the same pump absorption, which in turn would adversely effect the output M^2 value. An initially very slight reduction in the quantum yield would also occur but it is nevertheless expected to increase the output power, due to reduced upconversion and thermal load, of ~0.5W by going to a 5at.% doping level.

The value for the thermal load per unit volume (Q_T) used in this model is based on a thermal power of 3.4W. This is chosen to calculate the temperature used in the laser model (306K) as an average figure between zero and full pumping power, when 6.8W of Q.D. thermal power is predicted. The temperature in the core is predicted to be ~324K (51ºC) at full pump power. It should be made clear that the cooling arrangement and the waveguide structure are not optimised in terms of minimising the temperature rise. For instance, with both faces heat-sunk and the use of 100µm-thick substrate and cladding layers, which would still give a robust and easy to handle device, the temperature at maximum pump power is only 28ºC, for a heat sink temperature of 16ºC.

As discussed in Chapter 2 planar waveguide lasers have been shown to exhibit similarly good thermal management properties to bulk slab lasers [2]. Based on the theory of Chapter 2 section 2.3.2, the temperature rise in the double-clad structure described and its implications for power scaling to the 100W level can now be discussed. The waveguide architecture investigated is shown in Figure 5-11 and using the parameters listed in Table 5-2 the model gives a temperature distribution near the core as shown in Figure 5-12. Note the upper surface was not actively cooled; therefore an equivalent heat transfer coefficient, λ_a, to ambient air was used instead.

Air temperature	T_a	293 K
Heat sink temperature	T_{hs}	289 K
Air heat transfer coefficient	λ_a	10 $Wm^{-2}K^{-1}$
Water-cooled heat sink heat transfer coefficient	λ_{hs}	6000 $Wm^{-2}K^{-1}$
Thermal conductivity of YAG	k_y	13 $Wm^{-1}K^{-1}$
Thermal conductivity of sapphire	k_s	35 $Wm^{-1}K^{-1}$
Thermal power loading per unit volume	Q_T	$3.4x10^9$ Wm^{-3}

Table 5-2: Thermal model parameters – as detailed in Figure 5-11.

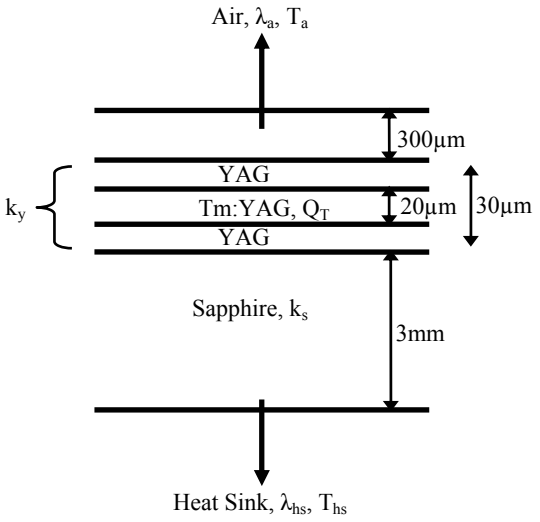

Figure 5-11: One-dimensional-cooling model structure

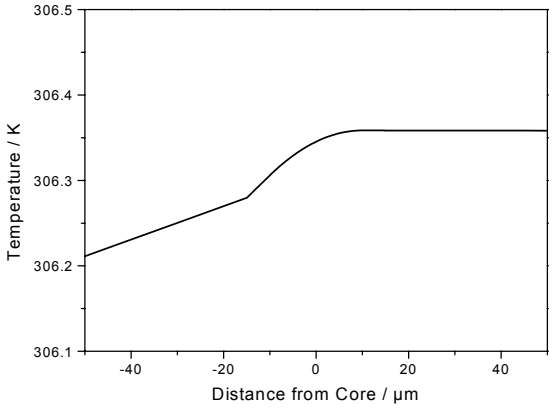

Figure 5-12: Temperature distribution near the waveguide core

At this point it is useful to enquire into the power scalability of such a device. The relatively simple thermal analysis suggests that, with the current heat load and the use of a thin, double-face-cooled waveguide described above, we would be three orders of magnitude below the surface stress fracture limit. This is calculated via a figure of merit obtained using equation (2.40) with the thermal shock parameter, R_s, for sapphire equal to $100 Wcm^{-1}$[19].

For the bonded waveguides described here, the different thermal expansion coefficients of the YAG and sapphire layers is a potential limitation but, in practice, they can clearly survive high temperatures as part of the fabrication process involves annealing the structure at a few hundred degrees. Thus, the main thermal limitation for quasi-three-level lasers will be degradation in the laser performance due to increased population in the lower laser levels. As an example, Figure 5-13 shows the expected laser performance for a range of temperatures.

The simplest scaling from the present results could be obtained by replacing the two 20W diodes with two 60W diodes, which are readily available with similar emission apertures. For the thin, double-face-cooled, waveguide this would give a maximum temperature of 321K and an expected output power of 50W for an output coupler of R_l^{oc}=0.87. Scaling from this point, without increasing the thermal load per unit volume, and hence the temperature rise, could be achieved through increasing the length of the crystal and adding

more diode pumps. Figure 5-14 gives the expected laser performance for a 2cm long device, side-pumped by four 60W diodes, approaching 100W of output power for an R_l^{oc}=0.7 output coupler.

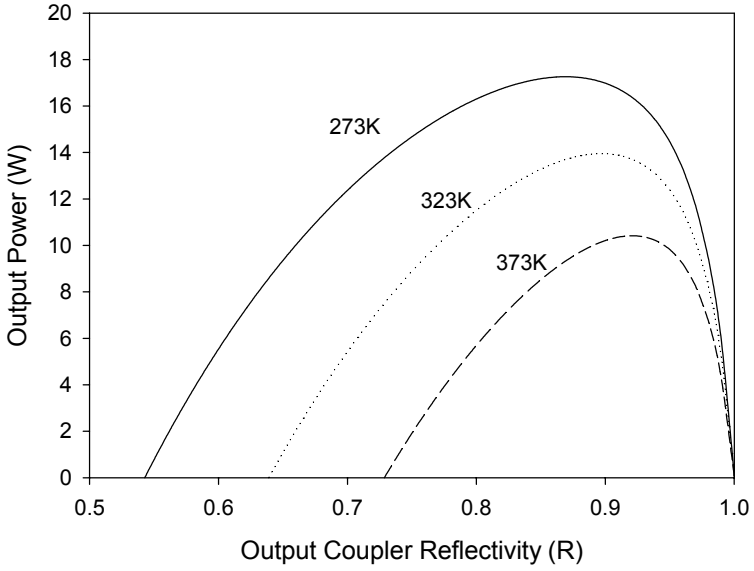

Figure 5-13: Output power against output coupler reflectivity for various core temperatures.

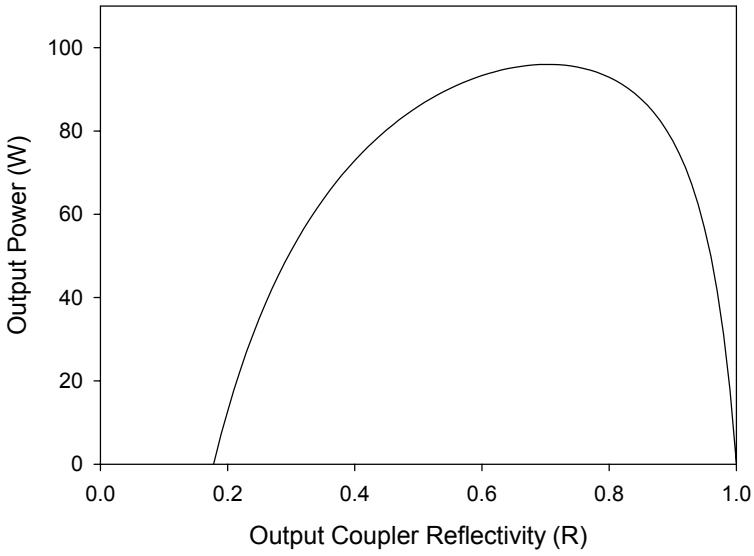

Figure 5-14: Theoretical plot of output power against output coupler reflectivity for four 60W diode pump lasers.

The output characteristics of the investigated waveguide have important implications for which method could be used to control the spatial properties of the laser in the non-guided plane. Typically, the combination of side-pumping with the plane/plane laser resonator used here leads to highly multi-mode output in the non-guided plane as shown above, [11]. As has been previously mentioned and proposed by Beach *et al.* [10], monolithic hybrid guided/unstable resonators could be a potential solution to this problem because of the high gains available from diode-pumped waveguide lasers. However, in the case of Tm:YAG, the fact that optimum output powers occur for relatively low output coupling, due to upconversion, means that the potential for use of unstable resonators will be limited. Fortunately though, the very low propagation loss found here suggests that zig-zag-path stable cavities [20] should be feasible, as will be discussed in the future works section.

5.4 Nd:YAG large mode area planar waveguide lasers

5.4.1 Introduction

Neodymium, especially in the host material YAG, has long been the workhorse of the solid-state laser field. Its characteristics have been well documented and yet each year new developments are made with this active material. Described in the following sections are some developments made with this laser crystal in the form of a side-pumped LMA planar waveguide structure. Firstly, due to the relatively high gains possible with this material, in particular in the waveguide geometry, it was discovered that ASE and parasitic lasing effects limited and in some cases defeated laser operation for the side-pumped configuration. Methods for reducing these effects are discussed in the next section, followed by a report of two different resonator geometries.

5.4.2 Frustrating amplified spontaneous emission and parasitic lasing

Parasitic lasing and ASE, two effects derived from spontaneous emission in all directions, are separate phenomena that affect the laser performance in different ways. ASE simply de-excites some of the population inversion thereby reducing the available gain for the resonator. Its effect can be relatively uniform across the excited volume, depending upon the physical attributes of the active material and resonator configuration. Conversely, parasitic lasing describes an unwanted resonant mode that exceeds a certain threshold, defined by the losses incurred for one round trip, which also clamps the inversion along

the path taken. In the waveguide structures described here these modes typically correspond to closed loops provided by total internal reflection within the short, yet wide, planar region, as illustrated in Figure 5-15. It should be noted that the single diamond (red loop) is not truly a TIR off the end faces, as the incident angle is less than the critical angle. However, there is still a substantial end-face Fresnel reflectance and a possible path for parasitic lasing. In fact the two examples illustrated in Figure 5-15 represent the limits to be expected from YAG/air interfaces with this geometry, the two diamond case (not shown) being well confined at both the side and end faces.

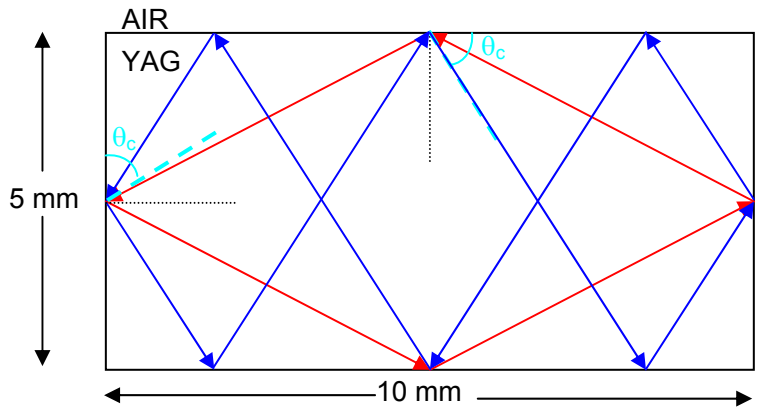

Figure 5-15: Illustration of the two limits for closed loops defined by TIR at the side and end faces of a YAG planar waveguide. θ_c is the critical angle ~33° for a YAG air interface.

Three different methods were investigated for reducing ASE and preventing parasitic lasing, and are described subsequently.

5.4.2.1 Grooving

Grooving or scribing lines, using a very fine diamond-tipped dicing saw, across the waveguide on the side faces was one method employed to destroy the mirror symmetry in the plane. Pitched equivalent to the emitter spacing of the diode bar, the ungrooved regions still allow efficient proximity coupling. Each groove effectively is a diffuse scattering zone no longer allowing specular reflections to build up as a beam passes around an in-plane TIR path. This method was observed to prevent parasitic lasing effects; it is also useful in reducing the ASE, where the grooves also decrease the average path length for beams bouncing off the side faces along the gain region.

5.4.2.2 Thick platelets

Another technique used to frustrate TIR off one side face was to contact a thick (~1mm) piece of YAG to the side face of the waveguide structure, polished at least on the side in contact. In this way the critical angle for TIR is increased to near grazing incidence. Thus light passing into the platelet is only weakly coupled back into the waveguide due to natural divergence after a round trip in the platelet and representing a significant loss for parasitic lasing and reduced solid angle for the ASE. If pumping through both sides, this method requires that the delivery optics are able to accommodate the extra optical distance between the waveguide entrance and face of the platelet.

5.4.2.3 Side-face angle polishing

A third method was to polish the side face at an angle to the normal of the waveguide plane and parallel to the end faces, as described in section 5.3.2. In this fashion, light reflected back into the waveguide from the side face would be forced into higher order modes and eventually into radiation modes after successive reflections, where it is lost completely. If the angle is increased beyond the NA of the waveguide then all modes would be coupled directly into radiation modes, representing the strongest method for reducing undesired feedback into the waveguide. This angle corresponds to ~16º for the YAG/sapphire waveguide composites investigated.

5.4.3 Large mode area planar waveguide laser with monolithic unstable resonator

5.4.3.1 Introduction

Comparisons between resonator configurations show that unstable cavities can produce the largest mode volume for short cavities [21]. To achieve sufficient discrimination between the fundamental and higher-order modes in an unstable resonator, a high output coupling and therefore high gain is required [21], well suited to the waveguide structure. The output power coupling is related to the cavity geometric magnification (M_g), which for a strip unstable resonator[xxviii] is given by:

$$T_l^{oc} = 1 - \frac{1}{M_g} \tag{5.7}$$

[xxviii] Strip unstable resonator refers to the output coupling being extracted in one axis only.

M_g is calculated using the laser cavity ABCD matrix and depends upon the magnifying or de-magnifying power of the resonator [21].

A LMA PW laser monolithic unstable resonator of magnification M_g=1.16 was previously reported by Beach *et al.* [10], demonstrating improved beam quality with respect to the plane-plane resonator. The authors suggest that by increasing the magnification factor a near-diffraction-limited output could be expected. Their cavity consisted of one flat end-face coated with a HR dielectric mirror and the other face was polished with a 20cm concave radius of curvature and coated over the central 64% with a 70%R mirror, the remaining area being anti-reflection coated. The output beam was spatially structured similar to a diffraction pattern for a plane wave passing a rectangular obscuration equivalent in size to the partially reflective coated region width.

The monolithic unstable resonator reported here was designed such that its output would come from only one side of the output coupling mirror, i.e. off axis as illustrated in Figure 5-16 and similar in design to a resonator proposed by Anan'ev *et al.* as reported in [22].

5.4.3.2 Experimental set-up

The confocal positive-branch off-axis unstable resonator with a geometric magnification of $M \sim 5$ was polished onto the end faces of a direct-bonded LMA PW YAG/sapphire composite. The double-clad waveguide design was the same as for the end-pumped Nd^{3+}-doped LMA structure (section 3.3) and previously reported [10, 11]. The design for the unstable resonator consisted of two curved mirrors confocally positioned and forming a Schmidt-Cassegrain style telescope [23], Figure 5-16(a), which has one half with respect to the optic axis deleted Figure 5-16(b).

The important parameters of the unstable resonator design are summarised in Table 5-3. A concave 1mm wide secondary mirror, R_2, was polished onto one end face with its centre of curvature (the optic axis) positioned 0.1mm away from one side face. A larger convex curvature, R_1, was polished across the entire second end face (with the same optic axis and focal point) forms the primary mirror. The two curvatures spaced by 11.1mm form one side of a beam expanding telescope with 5 times magnification. Both of these curved faces were HR coated, with the remaining flat face adjacent to R_2 anti-reflection coated. In this way the collimated output beam passes by the small concave curvature as it exits the cavity, as illustrated in Figure 5-16(b). The side faces were grooved as described in section

5.4.2.1 to accommodate proximity coupling of 20 or 40W CW diode bars from Coherent Inc.

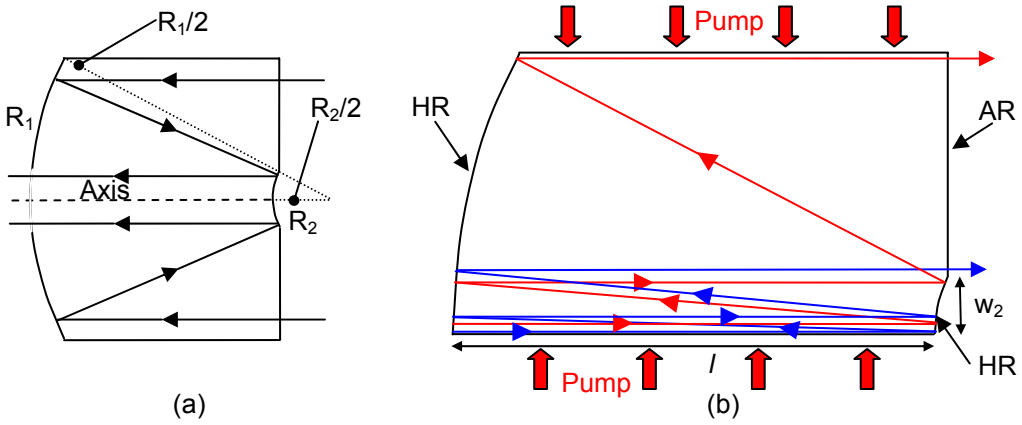

Figure 5-16: (a) Schmidt-Cassegrain telescope and (b) the view of (a) with one side of the axis deleted and forming the basis of the monolithic confocal UR.

Parameter		Value (mm)	Tolerance (mm)
Small radius of curvature	R_2	6.35	±0.1
Width of small mirror	w_2	1	+0, -0.1
Large radius of curvature	R_1	28.58	±0.2
Mirror spacing	l	11.1	+0.1, -0.05

Table 5-3: Monolithic unstable LMA PW laser resonator design parameters.

The waveguide was fabricated by Onyx Optics, who also did the additional polishing of the curved surfaces. To demonstrate the off-axis UR concept it was decided that spherical polishing would suffice for the curvatures, although cylindrical polishing perpendicular to the plane would have been preferred. Due to the complexity of the task and tight manufacturing tolerances the resulting in-plane unstable resonator structure resembled that shown in Figure 5-17. Note that the optic axis, denoted by the blue dashed line was found to lie inside the side face of the composite, whereby two 45° chamfers where required to prevent build up of radiation which would not reach the flat exit face. This meant that the first 0.5mm of pumped active material, closest to the small mirror would not contribute to

the extracted output power. The width of the curvature, R_2, was also reduced to maintain the 1:5 geometric ratio.

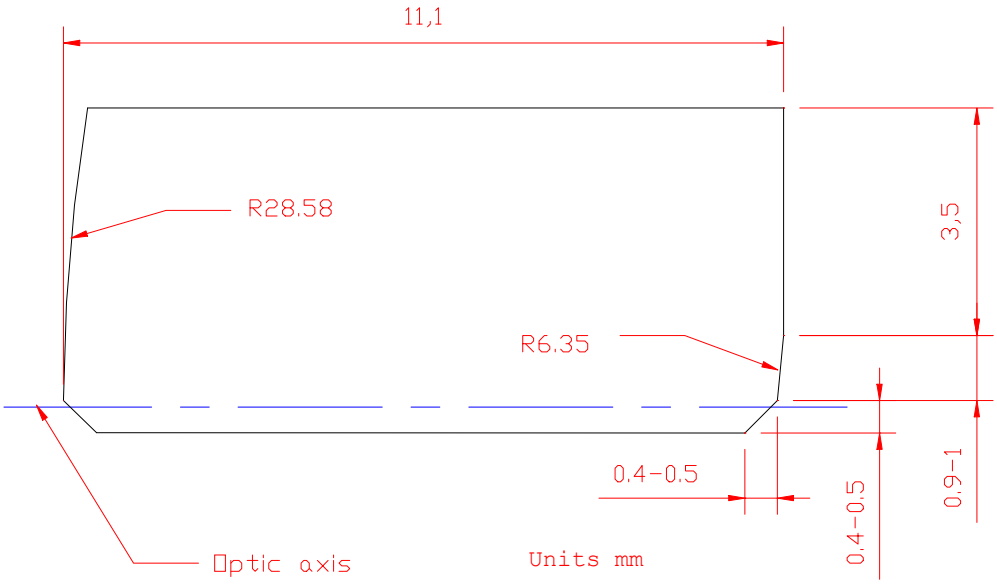

Figure 5-17: Plan view of 5x magnification unstable resonator. Output exits the flat 3.5mm wide surface.

The finished composite structure was then sent to SLS Optics[xxix] for coating of the waveguide faces. Further to the physical differences with respect to the actual design, the coating process required a finite edge width for the HR coating on the curvature R_2. Thus it was discovered that a proportion of the HR mirror carried over onto the flat exit aperture of the cavity, the effects of which will be discussed below.

As with the Tm:YAG LMA PW laser described earlier, two 20W Coherent diodes were proximity coupled to the waveguide using the same setup as pictured in Figure 5-4(b). The diode mounts were water cooled along with the copper pedestal supporting the waveguide, thus the heat sink temperature was optimised for strongest pump absorption. The diodes were brought to within ~30–50µm of the waveguide side face, limited by the copper heat sink overhanging the diode bar clashing with the sapphire outer-cladding. Thus the launch efficiency was estimated to be ~75-85% as illustrated by Figure 5-2.

[xxix] SLS Optics Ltd., Isle of Mann, IM4 4QD, British Isles

5.4.3.3 Laser performance

Firstly, two distinct output beams were found to exit the waveguide, one of which was attributed to the HR coating encroaching onto the cavity output coupling face. The other beam (denoted the main beam) had a broad rectangular profile as was expected from the large output aperture of the cavity. This beam was angled at ~5mrad with respect to the output-face normal indicating that the optic axes of the curved surfaces were misaligned. The additional beam (denoted the secondary beam) was found to exit the waveguide at an angle of ~30mrad with respect to the output-face normal was believed to come from multiple reflections between the HR mirror coatings, particularly the finite width ~150μm, of the HR coating overlaying the flat exit face.

Notwithstanding, the total output power from the LMA PW structure when pumped with two proximity-coupled 20W diode bars, is shown in Figure 5-18. Separately the two distinct beams were observed to have their own threshold and slope efficiencies, with the secondary beam soon extracting more of the available gain than the main beam.

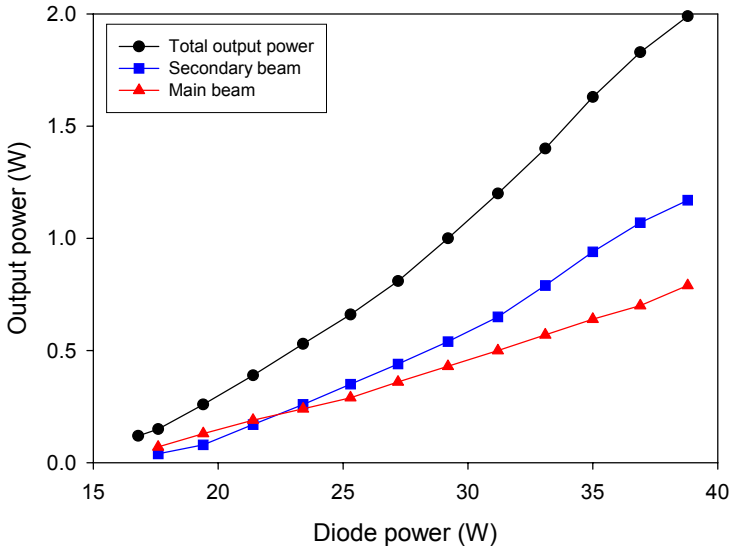

Figure 5-18: Laser output power from Mag. 5 unstable resonator.

Images of the far field intensity pattern from the UR, with the guided axis near-collimated using an f = 22mm cylindrical lens, were captured on a CCD camera at the focal plane of

an f = 40mm Gradium[xxx] lens, positioned ~165mm from the waveguide. The beam was attenuated using a variable-reflectivity wheel, a single reflection from an uncoated wedge, and coloured glass filters. Two far field images, corresponding to the maximum output power of Figure 5-18, of the main UR resonator beam and total laser output are shown in Figure 5-19 (a) and (b) respectively. Evident from these images is that the beam quality does not appear to be diffraction-limited, not even the guided axis (vertical with respect to the page). To verify this, the secondary beam was blocked whilst measuring the beam quality of the main beam. A beam quality of $M^2_x = 60 \pm 2$ in the plane and $M^2_y = 11.8 \pm 0.5$ in the guided axis were obtained. A measure of the total output beam quality was not undertaken due to the large angular separation between the two beams.

(a) (b)

Figure 5-19: Far field intensity patterns captured on a CCD camera, for (a) the main UR output beam and (b) the total laser output. Note guided axis was near collimated to enable viewing on a single CCD. The left-hand-side lobe of (b) is the same as image (a), although the scale is different between the two images.

5.4.3.4 Unstable resonator discussion

Thought to be the first demonstration of a high magnification off-axis monolithic LMA PW laser, this device did not perform as expected. The unguided axis output beam quality, the main parameter of importance in this investigation, improved approximately fivefold with respect to the plane-plane monolithic structure of the same size. However, the guided axis beam quality was degraded, attributed to the spherical mirror curvatures forcing the fundamental-mode into higher-order modes supported by the waveguide.

[xxx] LightPath Technologies, Inc. Walnut, CA 91789

A further investigation of unstable resonators is required to fully appreciate the high gains achievable with the planar waveguide. Extended unstable resonators have already been demonstrated in a thick face-pumped waveguide [24] and pump guided slabs [25], thus representing one method to avoid the fabrication intensive approach described here.

5.4.4 Large mode area planar waveguide laser with extended cavity

5.4.4.1 Introduction

Although not in keeping with the compact monolithic concept, an extended stable cavity was implemented as a means to improve beam quality in the unguided axis of a planar waveguide laser. Stable extended-cavity configurations have previously been demonstrated with direct-bonded multimode waveguides with good success [26-28]. However, these devices were limited to ~1W output powers, due to a combination of thermal issues and short absorption widths. A relatively simple cavity, pictured in Figure 5-20, based on the telescopic resonator concept [29] is reported here and preliminary results discussed.

The cavity investigated capitalises on the fact that the two orthogonal axes of the waveguide may be treated independently. Using ABCD matrices and accounting for the real lenses thickness and curvatures, a ~125mm long cavity was modelled, the schematic of which is illustrated in Figure 5-20(a). An example of the resulting cavity mode is shown in Figure 5-20(b). Due to its small mode size (~10μm), the guided beam upon exiting the waveguide has significant divergence, equivalent to having passed through a negative lens. As such, only a single positive lens is needed to act as a correcting – collimating element. The combination of waveguide and single positive lens imitates a cylindrical beam expanding telescope. The position of the collimating lens is determined by enforcing the relationship that after a round trip through the cavity, from the waveguide output face to the output coupler mirror and back again, the beam radius must match that of the fundamental mode of the waveguide.

In the waveguide the beam radius in the unguided axis is required to be approximately 1-1.5mm, if fundamental mode behaviour is to be approached, relying on increased diffraction losses for the higher order modes caused by the 5mm wide aperture of the waveguide structure [30]. As such the cavity considered for the x-axis is similar to a hemispherical cavity with the curved mirror replaced by a single cylindrical positive lens

with the plane mirror at its focal plane. In this way the beam waists defining the output beam characteristics in both axes, are located at the plane output coupler (OC) mirror with an ellipticity of ~1:10 (x:y), easily circularised using an extra-cavity cylindrical lens.

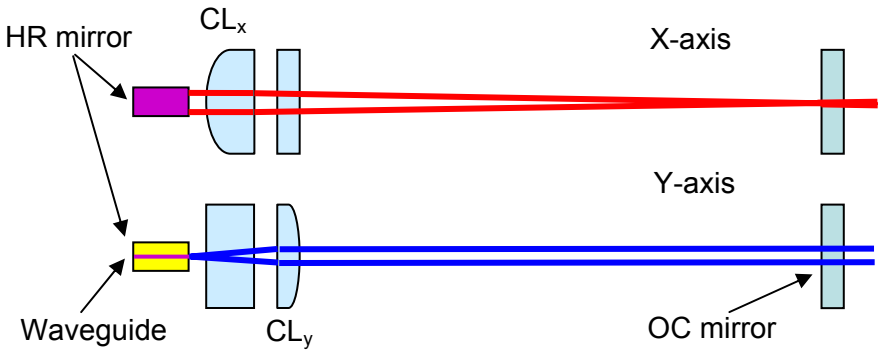

(a)

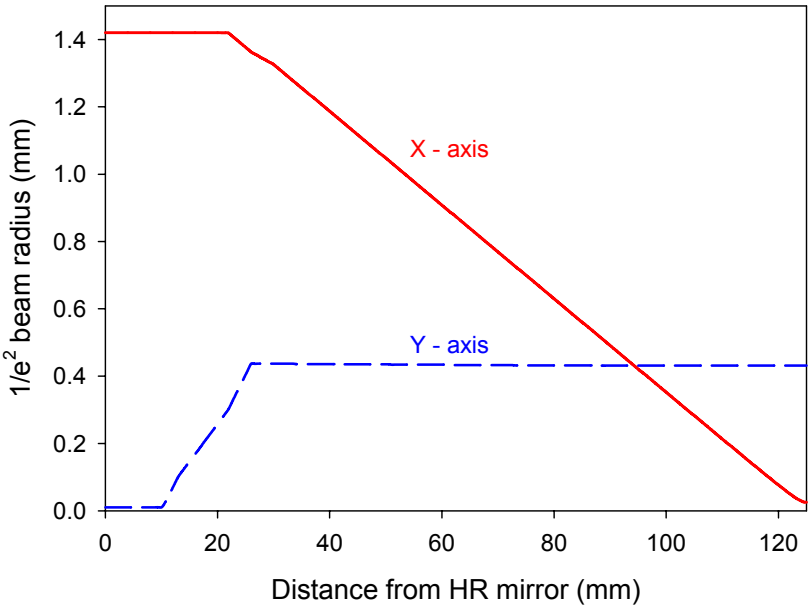

(b)

Figure 5-20: (a) Schematic of extended cavity configuration, CL_x, CL_y are cylindrical lenses operating in the x and y axes respectively. (b) An example of modelled beam radii for the two independent axes of the cavity.

5.4.4.2 Experimental set-up

The pump source was a fast-axis collimated diode bar from IMC[xxxi] producing 29W of output power for 48A of current. Water cooled and with a peak wavelength of 807nm at the maximum current, it was enclosed in a protective housing with an AR coated exit window. With the planar geometry of the diode bar and LMA PW aligned, a cylindrical lens of 19mm focal length focussed the diode slow axis output at ~50mm from the output window of the housing, where a Doric lens of ~1 mm focal length focussed the y-axis collimated beam forming an elliptical spot with second-moments radii of ~ 15μm x 2.5mm.

Mounted on a 6-axis translation stage the waveguide, the same as that detailed in the end-pumped configuration, section 3.3, was aligned to optimise pump coupling. As described in section 5.4.2.2, a thick YAG platelet was affixed to the un-pumped side face to frustrate parasitic lasing paths. A lightweight HR mirror was held to the rear face of the waveguide via the surface tension of a thin layer of fluorinated liquid. No active cooling was used for the waveguide in this experiment. All side and end faces were coated with an anti-reflection quarter-wave thick MgF_2 layer at the wavelengths of interest, i.e. 807nm for the side and 1.064μm for the end faces.

The cavity comprised a HR mirror, coating adjacent to the waveguide, two AR coated cylindrical lenses of focal lengths, f_{CLx} = 100mm and f_{CLy} = 12.7mm, oriented as shown in Figure 5-20(a), and a plane 85% reflective output coupler mirror positioned at the focal plane of lens CL_x. Lens CL_y was positioned such that the mode size from the waveguide would be coupled back into the guide after a round trip to and from the output coupler mirror. This was aligned by shaping another low power diode laser source at a wavelength of 1.06μm such that its beam radii approximated that of the desired cavity mode in the waveguide. Launched into the HR mirror end of the cavity the y-axis of the probe beam was collimated upon exit from lens CL_y giving the required waveguide lens separation.

[xxxi] Cutting Edge Optronics, MO 63301, USA

5.4.4.3 Laser performance

When configured to give reasonable output power performance, as shown in Figure 5-21, the cavity was shorter than predicted for the unguided axis aperture to be filled by the fundamental mode. Consequently although an output power of 6W was obtained, the beam quality as indicated by the inset in Figure 5-21 was not single mode. To obtain the beam profile shown in the inset, the laser output was first collimated in the x-axis with a single f = 100mm cylindrical lens, attenuated using a reflection from an uncoated glass wedge and Schott[xxxii] coloured glass filters, then captured by a CCD camera connected to a computer with digital frame-grabber and Beamview Analyser software by Coherent Inc. A full determination of the laser beam quality was not possible, due to the time required to do so and the temporary nature of the HR mirror contact. However, from the modelled beam width and divergence characteristics, the beam quality was estimated to have an $M^2_x \sim 25$.

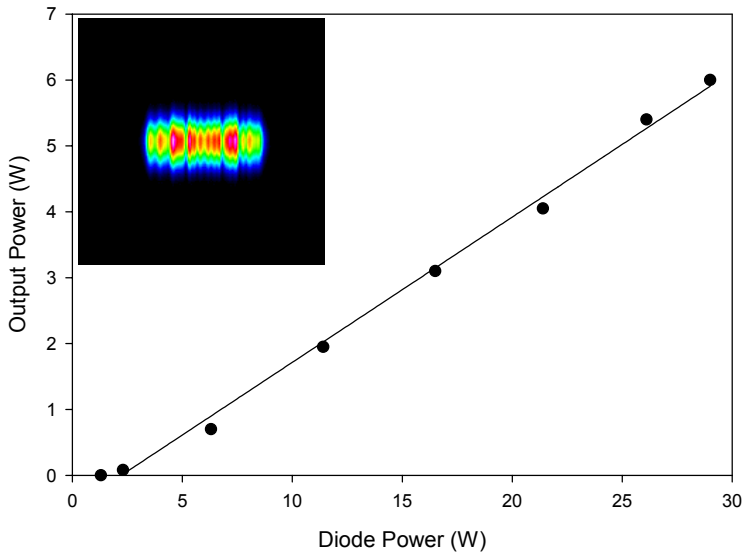

Figure 5-21: Output power performance of extended cavity operating in a multi-mode regime. Inset is a beam profile collected after collimating the in plane axis of the laser output, $M^2_x \sim 25$.

The output profile was improved, approaching the diffraction-limit with the beam profile as shown in Figure 5-22(a), by extending the cavity length to that predicted by the model,

[xxxii] Schott Glass Technologies, 400 York Avenue, Duryea, PA 18642 USA

i.e. ~125mm. However, this was at a cost of ~ 50% in output power, attributed to a reduced overlap between the quasi-uniform gain region and the Gaussian laser photon distribution [31]. Once again due to the temporary nature of the thin HR mirror attachment, exacerbated by the thermal loading of the crystal, the profile changed to that shown in Figure 5-22(b) moments after image Figure 5-22(a) was captured.

It was found near impossible to sustain a good mirror contact using Fluorinert as the fixative; other trialled solutions were even less successful. Therefore output performance as a function of pump power was not characterised with the cavity length optimised for beam quality.

(a) (b)

Figure 5-22: (a) Near diffraction-limited beam profile from an extended cavity, output collimated in the in-plane axis with a cylindrical lens before CCD camera. (b) same profile with thin mirror detaching.

5.4.4.4 Extended cavity discussion

The successful demonstration of an improvement in the unguided axis beam quality using an extended cavity has opened the way for further investigations into such sources. These preliminary results correspond to a significant increase in brightness with respect to that found for the monolithic plane-plane LMA PW laser. Noting the difficulty encountered with the attachment of the HR mirror, this waveguide was subsequently used in an end-pumped configuration detailed in the Chapter 3. Further work has since been carried out with dielectric mirrors coated directly onto the end faces and the side faces angle polished for ASE and parasitic lasing suppression. The details of this experiment have been included in Appendix A; being predominantly undertaken by a colleague, Dr C. Li. Suffice to say that improved performance was obtained with 6W of output power measured with beam quality factors, M_x^2=2.7 (un-guided axis) and M_y^2=1.1 (guided axis).

5.5 Summary

Efficient high-power operation of LMA planar waveguide lasers has been demonstrated at laser wavelengths of 1 and 2μm. The high numerical aperture waveguide structure allowed simple and direct coupling of the diode-bar pump power to the active core. Furthermore, the diode-pumped laser performance of the Tm:YAG LMA PW represents, to my knowledge, the highest reported slope efficiency for this active material, an example of the excellent thermal management and high gains achievable with these structures. A plane-wave model was found to be in excellent agreement with the experimental data and reported values for the variables used. Power scaling to the 100W regime appears possible for simple changes to the described configuration.

Two approaches were employed in an attempt to improve the beam quality in the unguided axis for the side-pumped configuration, the first a monolithic unstable resonator and the second an extended stable resonator. The first showed partial improvement in beam quality, however the actual laser performance did not meet expectations. Being the first iteration of a high-magnification off-axis unstable resonator, performance improvements are expected for future investigations. The second approach investigated was to utilise an extended cavity where the beam quality was found to approach the diffraction-limit. Further work has already demonstrated 6W with good beam quality from a side-pumped configuration.

As mentioned earlier in the chapter, the side-pumped geometry allows efficient and simple coupling of high-power pump sources, for example >100W diode-bar stacks. In addition, by optimising the thermal properties of the planar waveguide, such as the overall structure thickness and the interface with the heat sink, thermal loads of several hundreds of Watts per cm length can be tolerated before crystal fracture is expected to occur. These side-pumped planar waveguide devices could therefore be used to scale the output power into the kW regime.

5.6 References

[1] W. F. Krupke and L. L. Chase, "Ground-State Depleted Solid-State Lasers - Principles, Characteristics and Scaling," *Optical and Quantum Electronics*, vol. 22, pp. S1-S22, 1990.

[2] J. M. Eggleston, T. J. Kane, K. Kuhn, J. Unternahrer, and R. L. Byer, "The Slab Geometry Laser .1. Theory," *IEEE Journal of Quantum Electronics*, vol. 20, pp. 289-301, 1984.

[3] W. A. Clarkson and D. C. Hanna, "Two-mirror beam-shaping technique for high-power diode bars," *Optics Letters*, vol. 21, pp. 375-377, 1996.

[4] J. R. Leger and W. C. Goltsos, "Geometrical Transformation of Linear Diode-Laser Arrays for Longitudinal Pumping of Solid-State Lasers," *IEEE Journal of Quantum Electronics*, vol. 28, pp. 1088-1100, 1992.

[5] B. Ehlers, K. Du, M. Baumann, H.-G. Treusch, P. Loosen, and R. Proprawe, "Beam shaping and fiber coupling of high-power diode laser arrays," *Proceedings of SPIE: Lasers in Material Processing*, vol. 3097, pp. 639-644, 1997.

[6] E. C. Honea, R. J. Beach, S. B. Sutton, J. A. Speth, S. C. Mitchell, J. A. Skidmore, M. A. Emanuel, and S. A. Payne, "115-W Tm:YAG diode-pumped solid-state laser," *IEEE Journal of Quantum Electronics*, vol. 33, pp. 1592-1600, 1997.

[7] K. S. Lai, P. B. Phua, R. F. Wu, Y. L. Lim, E. Lau, S. W. Toh, B. T. Toh, and A. Chng, "120-W continuous-wave diode-pumped Tm : YAG laser," *Optics Letters*, vol. 25, pp. 1591-1593, 2000.

[8] A. Rameix, C. Borel, B. Chambaz, B. Ferrand, D. P. Shepherd, T. J. Warburton, D. C. Hanna, and A. C. Tropper, "An efficient, diode-pumped, 2μm Tm:YAG waveguide laser," *Optics Communications*, vol. 142, pp. 239-243, 1997.

[9] R. A. Hayward, W. A. Clarkson, P. W. Turner, J. Nilsson, A. B. Grudinin, and D. C. Hanna, "Efficient cladding-pumped Tm-doped silica fibre laser with high power singlemode output at 2μm," *Electronics Letters*, vol. 36, pp. 711-712, 2000.

[10] R. J. Beach, S. C. Mitchell, H. E. Meissner, O. R. Meissner, W. F. Krupke, J. M. McMahon, W. J. Bennett, and D. P. Shepherd, "Continuous-wave and passively Q-switched cladding-pumped planar waveguide lasers," *Optics Letters*, vol. 26, pp. 881-883, 2001.

[11] C. L. Bonner, T. Bhutta, D. P. Shepherd, and A. C. Tropper, "Double-clad structures and proximity coupling for diode-bar- pumped planar waveguide lasers," *IEEE Journal of Quantum Electronics*, vol. 36, pp. 236-242, 2000.

[12] W. Koechner, *Solid State Laser Engineering - Chapter 5*, vol. 1, 4th ed. Berlin Heidelberg: Springer Verlag, 1999.

[13] R. J. Beach, "CW theory of quasi-three level end-pumped laser oscillators," *Optics Communications*, vol. 123, pp. 385-393, 1996.

[14] J. B. Gruber, M. E. Hills, R. M. Macfarlane, C. A. Morrison, G. A. Turner, G. J. Quarles, G. J. Kintz, and L. Esterowitz, "Spectra and Energy-Levels of Tm-3+ - $Y_3Al_5O_{12}$," *Physical Review B*, vol. 40, pp. 9464-9478, 1989.

[15] G. Rustad and K. Stenersen, "Modeling of laser-pumped Tm and Ho lasers accounting for upconversion and ground-state depletion," *IEEE Journal of Quantum Electronics*, vol. 32, pp. 1645-1656, 1996.

[16] L. B. Shaw, R. S. F. Chang, and N. Djeu, "Measurement of up-Conversion Energy-Transfer Probabilities in $HoY_3Al_5O_{12}$ and $TmY_3Al_5O_{12}$," *Physical Review B*, vol. 50, pp. 6609-6619, 1994.

[17] T. Nishimura and T. Omi, "Relation between laser characteristics and Nd ion concentration in Nd:YAG," *Japanese Journal of Applied Physics*, vol. 14, pp. 1011-1016, 1975.
[18] Y. F. Chen, Y. P. Lan, and S. C. Wang, "Influence of energy-transfer upconversion on the performance of high-power diode-end-pumped CW lasers," *IEEE Journal of Quantum Electronics*, vol. 36, pp. 615-619, 2000.
[19] W. Koechner, *Solid State Laser Engineering - Chapter 7*, vol. 1, 4th ed. Berlin Heidelberg: Springer Verlag, 1999.
[20] J. Harrison, P. F. Moulton, and G. A. Scott, "13-W, M^2<1.2 Nd:YLF Laser Pumped by a Pair of 20-W Diode-Laser Bars," *CLEO '95, Postdeadline Paper*, 1995.
[21] A. E. Siegmann, *Lasers - Chapter 22*, 1st ed. New York: University Science Books, 1986.
[22] A. E. Siegmann, "Unstable Optical Resonators," *Applied Optics*, vol. 13, pp. 353-367, 1974.
[23] M. Born and E. Wolf, *Principles of Optics - pg 279*, vol. 1, 7th ed. Cambridge: Cambridge University Press, 1999.
[24] J. R. Lee, H. J. Baker, G. J. Friel, G. J. Hilton, and D. R. Hall, "High-average-power Nd : YAG planar waveguide laser that is face pumped by 10 laser diode bars," *Optics Letters*, vol. 27, pp. 524-526, 2002.
[25] N. Hodgson, H. J. Hoffman, V. Ter-Mikirtychev, and W. Jordon, "Diode-pumped, 220W ultra-thin Nd:YAG slab laser with near-diffraction limited beam quality," presented at Technical Digest, Advanced Solid State Lasers, Quebec City, Canada, 2002.
[26] U. Griebner, R. Grunwald, H. Schonnagel, J. Huschke, and G. Erbert, "Laser with guided pump and free-propagating resonator mode using diffusion-bonded rectangular channel waveguides," *Applied Physics Letters*, vol. 77, pp. 3505-3507, 2000.
[27] U. Griebner, R. Grunwald, and H. Schonnagel, "Thermally bonded Yb : YAG planar waveguide laser," *Optics Communications*, vol. 164, pp. 185-190, 1999.
[28] U. Griebner and H. Schonnagel, "Laser operation with nearly diffraction-limited output from a Yb:YAG multimode channel waveguide," *Optics Letters*, vol. 24, pp. 750-752, 1999.
[29] D. C. Hanna, C. G. Sawyers, and M. A. Yuratich, "Telescopic Resonators for Large-Volume TEM_{00}-Mode Operation," *Optical and Quantum Electronics*, vol. 13, pp. 493-507, 1981.
[30] H. Kogelnik and T. Li, "Laser Beams and Resonators," *Applied Optics*, vol. 5, pp. 1550-67, 1966.
[31] D. C. Hanna, A. C. Large, D. P. Shepherd, A. C. Tropper, I. Chartier, B. Ferrand, and D. Pelenc, "A Side-Pumped Nd-YAG Epitaxial Wave-Guide Laser," *Optics Communications*, vol. 91, pp. 229-235, 1992.

Chapter 6

CONCLUSION

6.1 Summary of work presented

Several high-brightness, compact, diode-pumped planar waveguide lasers, with near- and fully-diffraction-limited beam quality, have been demonstrated. Essential to the performance of these lasers has been the direct-bonding technology [1], enabling the fabrication of high-numerical-aperture YAG/sapphire composite structures with excellent thermal and wave-guiding properties. As important has been the development of the double-clad, large-mode-area (LMA) waveguides [2, 3], without which gain mode selection of the fundamental mode could not have been achieved within the fabrication limits of the planar structures.

Furthermore, the high gains possible with these devices allow the operation of weak and quasi-three-level laser transitions that typically require pumping at levels approaching the saturation intensity. Such high gains also make possible highly efficient end-pumped operation, with the observed performance approaching the highest known report of diode-pumped slope and optical-optical efficiency for a Nd:YAG laser [4, 5]. High-powers were also possible due to the slab-like geometry of the planar waveguide, which is well matched to that of the high-power diode laser, allowing simple and efficient coupling schemes to be utilised. Finally, the YAG/sapphire composite structure has additional benefits in terms of efficient management of the waste heat derived from the deficit in pump and lasing photon energy; primarily because the waveguide is an ultra-thin slab with large cooling surfaces with respect to the active volume and the thermal conductivity of sapphire, almost three times that of YAG, dominating the thermal resistance between the heat source and sink.

6.1.1 Modelling

A laser performance model was detailed that accounted for the spatial dependence of the doping, pump and laser photon distributions, and reabsorption at the laser wavelength.

This model was then extended to demonstrate the gain mode selection for the general case of non-uniformly doped active materials. A quasi-three-level laser-energetics model was also introduced, applicable to side-pumped LMA PW lasers where the spatial distribution of either pump or laser fields are unknown. Included in this model were ground-state depletion, gain saturation, cross-relaxation, and upconversion. Both of these models were shown to be in excellent agreement with experimental results.

In addition to the laser performance modelling, it was necessary to understand the thermal characteristics of the investigated devices. Typically going to smaller active devices yet maintaining high-average powers increases the thermal load per unit volume, temperature rise, and thus associated effects, e.g. increased threshold, lensing, and stress fracture to name a few. Two analyses were presented, each applicable to the different in-plane pumping schemes investigated. Both demonstrated that the YAG/sapphire composite structures are well suited to the high thermal loads experienced in high-power lasers, and in fact can have better performance than obtained with bulk crystal structures.

The theoretical description of the propagating modes in a general double-clad planar waveguide was detailed. Including a refractive index rise associated with doping the central YAG layer with rare-earth ions leads to increased confinement of the waveguide modes to the active region. This effect forces the real rare-earth doped double-clad waveguide towards the classical single-mode core design. Therefore achieving fundamental mode operation from a LMA PW laser is proven possible only by careful choice of the doped core thickness with respect to the waveguide aperture, and the index difference between core and inner cladding. Gain selection of the fundamental guided mode has also been shown to be relatively independent of the oscillating wavelength, allowing operation of the same waveguide structure (optimised for the shortest wavelength) at several different laser transitions whilst maintaining good beam quality.

6.1.2 End-pumping

Efficient end-pumped operation of Nd:YAG, and Er:YAG CW LMA-PW lasers were realised. In the Nd:YAG device 4.3W of CW 1.064μm diffraction-limited output was obtained for 7.5W of absorbed pump power. This corresponded to a η_s~58% slope efficiency and ~17% wall-plug efficiency, where further optimisation of the pump-coupling configuration could see this improved to ~20%. Optimising the laser for the quasi-three-level transition at 946nm, an output of 3.5W was measured for 6.5W of

absorbed pump power. Again representing the highest known diode-pumped slope efficiency η_s~57% for this transition, the additional benefits of a monolithic cavity and passive cooling make this a particularly attractive compact high-power laser source. Furthermore, when optimised for 1.33μm the same device generated 2.7W of output power with 7.2W of absorbed pump. Finally, with a non-optimised laser cavity the highest reported output power of 0.4W at 1.8μm from Nd:YAG was observed for 5.5W of absorbed pump. It is expected that output powers at this wavelength could exceed 1W from the same set up as investigated in Chapter 3, by simply optimising the cavity output coupling.

In the first demonstration of a CW pumped Er:YAG LMA PW laser, an output power of 0.45W at a wavelength of 2.7μm was obtained in initial experiments. Further investigations are expected to reveal Watt level outputs around 2.94μm through improved wavelength discrimination in the cavity output coupling and the use of a shorter resonator. Simple high-brightness lasers at this wavelength are highly sort after for their strong absorption by water and the associated medical applications. A similar end-pumped bulk Er:YAG laser, utilising advanced-design high-brightness high-power diodes, generated 1W at 2.94μm [6]. Thus the LMA Er:YAG PW laser further highlights the possibility for obtaining high output powers from weak laser transitions and standard diode pump sources.

Integrating a Cr^{4+} saturable absorber into a Yb:YAG LMA-PW, end-pumped passively Q-switched laser operation with 2.3W average power and ~20kW peak powers was obtained. The laser wavelength at 1.03μm was nearly-diffraction-limited and would make a compact, efficient source for generating Watt level visible outputs through frequency conversion in non-linear crystals. Additionally the peak power of an equivalent Yb:YAG LMA PW laser could be scaled toward the MW regime by simply decreasing the saturable absorber small-signal transmission and shortening the cavity length. Such devices would have several applications in the laser-marking and materials-processing industry. Similar operation of an end-pumped passively Q-switched Nd:YAG LMA PW laser demonstrated inferior performance to that of the Yb^{3+} doped structure due to limitations imposed by the recovery time of the Cr^{4+} saturable absorber.

6.1.3 Side-pumping

Diode side-pumping has been demonstrated as a route to power scaling the output of LMA PW lasers. The high-numerical aperture of the YAG/sapphire composite is shown to efficiently capture the highly divergent output of laser diode bars, by simply positioning them in close proximity to the waveguide. This simple and direct means of pumping an active medium is compatible with producing compact and efficient high-power laser devices.

Applying proximity-coupled side-pumping to a Tm:YAG LMA-PW with a monolithic plane-plane cavity, 15W of 2μm laser output was generated in an asymmetric beam that was diffraction-limited in the guided axis although multimode in the plane. A slope efficiency of η_s~61% was obtained with respect to the absorbed pump power along with a 34% optical to optical conversion. An energetics model of this laser was found to be in excellent agreement with the experimental data and demonstrated that upconversion was the primary limitation to efficient conversion of the pump power. In addition, due to the quasi-three-level nature of the 2μm Tm^{3+} transition, the temperature rise in the waveguide core is shown to also affect the laser performance through an increasing threshold condition. The efficient experimental results are further evidence of the excellent thermal management capabilities of the YAG/sapphire composites.

Despite the efficient performance of the Tm:YAG LMA PW laser, the beam quality and therefore brightness of the output beam was relatively poor. Hence a monolithic off-axis strip unstable resonator was trialled with a Nd:YAG LMA-PW laser, demonstrating an improvement in the in-plane beam quality notwithstanding the fundamental fabrication issues encountered.

A second approach employing an extended stable cavity was investigated as a means to increase the in-plane fundamental mode size and thereby improve beam quality. Using this technique an improvement in the beam profile was observed although at the expense of output power, corresponding to a poorer overlap of the pumping and laser field distributions [7]. Further work using this cavity and with mirrors coated directly onto the end faces of a Nd:YAG LMA waveguide has demonstrated a high-brightness ($M^2_{x,y}$=2.8,1.1) output power of 6W for an absorbed pump power of ~25W. Further improvements in the output power can be expected by using multi-pass cavity designs

which enhance the overlap of the cavity mode and the pumped volume, as will be discussed in the future works section.

6.2 Future Work

6.2.1 Diode-pumped tapered waveguide lasers for integrated optical circuits

Utilising the diode pump sources described in chapter 3 and 4 it is foreseeable that Watt level output powers are possible from tapered waveguides in materials other than YAG. These structures adiabatically expand a single-mode channel up to a broad multimode channel, whereby the fundamental mode of the smaller channel is maintained resulting in diffraction-limited laser output, see Figure 6.1. It may be possible by careful design and fabrication to achieve a reasonable overlap between the fundamental mode of the broad channel at the laser wavelength and the launched multimode pump radiation and therefore efficient laser operation [8-10]. The capability to fabricate these structures on planar chips makes them compatible with integrated optical circuits.

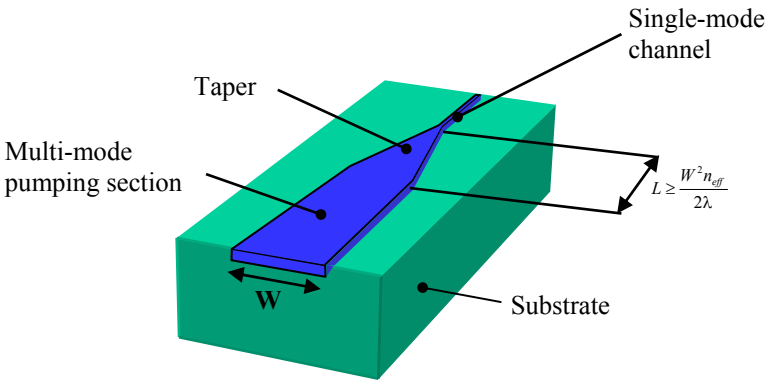

Figure 6.1: Tapered channel waveguide for spatial mode control in the unguided axis.

6.2.2 Stack side-pumping large mode area planar waveguide lasers

Capitalising on the high numerical aperture of YAG/sapphire LMA PW's, the possibility to scale the output powers by in-plane pumping with stacked diode-bar arrays is quite plausible. With commercially available CW collimated diode stacks, noting that a 180W 3-bar stack operating at 808nm has an M^2 parameter (in the fast axis of the diode) of <20[xxxiii], it should be possible to launch ~300W/cm into the waveguide structures

[xxxiii] Beam quality measured from a diode array made by Nuvonyx Inc., Plymouth, MI 48170 USA

described in this thesis. Furthermore by increasing the thickness of the waveguide aperture, whilst tailoring the refractive index profile such that the core-inner cladding index step is $<10^{-4}$, launching even greater pump powers is viable.

6.2.3 Extended cavities

As demonstrated using a stable extended cavity configuration, the beam quality in the unguided axes can be improved, however, to also increase the conversion efficiency of the laser, techniques are required that enhance the overlap of the cavity mode and excited region. Possible methods include the use of an extended unstable resonator as demonstrated in face-pumped thick-waveguides by researchers at Herriott Watt University [11] and side-pumped thin slabs by workers at Spectra Physics Inc. [12], or to pass the laser field several times through the gain region as demonstrated with other side-pumped slab lasers [13]. Gain limiting effects such as ASE, parasitic lasing, and upconversion will most probably define the final configurations investigated.

6.2.4 Quasi-monolithic planar waveguide laser using platelet waveguide mirrors

To maintain the concept of compact planar waveguide lasers, one way to avoid the tight fabrication tolerances for polishing mirror curvatures onto the waveguide structure itself, is through the use of platelet waveguide mirrors. An example of a platelet waveguide is illustrated in Figure 6.2, simply a thin waveguide structure with the same properties and dimensions as an active waveguide, to which it can be proximity coupled in a way similar to butt-coupling optical fibres. Thus the platelet waveguide could be polished and coated just like any other cylindrical optic; the final result being a mirror that only acts in the plane whilst maintaining the fundamental mode in the guided axis.

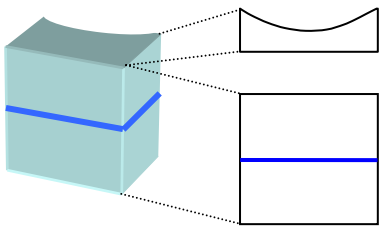

Figure 6.2: Platelet waveguide mirror with front and top views.

As such, it could be possible to arrange quasi-monolithic laser cavities acting in the plane where the platelet mirror could be aligned separately to optimise performance. Mentioned above, an argument exists for using multiple passes through the gain medium to enhance the laser and pump fields overlap condition. In this way a stable cavity can be conceived using two flat end faces and two butt-coupled curved platelet mirrors to form a z-cavity, whilst at the same time increasing the in-plane mode size, see Figure 6.3. Thus although there are a multitude of possibilities to be considered, the LMA PW is an excellent basis from which to start.

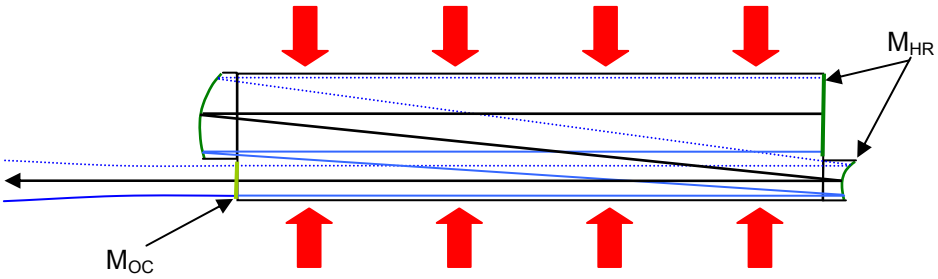

Figure 6.3: Top view of a Z-cavity with platelet waveguide mirrors forming an intra-cavity beam expander.

In conclusion the work presented in this thesis has confirmed that the high numerical aperture, large-mode-area planar waveguide is well suited to high-power diode-pumping and from which efficient laser output can be obtained. Methods to enhance the brightness of these devices have been demonstrated and discussed and while power scaling these devices toward the kilo-Watt regime appears quite feasible, they can also be utilised to enhance the performance of weak and/or quasi-three-level laser transitions. A vast variety of applications await the future development of this class of laser.

6.3 References

[1] C. T. A. Brown, C. L. Bonner, T. J. Warburton, D. P. Shepherd, A. C. Tropper, D. C. Hanna, and H. E. Meissner, "Thermally bonded planar waveguide lasers," *Applied Physics Letters*, vol. 71, pp. 1139-1141, 1997.

[2] N. G. R. Broderick, H. L. Offerhaus, D. J. Richardson, R. A. Sammut, J. Caplen, and L. Dong, "Large mode area fibers for high power applications," *Optical Fiber Technology*, vol. 5, pp. 185-196, 1999.

[3] C. L. Bonner, T. Bhutta, D. P. Shepherd, and A. C. Tropper, "Double-clad structures and proximity coupling for diode-bar- pumped planar waveguide lasers," *IEEE Journal of Quantum Electronics*, vol. 36, pp. 236-242, 2000.

[4] I. T. McKinnie, J. E. Koroshetz, W. S. Pelouch, D. D. Smith, J. R. Unternahrer, and S. W. Henderson, "Self-imaging Nd:YAG laser with 58% slope efficiency," presented at Conference on Lasers and Electro Optics, 2002.

[5] W. Koechner, *Solid State Laser Engineering - Chapter 3*, vol. 1, 4th ed. Berlin Heidelberg: Springer Verlag, 1999.

[6] D. W. Chen, C. L. Fincher, T. S. Rose, F. L. Vernon, and R. A. Fields, "Diode-pumped 1-W continuous-wave Er:YAG 3μm laser," *Optics Letters*, vol. 24, pp. 385-387, 1999.

[7] W. A. Clarkson and D. C. Hanna, "Effects of Transverse-Mode Profile on Slope Efficiency and Relaxation Oscillations in a Longitudinally-Pumped Laser," *Journal of Modern Optics*, vol. 36, pp. 483-498, 1989.

[8] S. J. Hettrick, J. I. Mackenzie, R. D. Harris, J. S. Wilkinson, D. P. Shepherd, and A. C. Tropper, "Ion-exchanged tapered-waveguide laser in neodymium-doped BK7 glass," *Optics Letters*, vol. 25, pp. 1433-1435, 2000.

[9] D. P. Shepherd, S. J. Hettrick, C. Li, J. I. Mackenzie, R. J. Beach, S. C. Mitchell, and H. E. Meissner, "High-power planar dielectric waveguide lasers," *Journal of Physics D-Applied Physics*, vol. 34, pp. 2420-2432, 2001.

[10] P. Madasamy, S. Honkanen, D. F. Geraghty, and N. Peyghambarian, "Single-mode tapered waveguide laser in Er-doped glass with multimode-diode pumping," *Applied Physics Letters*, vol. 82, pp. 1332-1334, 2003.

[11] J. R. Lee, H. J. Baker, G. J. Friel, G. J. Hilton, and D. R. Hall, "High-average-power Nd : YAG planar waveguide laser that is face pumped by 10 laser diode bars," *Optics Letters*, vol. 27, pp. 524-526, 2002.

[12] N. Hodgson, H. J. Hoffman, V. Ter-Mikirtychev, and W. Jordon, "Diode-pumped, 220W ultra-thin Nd:YAG slab laser with near-diffraction limited beam quality," presented at Technical Digest, Advanced Solid State Lasers, Quebec City, Canada, 2002.

[13] J. Harrison, P. F. Moulton, and G. A. Scott, "13-W, M^2<1.2 Nd:YLF Laser Pumped by a Pair of 20-W Diode-Laser Bars," *CLEO '95, Postdeadline Paper*, 1995.

APPENDIX A: EXTENDED CAVITY PAPER

Following is a paper submitted to Optics Communications (April 2003) on an extended cavity diode-pumped waveguide laser. The bulk of the experimental work was carried out during the period of writing this thesis by a colleague, Dr C. Li.

A Diode-Bar Side-Pumped Waveguide Laser with an Extended Stable Cavity for Spatial Mode Control

C.Li, J.I.Mackenzie, J.Wang, and D.P.Shepherd

Optoelectronics Research Centre
University of Southampton
Highfield
Southampton SO17 1BJ, UK

Email dps@orc.soton.ac.uk

Abstract

We describe the use of an extended stable cavity to control the output spatial mode of a diode-bar side-pumped slab waveguide laser. The active medium consists of a Nd:YAG core with a one-dimensional double-clad guiding structure. The device gives >10W output power with a 56% slope efficiency for multi-mode operation, which is reduced to 33% for the best output beam quality parameters (M^2 values) of 2.8 by 1.1. The prospects for obtaining higher efficiencies and scaling to larger average powers are discussed.

Rare-earth-doped slab waveguides offer a combination of features that make them attractive for use as the active medium in high-average-power diode-pumped lasers. These include excellent thermal management and a geometric compatibility with the asymmetric output of high-power diode pump lasers [1], as well as the normal waveguide advantages of high gain and hence low threshold. In the guided axis, although multi-mode waveguides are generally required to confine the non-diffraction-limited output of high-power diode pump sources, it is relatively easy to enforce single-mode operation, for instance through the use of double-clad structures [2,3] or multi-mode interference [4,5]. However, for power-scalable side-pumping arrangements, the pumped mode size in the non-guided axis tends to be ≥0.5cm and so a short (~1cm) monolithic plane/plane cavity leads to highly non-diffraction-limited output. Extended unstable cavity designs have been demonstrated to overcome this problem and output powers of over 100W have been obtained with M^2 values as low as 1.8 by 1.1 [6]. Here we report the use of an extended stable cavity in combination with a double-clad waveguide to achieve the same goal, comparing its performance to the multi-mode case, and finding the limits to the achievable beam quality. We also discuss the prospects for improving the efficiency of the high brightness output and for power scaling.

The waveguide used in these experiments was fabricated by Onyx Optics Inc. and consisted of a 30μm-deep YAG core, of which only the central 20μm is doped with Nd (1at.%), capped by sapphire substrate and cladding layers. The waveguide was 1cm-long in the lasing axis by 5mm-wide in the pumping axis. Fig. 1 shows the experimental arrangement for side-pumping the double-clad

Nd:YAG waveguide. In the guided axis, focussing of the collimated output of the fibre-lensed diode bar is achieved using a 1mm focal length, graded index lens from Doric Lenses Inc.. In the non-guided axis a 19mm focal length cylindrical lens focuses the beam through a 5mm-wide aperture, such that it is less than 1cm wide at the input side-face of the guide. Focussing through the aperture helps to break the symmetry of the pumping scheme and thus minimises the coupling of unabsorbed pump light from one diode into the other. It should be noted that it is also possible to simply proximity-couple diode bars to this type of high numerical aperture (NA) waveguide [1, 2]. The pump-coupling optics used in this case led to approximately 50% of the light being absorbed, which we attribute to the waveguide being approximately one absorption length wide for the diode bar (accounting for the double-clad structure) and a launch efficiency into the guide of nearly 80%. Consequently we were able to operate at up to 25W of absorbed pump power.

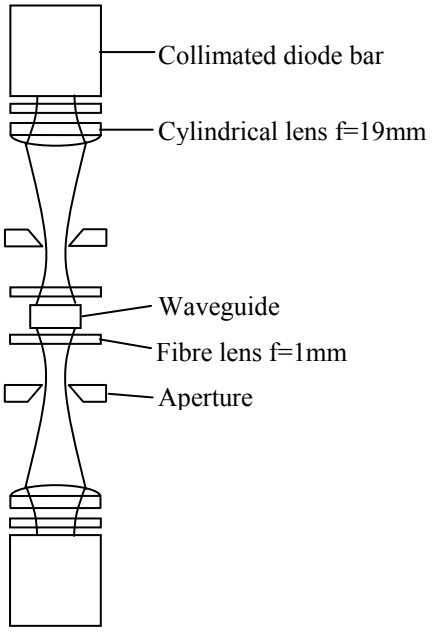

Fig. 1 Coupling optics for side-pumping.

The laser cavity, shown in Fig. 2, was designed using an ABCD matrix model. In the guided axis, fundamental-mode operation is assured by the double-clad structure and re-imaging about a plane mirror at the AR-coated waveguide intra-cavity face. This is achieved by collimating the waveguide output with a 12.7mm focal length cylindrical lens. Conversely, for the non-guided axis, a 100mm focal length cylindrical lens forms a tightly focussed beam-waist at the external plane mirror and can be tailored such that a large cavity mode fills the 5mm-wide gain region by extending the cavity length (~12cm) near to the stability limit at. The outside end-face of the waveguide was directly coated to complete the laser resonator.

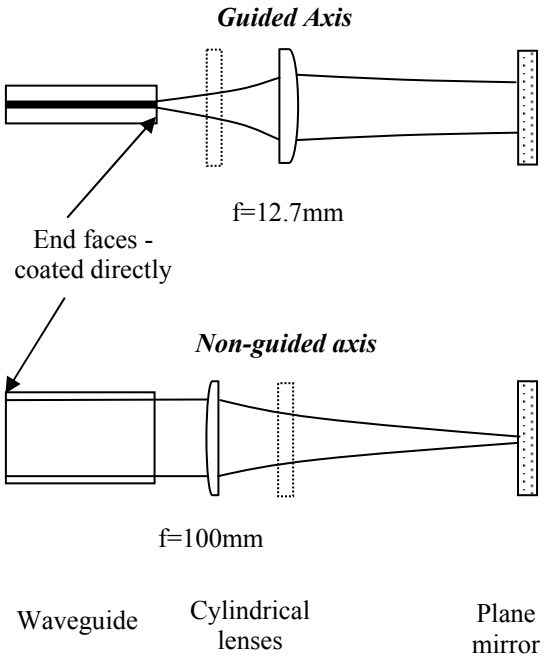

Fig. 2 Extended cavity resonator design.

Fig. 3 shows how the resulting waveguide laser output M^2 values, measured using a Coherent

Modemaster M^2 meter, change with cavity length for a cavity output coupling of 19%. It can be seen that the guided axis remains diffraction-limited in all cases (M^2<1.2), while the beam quality in the non-guided axis reaches M^2=2.8 at its optimum. At this point the output beam profile appears approximately Gaussian in both axes. The use of a plane external mirror means that waists are formed in both axes at this mirror and a single cylindrical collimating lens can be used after the waveguide laser to circularise output as shown in the inset to Fig. 3.

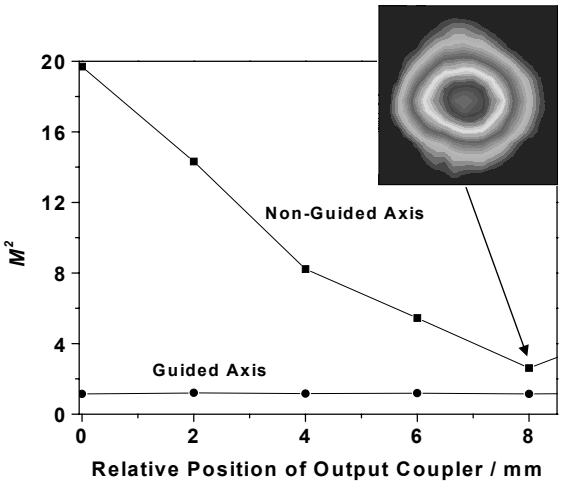

Fig. 3 Output beam quality factor against relative position of the output coupler, with T=19% and an optimum cavity length of ~12cm. The inset shows the optimised collimated output captured on a CCD camera.

Using the optimum output coupling, T=30%, for the high brightness configuration, but optimising the cavity length for power rather than beam quality, gave M^2 values as high as ~60 in the non-guided axis. Fig. 4 compares the output power performance of this highly multi-mode cavity with that of the high-brightness cavity. It can be seen that the slope efficiency is reduced from around 56% to 33% in order to achieve high-brightness output. This is due to the fact that the mode becomes near-Gaussian in the non-guided axis, giving a worse spatial overlap with the step-like gain profile. Thus the gain at the edges of the waveguide cannot be effectively used by the fundamental mode, which reduces the output efficiency and allows gain for higher-order modes such that the measured M^2 is higher than 1 in this axis.

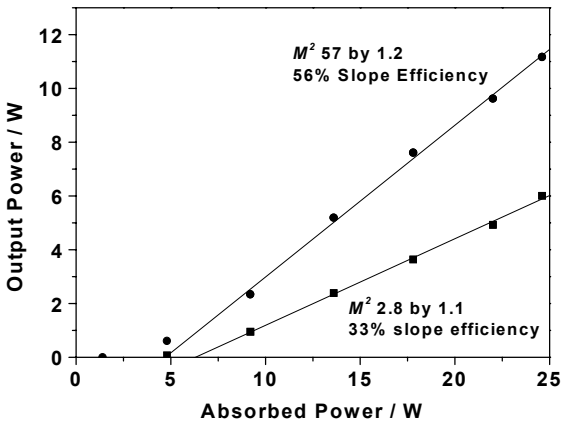

Fig. 4 Output power against absorbed pump power for the high-brightness and multi-mode cavities and an output coupling of T=30%.

The slope efficiency with respect to absorbed pump power for a 4-level laser with a unity pumping quantum efficiency is given by [7]

$$\eta = \frac{T}{(T+L)} \frac{\lambda_p}{\lambda_l} \eta_{pl} \quad ,$$

where T is the output coupler transmission, L represents the other round-trip losses, λ_p and λ_l are the pump and laser frequencies, and η_{pl} is a measure

of the overlap of the normalised pump, $r_0(x,y,z)$, and laser, $s_0(x,y,z)$, spatial distributions given by [7]

$$\eta_{pl} = \frac{\left[\int_{cavity} r_0(x,y,z)s_0(x,y,z)dV\right]^2}{\int_{cavity} r_o(x,y,z)s_0^2(x,y,z)dV} \quad .$$

It is assumed that the normalised functions which represent the experimental set-up are a uniformly pumped doped core, given by

$$r_0(x,y,z) = \frac{1}{dwl}, \; for \; |x| \le \frac{w}{2}, |y| \le \frac{d}{2}, 0 \le z \le l \quad ,$$

and a laser mode with an elliptical Gaussian distribution with beam waists, ω_x and ω_y, averaged over the waveguide length, l, in the non-guided and guided axes respectively; that is

$$s_0(x,y,z) = \frac{2}{\pi\omega_x\omega_y l}\exp\left(-2\left(\frac{x^2}{\omega_x^2}+\frac{y^2}{\omega_y^2}\right)\right) \quad .$$

Therefore, in the guided axis, lasing on the fundamental mode is expected with the beam waist equal to half the active core depth, i.e. $\omega_x=d/2$. This assumes that the mode is well confined within the full 30µm-depth of the YAG layers. If we also assume that the full width of the fundamental cavity mode in the non-guided axis is matched to the width, w, of the waveguide, i.e. $\omega_y \approx w/3$, then we find that η_{pl}=0.48. Hence the maximum possible slope efficiency for Nd:YAG operating at 1.064µm with a 807nm pump, corresponding to negligible round trip losses, is 36%, in good agreement with our experimental value of 33%. In order to improve the output efficiency of the high-brightness side-pumped waveguide laser, a zigzag lasing path could be used in the non-guided axis [8], perhaps involving a bounce off the side-walls [9], to further optimise the overlap of the lasing mode and the pumped volume.

Optimising the output coupling and cavity length for output power, a maximum of 12.2W was observed with T=42%. However, it was also noted that with this output coupling and with the cavity length set to obtain high-brightness operation, the beam quality in the non-guided axis became significantly degraded at higher pump powers with M^2 values of >6. It thus appears that the lower reflectivity cavity has a weaker control of the resonating spatial mode of the cavity and a tendency to go towards the multi-mode output of the monolithic waveguide.

The prospects for power scaling of the high-brightness, side-pumped waveguide laser appear to be good. Firstly, a similar pumping arrangement and waveguide structure would also be compatible with the use of diode-stack pumping. The 30µm-deep, 0.46-NA guides used here are compatible with the use of 3-bar stacks (available with M^2 values in the fast axis of <20) delivering up to 180W of pump power from each side. Even greater pump powers could then be achieved by scaling the depth and/or the length of the guide. The ultra-thin slab geometry of the waveguide is also excellent for handling the thermal loading associated with such high power pumping, giving high stress-fracture limits and low depolarisation loss, while the guide dominates the main thermal-lensing effect. No degradation in beam quality is expected in the guided axis at higher pump powers due to the careful design of the double-clad geometry [3]. In the non-guided axis the M^2 value remained stable over the power regime

investigated here for output coupling <30%, but may degrade at higher powers if gain at the edges of the slab is not efficiently extracted. The use of zigzag lasing paths may help to overcome this problem, as well as improving the overall efficiency of the device. Unstable resonators are also a potential solution for high-efficiency extraction with good beam quality [6]. Efficient extraction of all the available gain is also important in minimising the potential effects of amplified spontaneous emission and parasitic lasing in these high-gain slab waveguides. These latter effects suggest that the planar waveguides will be best suited to continuous-wave or high-repetition-rate pulsed operation.

In summary, we have demonstrated the use of a stable extended cavity consisting of two cylindrical lenses and a plane mirror that can deliver high-brightness, multi-Watt output from a diode-bar side-pumped waveguide laser. Multi-mode output powers of >10W are obtained from the waveguide, at a 56% slope efficiency with respect to absorbed power. When the external cavity is optimised for beam quality, M^2 values of 1.1 (guided) by 2.8 (non-guided) are obtained and the slope efficiency is reduced to 33%, in line with theoretical expectation considering the spatial overlap of the uniformly pumped slab waveguide and the near-Gaussian lasing mode. The prospects for power scaling of this compact and high-brightness source appear to be good, due to the compatibility of the waveguide with diode-stack pumping and its thermal power handling capabilities. The use of zigzag lasing paths to fully extract the available gain and improve the spatial overlap, should lead to higher extraction efficiencies and offer further improvement in non-guided beam quality.

Acknowledgements

This work was supported in part by the award of an EPSRC grant GR/M98449. The authors wish to acknowledge O. Meissner and H. Meissner of Onyx Optics for fabrication of the waveguides used in these experiments.

References

[1] D.P.Shepherd, S.J.Hettrick, C.Li, J.I.Mackenzie, R.J.Beach, S.C.Mitchell, H.E.Meissner, J. Phys. D: Appl. Phys. 34 (2001) 2420.

[2] J.I.Mackenzie, D.P.Shepherd, S.C.Mitchell, R.J.Beach, H.E.Meissner, Electr. Lett. 37 (2001) 898.

[3] T.Bhutta, J.I.Mackenzie, D.P.Shepherd, R.J.Beach, J. Opt. Soc. Am. B 19 (2002) 1539.

[4] W.S.Pelouch, D.D.Smith, J.E.Koroshetz, I.T.McKinnie, J.R.Unternährer, S.W.Henderson, OSA TOPS Vol.68, Advanced Solid-State Lasers (2002) 6.

[5] H.J.Baker, J.R.Lee, D.Hall, Opt. Express 10 (2002) 297.

[6] J.R.Lee, H.J.Baker, D.Hall, OSA TOPS Vol.68 Advanced Solid-State Lasers (2002) 529.

[7] K.Kubodera, K.Otsuka, J. Appl. Phys. 50 (1979) 653.

[8] J.Harrison, P.F.Moulton, G.A.Scott, CLEO'95 Post Deadline Papers, paper CPD20, Optical Society of America, Washington D.C. (1995).

[9] J.E.Bernard, A.J.Alcock, Opt. Lett. 18 (1993) 968.

APPENDIX B: PUBLICATIONS LIST

Journal Publications

[1] S. J. Hettrick, J. I. Mackenzie, R. D. Harris, J. S. Wilkinson, D. P. Shepherd, and A. C. Tropper, "Ion-exchanged tapered-waveguide laser in neodymium-doped BK7 glass," *Optics Letters*, vol. 25, pp. 1433-1435, 2000.

[2] J. I. Mackenzie, S. C. Mitchell, R. J. Beach, H. E. Meissner, and D. P. Shepherd, "15W diode-side-pumped Tm:YAG waveguide laser at 2μm," *Electronics Letters*, vol. 37, pp. 898-899, 2001.

[3] J. I. Mackenzie, C. Li, D. P. Shepherd, H. E. Meissner, and S. C. Mitchell, "Longitudinally diode-pumped Nd:YAG double-clad planar waveguide laser," *Optics Letters*, vol. 26, pp. 698-700, 2001.

[4] D. P. Shepherd, S. J. Hettrick, C. Li, J. I. Mackenzie, R. J. Beach, S. C. Mitchell, and H. E. Meissner, "High-power planar dielectric waveguide lasers," *Journal of Physics D-Applied Physics*, vol. 34, pp. 2420-2432, 2001.

[5] T. Bhutta, J. I. Mackenzie, D. P. Shepherd, and R. J. Beach, "Spatial dopant profiles for transverse-mode selection in multimode waveguides," *Journal of the Optical Society of America B-Optical Physics*, vol. 19, pp. 1539 - 1543, 2002.

[6] J. I. Mackenzie, C. Li, D. P. Shepherd, R. J. Beach, and S. C. Mitchell, "Modeling of high-power continuous-wave Tm:YAG side-pumped double-clad waveguide lasers," *IEEE Journal of Quantum Electronics*, vol. 38, pp. 222-230, 2002.

[7] J. I. Mackenzie and D. P. Shepherd, "End-pumped, passively Q-switched Yb:YAG double-clad waveguide laser," *Optics Letters*, vol. 27, pp. 2161-2163, 2002.

[8] J. I. Mackenzie, C. Li, and D. P. Shepherd, "Multi-watt, high efficiency, diffraction-limited Nd:YAG planar waveguide laser," *IEEE Journal of Quantum Electronics*, vol. 39, pp. 493-500, 2003.

Conference Publications

S.J.Hettrick, J.I.Mackenzie, J.S.Wilkinson, A.C.Tropper, D.Shepherd**,** **"**Ion-exchanged Nd:glass tapered waveguide laser", *CLEO/Europe* Nice 10-15 Sep 2000 CTuM6

C.Li, S.J.Hettrick, J.I.Mackenzie, J.S.Wilkinson, D.P.Shepherd, **"**Longitudinally-diode-pumped high-power waveguide lasers", *ECIO* Paderborn Germany 4-6 Apr 2001 WeB2.4

J.I.Mackenzie, C.Li, D.P.Shepherd, H.E.Meissner, **"**End-pumped double-clad waveguide laser", *CLEO 2001* Baltimore 6-11 May 2001 CFH6

J.I.Mackenzie, S.C.Mitchell, R.J.Beach, H.E.Meissner, D.P.Shepherd, **"**15W diode-pumped Tm:YAG double-clad waveguide laser", *Quantum Electronics & Photonics (QEP 15)* Glasgow 3-6 Sep 2001 P1-7

R.J.Beach, S.C.Mitchell, H.E.Meissner, W.F.Krupke, J.M.McMahon, W.J.Benett, J.I.,Mackenzie, D.P.Shepherd, **"**CW and passively Q-switched cladding pumped planar waveguide lasers", *OSA Annual Meeting 2001/ILS XVII* Long Beach, California 14-18 Oct 2001 (Invited) Paper MD5.

J.I.Mackenzie, S.C.Mitchell, R.J.Beach, H.E.Meissner, D.P.Shepherd, **"**15W diode-pumped Tm:YAG double-clad waveguide laser", *14th Annual Meeting of the IEEE Lasers and Electro-Optics Society (LEOS)* San Diego 2001 MH3

S.J.Hettrick, C.Li, J.I.Mackenzie, J.S.Wilkinson, D.P.Shepherd, **"**Nd:Glass tapered planar waveguide laser", *14th Annual Meeting of the IEEE Lasers and Electro-Optics Society (LEOS)* San Diego 2001 MP3

J.I.Mackenzie, C.Li, J.Wang, D.P.Shepherd, "Multi-watt diffraction-limited CW and Q-switched diode-end-pumped double-clad waveguide lasers", *CLEO/Europe EQEC 2003* Munich 22-27 Jun 2003 CL1-1 THU (accepted)

Invited Seminars

J.I. Mackenzie, T. Bhutta, D.P. Shepherd, R.J. Beach, S.C. Mitchell, H.E. Meissner, O.R. Meissner, W.F. Krupke, J.M. McMahon, W. J. Benett, "CW and Passively Q-switched Double-Clad Planar Waveguide Lasers", *Macquarie University, Sydney, Australia. Nov 2001*

J.I.Mackenzie, S.J.Hettrick, C.Li, and D.P.Shepherd, **"**Planar waveguides for high-power laser devices", SFIT Lausanne, France. March 2002